AIT *informa*

Rivista italiana di
TELERILEVAMENTO

n. 38 - 2007

**Numero speciale
"Telerilevamento urbano"**
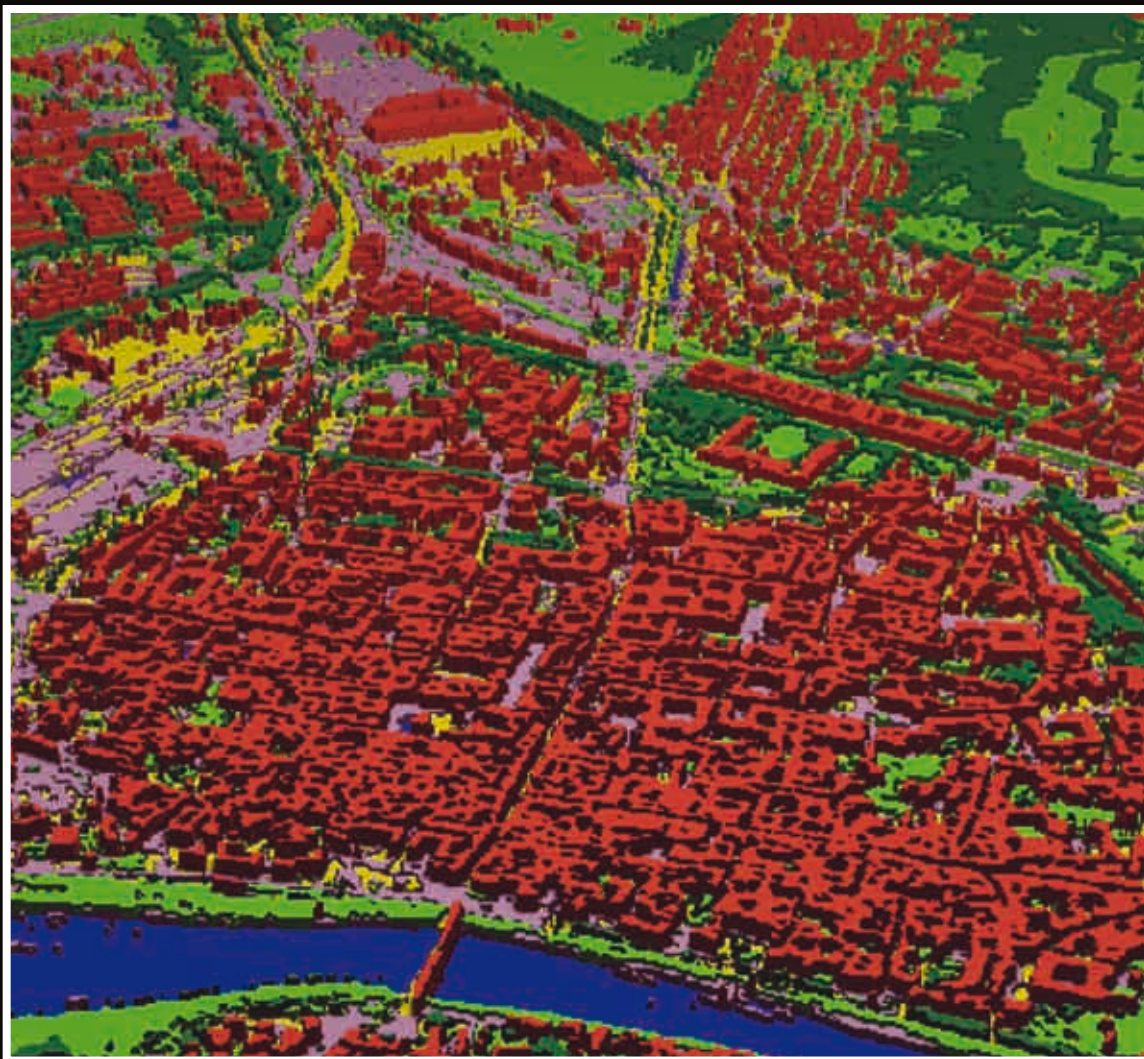
ASSOCIAZIONE ITALIANA DI TELERILEVAMENTO

Rivista italiana di TELERILEVAMENTO

A.I.T. informa

n° 38 - 2007

In copertina: Visualizzazione tridimensionale di una mappa tematica della città di Pavia ottenuta per classificazione di immagini satellitari ad alta risoluzione. © Univ. di Pavia

Cari Lettori … e cari Scrittori,

la Rivista Italiana di Telerilevamento è cresciuta molto negli ultimi anni, sia come qualità dei lavori presentati, sia come veste editoriale e regolarità nelle uscite.

Un'ulteriore crescita richiede forze nuove e idee nuove ed è evidente che un "vecchio" del Telerilevamento non può darle.

E' quindi giunto il momento di lasciare, anche per non correre il rischio di arrivare a sentire "mia" una cosa che è di "tutti". E per tutti intendo quella comunità italiana di telerilevatori che nella Rivista ha trovato un'occasione di scambio scientifico e di crescita culturale, e non solo lo strumento per acquisire punteggi per la propria carriera.

La tentazione di crescere in una direzione internazionale è emersa più volte e certamente si ripresenterà in un prossimo futuro. Anche per questo è il momento di lasciare: le mie idee, che esporrò per l'ultima volta in queste righe, non devono avere un peso diverso da quelle di ogni altro socio di AIT; da Direttore non ne sarei capace.

Quando assunsi la Direzione scientifica della Rivista lo feci perché credevo che la comunità nazionale avesse bisogno di una sede nella quale, non solo presentare i risultati delle proprie ricerche, ma anche fare crescere chi è all'inizio o chi al Telerilevamento chiede servizi e prodotti e vuole saperne di più. I giovani ricercatori, gli studenti, i professionisti e i tecnici degli enti territoriali rientrano in questa categoria e per rivolgersi a loro è preferibile usare la lingua italiana ed abbandonare lo snobbismo del "tutti ormai leggono l'inglese": perché impegnare una parte del cervello a tradurre quando serve tutto per capire?

Certo che sarebbe stato assai più gratificante essere il Direttore di una rivista internazionale, ma se questo era il mio obiettivo mi sarei lanciato in una ben più ardua competizione per "vincere" una di quelle già esistenti ed in grado di ospitare quanto di meglio viene prodotto in tutto il mondo.

In quest'ultimo saluto (cosa che spero non porti male!) non posso non guardare indietro alla vita della nostra associazione: un tempo unione di amici ansiosi di parlare (e di bere) insieme ed oggi fredda appendice di una cosa voluta da pochi e non capita da molti. La diluizione di AIT in ASITA ha portato indubbi vantaggi, ed io so bene quanto ciò abbia giovato alla gestione economica della Rivista, ma ci ha fatto perdere quello "spirito di corpo" che ci caratterizzava negli anni '80 e '90. L'impegno a mantenere convegni AIT, seppure biennali, non è stato mantenuto, l'aspetto didattico è stato quasi completamente abbandonato e i soci, in cambio della loro adesione, hanno ricevuto ben poco oltre la Rivista, come se l'iscrizione non fosse altro che l'abbonamento ad un qualsiasi periodico.

Anche in queste idee dimostro di essere un "vecchio" telerilevatore, ed è proprio bene che mi ritiri!

E' doveroso, a questo punto, fare i migliori auguri al nuovo Direttore scientifico Marco Marchetti, ben conoscendo l'impegno che richiede questo lavoro e quanto ne richiederà per progredire, indipendentemente dalla direzione in cui si vorrà andare.

Potrebbe sembrare un augurio formale, considerato quanto ho scritto sopra, ma non lo è. Credo che Marco abbia dato la propria disponibilità con lo spirito con cui tredici anni fa la detti anch'io: mettere il proprio impegno al servizio di AIT, con poca attenzione ai vantaggi che ciò potrà procurare (che sono assai modesti e platonici!) e molta fiducia nella collaborazione di tutti.

Anche da "ex" la mia collaborazione, se necessaria, sarà totale.

Un caro saluto a tutti!

Enzo Pranzini

Introduzione

L'analisi di dati acquisiti da sensori montati su piattaforme aeree o satellitari, per applicazioni legate all'area urbana, è di grande interesse e attualità. In effetti, la maggior parte della popolazione mondiale vive in agglomerati urbani di diverse dimensioni e i problemi di questi agglomerati si riflettono su di essa.

Ai ricercatori interessati a queste aree il telerilevamento offre una possibilità di avere contemporaneamente viste d'insieme e particolari precisi, grazie alla presenza in orbita di sensori satellitari con diverse caratteristiche di risoluzione spaziale e spettrale. In questo senso sia la possibilità di utilizzare dati da satellite ad altissima risoluzione, acquistabili a prezzo relativamente basso, sia quella di avere a breve una costellazione di satelliti ad orbita bassa, il sistema Cosmo/SkyMed sponsorizzato dalla Agenzia Spaziale Italiana, si presentano come occasioni da non perdere per le quali la comunità scientifica, anche italiana, si deve continuamente aggiornare e preparare. Contemporaneamente, esistono possibilità da tempo in atto per la caratterizzazione di elementi del tessuto urbano mediante piattaforme aeree di nuova generazione che hanno anche in Italia notevoli attori a livello industriale.

Per queste motivazioni è stato organizzato un primo workshop italiano di rilevamento urbano da piattaforma aerea e satellitare, con il contributo dell'Associazione Italiana Telerilevamento (AIT) e della Società Italiana di Fotogrammetria e Topografia (SIFET) e in collaborazione con l'Università di Pavia e la Fondazione Università di Mantova. Sponsorizzazione scientifica è stata fornita inoltre fornita dalla Associazione docenti Universitari di Topografia E Cartografia (AUTEC) e dal Consorzio Nazionale Interuniversitario per le Telecomunicazioni (CNIT). Il workshop aveva l'ambizione di tradursi in una reale occasione di coordinamento e di confronto per i ricercatori italiani nel campo del rilevamento urbano, grazie anche alla presenza di qualificati relatori invitati di livello internazionale.

Le principali ragioni di questo workshop erano dunque:
  a) la volontà di verificare l'interesse nella comunità scientifica, industriale e degli utenti a questo tema;
  b) la possibilità di aumentare la (limitata) visibilità di questo settore del rilevamento, che pure ha ampie implicazioni di tipo applicativo;
  c) il fornire un luogo per scambio di opinioni e di metodologie di ricerca, ma anche di risultati pratici ed esperienze di progetto;
  d) il definire insieme priorità, linee di ricerca promettenti e applicazioni mature, in modo da fare il punto sulla situazione e progettare insieme per il futuro.

Alcune delle sfide che il workshop si riprometteva di affrontare si può dire che siano state vinte. In particolare:
  a) il workshop è riuscito a stabilire una decisa maturità della comunità scientifica italiana nell'ambito del telerilevamento urbano, che però necessita di una solida interazione con il mondo industriale e con il mondo degli utenti per poter estrinsecare le proprie potenzialità;
  b) sono state inoltre definite alcune priorità immediate per la ricerca e/o l'applicazione, con particolare enfasi sulla situazione italiana ma senza perdere d'occhio l'Europa, in particolare il monitoraggio globale per l'ambiente e la sicurezza (GMES), integrazione di dati telerilevati e GIS (geomatica), integrazione di sensori differenti (data fusion), analisi tridimensionale delle aree urbane.

La sfida che è invece rimasta anche dopo la conclusione del workshop è quella di definire una metodologia che permetta uno scambio di informazioni più efficace e continuo tra tutti coloro che sono coinvolti in attività nello specifico ambito del telerilevamento urbano, nonché un più efficace coinvolgimento di tutti gli attori (università e centri di ricerche, piccole e medie imprese, enti locali e nazionali) in questo processo di osmosi. A questo proposito le azioni successive a questo workshop sono state due: da una parte sono state rese pubbliche le presentazioni effettuate durante la due giorni di Mantova. Esse sono direttamente reperibili a partire dalla pagina web della conferenza http://geomatica.unipv.it/urbanworkshop e permettono a chi non è potuto intervenire di capire quali siano le linee di lavoro emerse in quella sede.

La seconda azione è stata la realizzazione di questo numero speciale della Rivista Italiana di Telerilevamento, rappresentativo delle capacità e delle potenzialità della comunità di chi si occupa di telerilevamento urbano, un vero "biglietto da visita" verso chi non conosce le potenzialità di questi strumenti o li conosce poco. Come si noterà, i lavori qui riportati sono di grande interesse e presentano applicazioni del telerilevamento che, in molti casi, hanno una rilevanza pratica immediata. Il telerilevamento urbano riveste indubbiamente notevole utilità in situazioni di emergenza e di disastri naturali, come pure per aree in paesi in via di sviluppo e laddove le informazioni del rilevamento a terra, più precise ma più faticose da recuperare su aree geograficamente estese, non sono disponibili.

Gli esempi nei lavori qui riportati indicano però che ci sono situazioni in cui il sensore remoto riesce ad essere utile complemento ai dati a terra anche in zone molto ben caratterizzate, quali le aree urbane del nostro paese. La speranza degli autori e del coordinatore di questo numero speciale è che questi esempi possano essere di stimolo ad un ripensamento per quanti hanno sempre guardato con scetticismo a questa branca del telerilevamento.

Paolo Gamba, Università di Pavia

DEM reconstruction accuracy of multi-channel SAR Interferometry in urban areas

Giancarlo Ferraiuolo[1], Federica Meglio[2], Vito Pascazio[3] and Gilda Schirinzi[2]

[1]Dipartimento di Ingegneria Elettronica e delle Telecomunicazioni, Università di Napoli Federico II, via Claudio 21 - 80125 Napoli
[2]DAEIMI, Università di Cassino, via Di Biasio 43 - 03043 Cassino. E-mail: schirinzi@unicas.it
[3]Dipartimento per le Tecnologie, Università di Napoli Parthenope, via Medina 40 - 80133 Napoli

Abstract
Interferometric SAR (InSAR) systems allow the estimation of the height profile of the Earth surface. When the observed scene is characterized by high ground slopes or exhibits strong height profile discontinuities (like in urban areas), the height reconstruction obtained from a single interferogram is ambiguous, since the solution of the estimation problem is not unique. To solve this ambiguity and restore the solution uniqueness, multiple interferograms, obtained with different baselines and/or with different frequencies, have to be used (multi-channel InSAR). In this paper a brief review of three multi-channel InSAR methods, together with an analysis of achievable reconstruction accuracy, is presented.
Keywords: SAR Interferometry, Digital Elevation Model reconstruction, statistical estimation

Riassunto
I sensori SAR interferometrici (InSAR) consentono di stimare il profilo altimetrico della superficie terrestre. Quando nella scena osservata sono presenti profili di quota caratterizzati da grandi pendenze o, in alcuni casi, da salti di quota, come nel caso delle aree urbane, la ricostruzione del profilo a partire da un singolo interferogramma è ambigua, poiché la soluzione del problema di stima non è unica. Per risolvere questa ambiguità, e per ristabilire quindi l'unicità della soluzione, bisogna seguire un approccio diverso, basato sull'uso di più interferogrammi ottenuti con baselines e/o con frequenze di lavoro differenti (sistemi InSAR multi-canale). In questo lavoro dopo una breve ricapitolazione relativa a tre metodologie InSAR multi-canale, viene effettuata un'analisi delle accuratezze ottenibili per la ricostruzione dei profili di quota.
Parole chiave: Interfermetria SAR, ricostruzione DEM, stima statistica

Introduction
Interferometric Synthetic Aperture Radar Systems (InSAR) allow the estimation of the altimetric profile of the imaged scene on the Earth surface. In fact, the ground height profile is related to the SAR interferometric phase through a known mapping. The Digital Elevation Model (DEM) of the ground can be then estimated by means of a phase unwrapping (PhU) operation [Bamler, 1998]. PhU consists essentially in a two dimensional (2D) profile reconstruction in the interval $(-\infty,\infty)$ starting from the wrapped phase values in the interval $(-\pi,\pi)$. Since there is an infinite number of height profiles that can be wrapped in the same interferometric phase, the PhU is an ill-posed problem, unless proper regularity constraints are imposed. The constraint that is commonly imposed forces the (unwrapped) phase jumps between adjacent pixels to be less that π. This assumption implies the absence of high slopes

and strong discontinuities in the ground elevation profile, and then it can be very critical for some application, such as the elevation mapping of urban areas, where height elevation discontinuities are very frequent due to the presence of buildings.

To recover the solution uniqueness without imposing any constraint on the height profile of the ground surface it is necessary to use multiple interferograms acquired at different frequencies [Pascazio, 2001] and/or with different baselines [Ferretti, 2001] (multi-channel InSAR systems). In this way it is possible to reconstruct also height profiles exhibiting strong discontinuities, like happens in the case of urban areas.

Recently, different methods based on maximum likelihood estimation have been developed [Pascazio, 2001; Ferretti, 2001; Pascazio, 2002]. The number of interferograms required to obtain a reliable reconstruction depends significantly on the operating frequencies, on the used baselines values and on the coherence value of each interferogram. In the lack of a sufficient number of interferometric acquisitions at different frequencies and/or with different baselines, it is possible to increase the number of data by sub-band filtering the (complex) images obtained using wide-band systems, in such a way to form a larger number of couples of interferometric images at reduced spatial resolution [Pascazio, 2001]. In this way we obtain an increase of the number of data at expenses of a spatial resolution reduction. To reduce this effect, a technique based on Maximum a Posteriori (MAP) estimation has been introduced [Ferraiuolo, 2004]. It uses an a priori Markovian (MRF) statistical distribution for the 2D height profile [Li, 2001]. The MRF, through the assignment of a parameter set (hyperparameters), that can be tuned using an unsupervised procedure, allows the description of the local interaction between couples of pixels.

The recent availability of low spatial resolution DEMs of a large part of the Earth surface, computed by the interferometric data acquired by the SRTM C-band SAR system and free distributed by NASA (http://edc.usgs.gov/products/elevation.html), has brought new insights in the solution of the elevation profile estimation problem [Sangh-Ho, 2005]. This problem can be, in fact, formulated in the following way: given an assigned number of interferograms related to the same area and an inaccurate external DEM at a low spatial resolution, find a more accurate DEM estimation at a higher spatial resolution. This is a problem of great interest in elevation mapping of urban areas, since SRTM DEM does not reproduce the building height profile.

In this paper we investigate the possibility of obtaining more accurate height estimation starting from multiple interferograms.

Multi-channel DEM estimation

An InSAR multi-channel systems is based on the collection of more interferograms acquired in a multi-frequency or in a multi baseline configuration. The system geometry in the multi-baseline case is shown in Figure 1, for the case of two baselines.

The SAR multi-baseline interferometric phase signals can be expressed as:

$$\phi_{0n}(i,j) = \left\langle \alpha B_{\perp n} h(i,j) + w_n(i,j) \right\rangle_{2\pi} \qquad n = 1,..,N \quad i = 1,...,M \quad j = 1,...,P \qquad [1]$$

where (i, j) are the discrete range and azimuth co-ordinates, and

$$\alpha = \frac{4\pi}{\lambda R_0 \sin\theta} \, , \qquad\qquad [2]$$

λ is the wavelength, $B_{\perp n}$ is the orthogonal baseline of the n-th SAR interferogram, θ is the view angle, R_0 is the distance to the centre of the scene, w_n is the phase decorrelation noise and $\langle \cdot \rangle_{2\pi}$ represents the "modulo-2π" operation.

Figure 1 - Two-baselines InSAR system geometry.
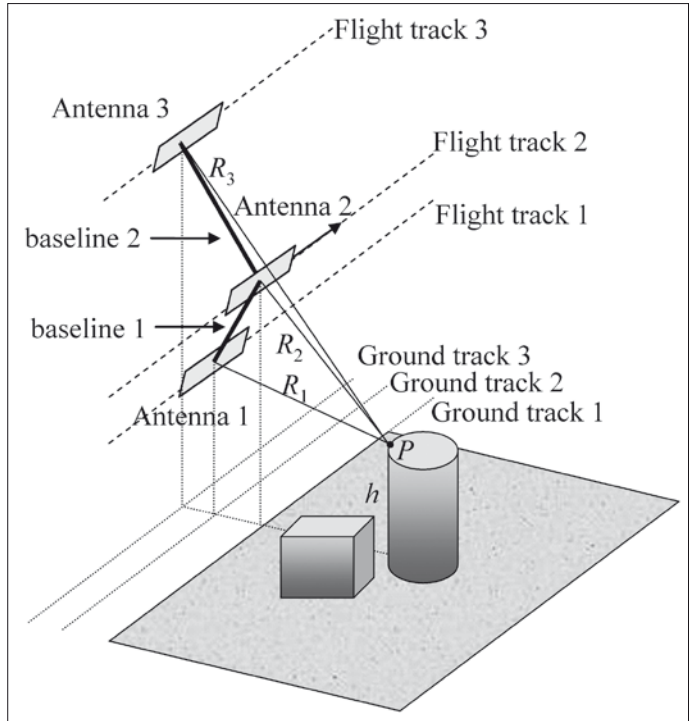
The problem consist in estimating the height values $h(i, j)$, starting from the N measured wrapped phases $\phi_{0n}(i, j)$. In the following of this section we will describe these different methods to estimating the height values.

ML Height Estimation (ML-HE)

If we consider the height values $h(i, j)$ to be deterministic parameters, a maximum likelihood (ML) estimation approach [Kay, 1993], which amounts to find the values of $h(i, j)$ maximizing the likelihood function, can be followed.

In the case of a single interferogram, the ML function is given by [Pascazio, 2001]:

$$f\big(\phi(i, j)\big|h(i, j)\big) = \frac{1}{2\pi} \frac{1 - |\gamma|^2}{1 - |\gamma|^2 \cos^2(\phi - \alpha B_\perp h)} \times \left\{ 1 + \frac{|\gamma| \cos(\phi - \alpha B_\perp h) \cos^{-1}\big[-|\gamma| \cos(\phi - \alpha B_\perp h)\big]}{\big[1 - |\gamma|^2 \cos^2(\phi - \alpha B_\perp h)\big]^{1/2}} \right\} \quad [3]$$

where $\phi \in [-\pi, \pi)$ is the measured wrapped phase (given the actual elevation h) and γ is the coherence [Bamler, 1998].

The plot of Equation [3] for a given measured value of the interferometric phase ϕ, for a given height value ($h = 300$ meters), for the baseline $B_\perp = 568$ m, with the ENVISAT-ASAR system parameters of Table 1, is shown in Figure 2 for two different coherence values ($\gamma = 0.7$ for the solid line, $\gamma = 0.37$ for the dotted).

It shows very clearly that the likelihood function is periodic with period $T_h = 2\pi / \alpha B_\perp =$

Table 1 - ENVISAT-ASAR parameters.

ENVISAT-ASAR parameters	
Wavelength λ	0.0566 m
View angle θ	30°
Range distance R	700 Km
Pulse bandwidth Δf	16 MHz

$\lambda R_0 \sin\theta / 2B_\perp = 17.25$ m, and then it exhibits an infinite number of global maxima. The ML solution is given by:

$$\hat{h}_{ML}(i,j) = \arg\max_h f\big(\phi(i,j)\big|h(i,j)\big)$$ [4]

Problem [4] admits the following infinite solutions:

$$\hat{h}_{ML} = \frac{\phi}{\alpha B_\perp} \pm kT_h, \qquad k = 0,1,2,\ldots\ .$$ [5]

In order to solve this ambiguity problem, we have to consider additional independent phase measures ϕ_n, ($n=1,\ldots,N$), for instance acquired with different baselines. The multi-channel likelihood function, in this case, is given, by supposing statistical independent interferometric phases, by:

$$F_{mf}\big(\Phi(i,j)\big|h(i,j)\big) = \prod_{n=1}^{N} f\big(\phi_n(i,j)\big|h(i,j)\big),$$ [6]

where $\Phi(i,j) = [\phi_1(i,j)\ \phi_2(i,j)\ \ldots\ \phi_N(i,j)]^T$ is the measured wrapped phase data vector. Note that we have now a wrapped phase data vector for each position (i,j) on the ground. The plot of Equation [6] for a given height value ($h = 300$ meters), for two values of the measured interferometric phases at the baselines $B_{\perp 1} = 98$ m and $B_{\perp 2} = 568$ m, with the ENVISAT-ASAR InSAR system parameters of Table 1, and for $\gamma_1 = 0.7$, is shown in Figure 3.
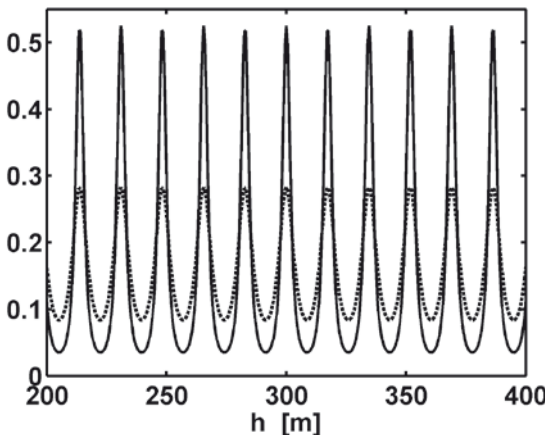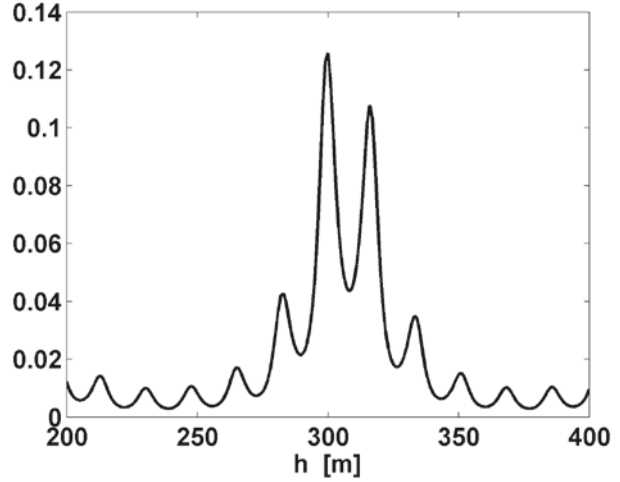

Figure 2 - Single-baseline ML function for a given measured value ϕ of the interferometric phase corresponding to $h = 300$ m, and for different coherence values ($\gamma = 0.7$ for the solid line, $\gamma = 0.37$ for the dotted line).

Figure 3 - Two-baselines ML function for two measured values of the interferometric phase, with $B_{\perp 1} = 70$ m, $B_{\perp 2} = 568$ m, and $\gamma_1 = 0.7$.

Note that the multiplication of the two single-baseline likelihood functions avoids multiple global maxima, which are present in each single frequency likelihood function, at least in the range of interest for *h*.

ML Local Plane Parameter Estimation (ML-LPPE)

In order to exploit the potentiality of the multi-frequency ML-HE method summarized in the previous section, we need a large number of independent measures. In [Pascazio, 2001] it is shown that satisfactory results can be obtained with wide band SAR sensors, by sub-band partitioning the overall Fourier spectrum. The wide band allows to preserve satisfactory spatial resolutions after the sub-band partitioning. For non-wide band SAR systems, we will need other additional independent phase measures. Moreover, we remind that the ML-HE is performed for each position, independently from the surrounding ones.

A better performance can be achieved if we introduce some relations among the height value in a given pixel and the height values in an assigned cluster of neighbouring pixels. The basic idea for obtaining such a result is presented in the following.

Let us consider the height profile $h(\cdot, \cdot)$ to be recovered. Suppose that N independent measures of wrapped phases are available to estimate $h(i, j)$. Consider now a "cluster" $\mathcal{N}_{ij}$ of pixels formed by the pixel (i, j) itself, and by N_P-1 neighbouring pixelss. For the cluster $\mathcal{N}_{ij}$ we have at our disposal $N_P \mathrm{x} N$ independent measures of wrapped phases (N for each pixel of the cluster).

If the height surface in the neighborhood $\mathcal{N}_{ij}$ can be approximated by a plane, the height $z(p, q)$ of each pixel belonging to $\mathcal{N}_{ij}$ can be approximated by the Equation:

$$z (p, q) = a (i, j)p + b (i, j)q + c (i, j) \qquad (p, q) \in \mathcal{N}_{ij} \qquad [7]$$

We *a-priori* exclude from Equation [7] the unrealistic case of a perfect vertical plane ($a \to \infty$ and/or $b \to \infty$) on a discrete domain.

Then, in place of estimating the height values for each position independently from the others as performed by the ML-HE method, we can search the parameters $a(i, j)$, $b(i, j)$, and $c(i, j)$ of the planes best approximating in the ML sense the true height profile of the pixels belonging to $\mathcal{N}_{ij}$, starting from the $N_P \mathrm{x} N$ wrapped phase values. This ML estima-

tion is repeated for each (i, j). We refer to this approach in the following as the Maximum Likelihood local planes parameters estimation (ML-LPPE) method. In Figure 4, a rectangular neighbouring system constituted by $N_P = 9$ positions has been considered. Then, if we introduce for each (i, j), the vector of unknown parameters $\boldsymbol{x}_{ij} = [a(i, j)\ b(i, j)\ c(i, j)]^T$ and the vector of measured phase data $\Theta_{ij} = \{\Phi^T(p,q),\ (p,q) \in \mathcal{N}_{ij}\}$, where the vectors $\Phi(p, q)$ were first introduced in Equation [6], we can recast the estimation problem in the following way:

$$\hat{\boldsymbol{x}}_{ij} = \arg \max_{\boldsymbol{x}} L\!\left(\Theta_{ij}\,\middle|\,\boldsymbol{x}_{ij}\right) = \arg \max_{\boldsymbol{x}} \prod_{(p,q)\in\mathcal{N}_{ij}} F_{mf}\!\left(\Phi(p,q)\,\middle|\,\boldsymbol{x}_{ij}\right) =$$

$$= \arg \max_{\boldsymbol{x}} \prod_{(p,q)\in\mathcal{N}_{ij}} \prod_{n=1}^{N} f\!\left(\phi_n(p,q)\,\middle|\,\boldsymbol{x}_{ij}\right), \qquad [8]$$

where

$$f\!\left(\phi_n(p,q)\,\middle|\,\boldsymbol{x}_{ij}\right) = \frac{(2\pi)^{-1}\!\left(1-|\gamma_n|^2\right)}{1-|\gamma_n|^2 \cos^2\!\left(\phi_n(p,q)-\alpha B_{\perp n}(ap+bq+c)\right)}$$

$$\times \left\{ 1 + \frac{|\gamma_n|\cos\!\left(\phi_n(p,q)-\alpha B_{\perp n}(ap+bq+c)\right)}{\left[1-|\gamma_n|^2 \cos^2\!\left(\phi_n(p,q)-\alpha B_{\perp n}(ap+bq+c)\right)\right]^{1/2}} \times \right. \qquad [9]$$

$$\left. \times \cos^{-1}\!\left[-|\gamma_n|\cos\!\left(\phi_n(p,q)-\alpha B_{\perp n}(ap+bq+c)\right)\right] \right\}$$

and where $\gamma_n = \gamma_n(p, q)$, $a = a(i, j)$, $b = b(i, j)$, and $c = c(i, j)$.
In this way we search for the parameters $\hat{a}(i,j)$, $\hat{b}(i, j)$, $\hat{c}(i,j)$ of the local plane approximating (in the ML sense) the true height surface. The final height estimate is given by the value assumed at the "central" point (i, j) of the neighbouring system $\mathcal{N}_{ij}$:

$$\hat{h}(i, j) = \hat{a}(i, j)i + \hat{b}(i, j)j + \hat{c}(i, j), \qquad \forall(i, j) \qquad [10]$$

In this case we estimate 3 parameters (a, b, and c) starting from $N_P \times N$ ($N_P = 9$ in Figure 4) wrapped phase measures, improving of a factor $N_P/3$ the ratio between the number of independent measures and the number of unknowns with respect to the multi-frequency ML-HE estimation. Note that the maximization [10] has to be performed with respect to three parameters. Global maximization algorithms such as Simulated Annealing in the Metropolis version can be used for this purpose [Li, 2001]. As such methods can be very time consuming, to improve numerical efficiency, a parallelization can be very easily introduced due to the local nature of the algorithm.

MAP Height Estimation
In terms of the MAP approach the unknown image is seen as a random vector H with a known *a-priori* statistical distribution. This distribution is usually defined in such a way to
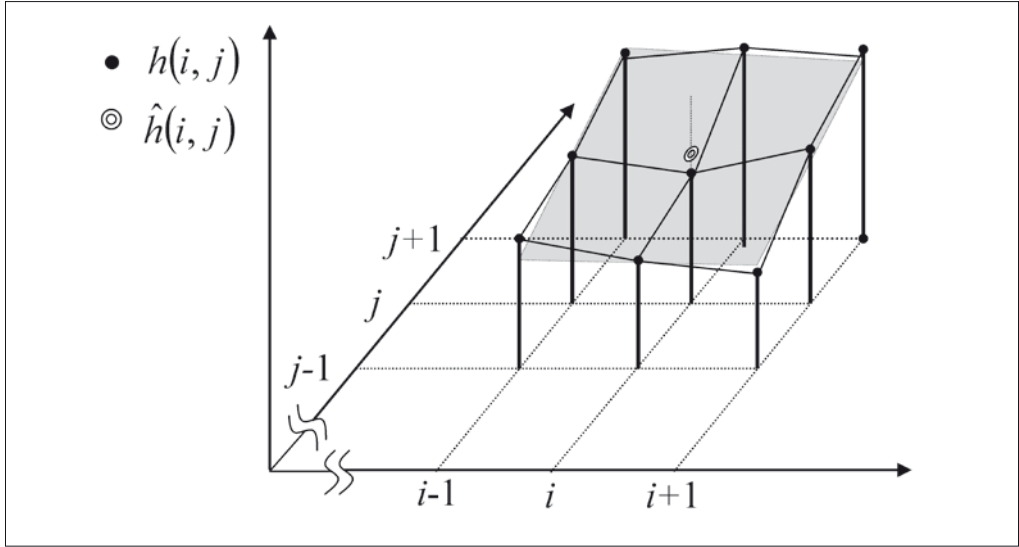
Figure 4 - Plane (grey) approximating the true profile for position (i,j) in the grid, for a neighbouring system consisting of N_P= 9 positions: ● true height values; ⊙ height values approximated by the plane.

assign high probability to particular pixel configurations. In our case, being the unknown image representative of the elevation of a geographic area, a strong contextual pixel information is very likely to be. In particular, we assume that the unknown images can be modelled as a *Markov Random Field* (MRF) [Li, 2001], a general image model able to represent contextual pixel information.

In particular, we choose a Gaussian Markov Random Field (GMRF) [Li, 2001] as *a-priori* model, whose expression is:

$$g(\boldsymbol{h};\sigma)=\frac{1}{Z(\sigma)}\exp\left\{-\sum_{s=1}^{M\times P}\sum_{k\in\mathcal{N}_s}\left[\frac{(h_s-h_k)^2}{2\sigma_{sk}^2}\right]\right\},\qquad [11]$$

where $\mathcal{N}_s$ is the *neighbourhood system* of s-th pixel[1] and σ_{sk} are the *hyperparameters,* representative of the local characteristics of the image h, whose values are related to the spatial variations: the higher the probability that the differences $(h_s - h_k)$ assume large values, the higher the value of σ_{sk}. With such definition, the *local* GMRF model in Equation [11], by mean of the *hyperparameters*, well adapts to describe the image *local* nature, leading to a powerful and general model, well-suited to represent a wide class of height profiles. The *hyperparamet*ers have to be estimated starting from the measured interferograms [Ferraiuolo, 2004], in order to correctly represent the unknown image.

The *incomplete data* ML hyperparameter estimation problem, *i.e.* the estimation from the measured interferograms $\boldsymbol{y}=[\Phi_1^T\ \Phi_2^T\cdots\Phi_{M\times P}^T]^T$, is typically solved iteratively, using the

---

[1] We change in the MAP framework the notation to denote pixels (s in place of *ij*) to avoid in this case a too complicated notation.

Expectation-Maximization (EM) algorithm [Li, 2001]. It is possible to derive a closed form (similarly to [Saquib, 1998]) of the expression of the hyperparameter estimation update at (z+1)-*th* step of the EM algorithm:

$$\sigma_{sk}^2 (z+1) = E\left[(h_s - h_k)^2 \,\Big|\, \boldsymbol{y}, \sigma_{sk}(z) \right]$$ [12]

For the evaluation of the expected-value, thanks to ergodicity of posterior distribution [Geman, 1984], we can approximate this expected-value by "time" averaging [Ferraiuolo, 2004].

The local estimation of hyperparameters is very powerful, because it allows to localize the flat regions and the discontinuities of the image, taking into account the local characteristics of the profile, and generating a hyperparameter *map* for the profile. This is particularly important for urban area applications. Once the hyperparameters have been estimated, the MAP estimation is given by:

$$\hat{\boldsymbol{h}}_{MAP} = \arg\max_{\boldsymbol{h}} \ln \prod_{s=1}^{M \times P} F_{mf}\left(\Phi_s | h_s\right) g\left(\boldsymbol{h}, \hat{\sigma}\right) =$$

$$= \arg\min_{\boldsymbol{h}} \left[\sum_{s=1}^{M \times P} \sum_{k \in \mathcal{N}_i} \left[\frac{(h_s - h_k)^2}{2(\hat{\sigma}_{sk})^2} \right] - \sum_{s=1}^{M \times P} \ln F_{mf}\left(\Phi_s | h_s\right) \right].$$ [13]

Summarizing, the proposed solution procedure consists of two steps:
  1. ML estimation of the hyperparameter vector σ.
  2. MAP estimation of the height profile *h*.

We use the *Simulated Annealing* [Li, 2001] algorithm to isolate the modal value. However, it is well know that this algorithm is excessive time demanding, because it works to avoid the risk of be trapped in local-minima solutions. On the contrary, deterministic algorithms are very sensitive to the presence of local solutions, but they have in general faster convergence. As a consequence, it turns out to be affordable a semi-deterministic solution, which guarantees a good grade of effectiveness in terms of reliable convergence, and at the same time a realistic convergence time. Moreover, we found out that the knowledge of the *hyperparameter* map is very effective to avoid local-minima in the image formation process, and consequently we adopt the following strategy to solve the problem: after hyperparameter estimation, we initialise the reconstruction algorithm with an high probability sample of the image, generated from the sampling, and starting from it we get the solution by ICM (Iterated Conditional Modes) algorithm [Li, 2001], which is deterministic (it is equivalent to Simulated Annealing with temperature *T* fixed to zero), and then it is very fast. The algorithm complexity grows linearly with the height image dimension.

DEM estimation accuracy

In the previous section we presented three methods to estimate height profiles from multiple interferograms. To assess the methods performances, in terms of the quality of the used estimator, we have to evaluate its bias and variance, and briefly discuss the role of the choice of the baselines.

To obtain a reliable height estimation two main points have to be faced:

1) *Height ambiguity interval*: The single interferogram likelihood function is periodic. The multi-channel likelihood function is given by the product of function with different

periods. Then, if the baselines are properly chosen, the multi-channel likelihood function exhibits, in principle, a unique maximum. However, due to the finite precision floating point representation, several maxima will be still present in practice. This problem can be easily managed by using a small value for one of the baselines, in such a way to have a large period. When an inaccurate low resolution a priori DEM is available, the smallest baseline can be chosen in such a way to have a period grater than the *a priori* DEM accuracy.

2) *Reconstruction accuracy*: The reconstruction accuracy can be evaluated by means of the Cramer-Rao Lower Bounds (CRLB) [Kay, 1993], representing the minimum variance of the reconstruction error that would be obtained using an efficient estimator. It depends on the interferograms coherence and on the adopted baselines. Given the relationship (1) between the measured phase and the height *h,* we expect the CRLB decrease when baselines increase. However, the spatial decorrelation effect due to the baseline increase has also to be taken into account [Zebker, 1992]. The behavior of the CRLB for the three estimators is presented in the following sections.

CRLB for ML Height Estimation

As the CRLB refers to the estimation of the height profile values, and as there is not any dependence of the estimation method on the position (i, j), for the sake of notational simplicity we set $h=h(i, j)$ and $\Phi=\Phi(i, j)$.

The CRLB for the estimation of the height h with the HE method is given by [Kay, 1993]:

$$CRLB_h = \frac{1}{E\left[\left(\frac{\partial \ln F_{mf}(\Phi|h)}{\partial h}\right)^2\right]},$$
[14]

where $E[.]$ denotes statistical expectation with respect to the pdf $F_{mf}(\Phi|h)$ of the data (the wrapped phase vector Φ) given by Equation [6]. It depends on the baselines and on the coherence, which in its turn is dependent on the baseline, through the relation [Zebker, 1992]:

$$\gamma = \gamma_0 \left(1 - \frac{2\cos\theta \, \rho_y B_\perp}{\lambda R_0}\right),$$
[15]

where γ_0 is the coherence related to atmospheric conditions and to the thermal noise, $\rho_y=c/(2\Delta f \sin\theta)$ is the ground range resolution and the other symbol are defined in Table 1. Note that the critical baseline value

$$B_{\perp c} = \frac{\lambda R_0}{2\cos\theta \, \rho_y}$$
[16]

corresponds to the complete decorrelation of the interferometric images, which cannot be used to form the phase interferogram.

The CRLB has been evaluated using Monte Carlo simulation. Its behaviour for the case of two baselines with the ENVISAT-ASAR system parameters of Table 1 and $\gamma_0=0.7$, is shown in Figure 5. The minimum baseline has been fixed at the values of 70 m, 98 m, and 163.3 m, corresponding to ambiguity height intervals of 140 m, 100 m, and 60 m (that are approximately comparable with the accuracy of the SRTM DEM distributed by NASA).
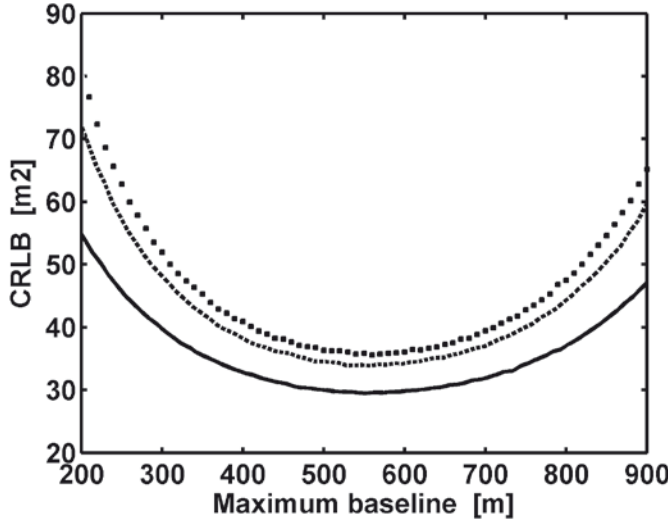
Figure 5 - Two-baselines CRLB for the ML-HE estimator for γ_0= 0.7 and $B_{\perp min}$=70 m (dotted), $B_{\perp min}$= 98 m (dashed) and $B_{\perp min}$= 163.3 m (solid).

The maximum baseline value has been changed with continuity. The obtained CRLB curve exhibits a minimum for a value of the second baseline approximately equal to 568 m, that is quite near to $B_{\perp c}/2$=603 m.

CRLB for ML Local Plane Parameter Estimation

Concerning the CRLB for the estimation of the vector x with the LPPE method, note that if the origin of the reference system in Equations [7] and [10] is positioned on the current value (i, j), the estimation of the height value reduces to the estimation of the coefficient c [Pascazio, 2002]. Consequently, we are interested in the evaluation of the CRLB for c. This is given by [Kay, 1993]:

$$CRLB_c = \left[\mathbf{I}^{-1}(x)\right]_{33} ,$$

$$\mathbf{I}(x)= E \begin{bmatrix} \left(\dfrac{\partial \ln L}{\partial a}\right)^2 & \dfrac{\partial \ln L}{\partial a}\dfrac{\partial \ln L}{\partial b} & \dfrac{\partial \ln L}{\partial a}\dfrac{\partial \ln L}{\partial c} \\ \dfrac{\partial \ln L}{\partial b}\dfrac{\partial \ln L}{\partial a} & \left(\dfrac{\partial \ln L}{\partial b}\right)^2 & \dfrac{\partial \ln L}{\partial b}\dfrac{\partial \ln L}{\partial c} \\ \dfrac{\partial \ln L}{\partial c}\dfrac{\partial \ln L}{\partial a} & \dfrac{\partial \ln L}{\partial c}\dfrac{\partial \ln L}{\partial b} & \left(\dfrac{\partial \ln L}{\partial c}\right)^2 \end{bmatrix} \qquad [17]$$

where L stands for $L(\Theta|x)$, $E[.]$ denotes statistical expectation with respect to the pdf $\Pi_{(p,q)\in \mathcal{N}} F_{mf}(\Phi(p, q)/x)$ of the data (the wrapped phase vector $\Theta=\Phi^T(p, q)$, $(p, q)\in \mathcal{N}$), I(x) is the Fisher Information Matrix [Kay, 1993], $I^{-1}(x)$ is its inverse, and $[.]_{33}$ denotes the third element of the matrix diagonal.

The CRLB behaviour for LPPE method in the same case of Figure 5 is shown in Figure 6. Also in this case the obtained CRLB curve exhibits a minimum for a value of the second baseline approximately equal to $B_{\perp c}/2$, but its value is much lower than the one obtained with the ML-HE estimator.

Figure 6 - Two-baselines CRLB for the LPPE estimator for γ_0= 0.7 and $B_{\perp min}$= 70 m (dotted), $B_{\perp min}$= 98 m (dashed) and $B_{\perp min}$= 163.3 m (solid).
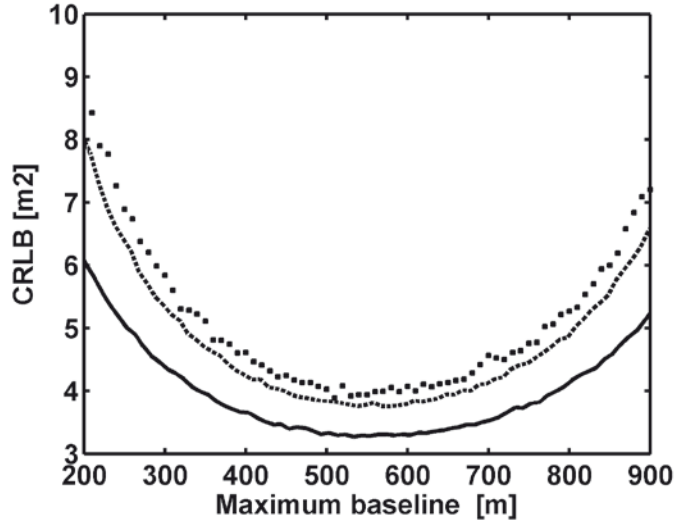
However it has to be reminded that in this case (strongly non linear ML estimation) the CRLB only represents a theoretical lower bound for the variance of the searched parameters. The variance of the actual ML estimate will tend to the CRLB asymptotically, and very often it is very difficult to *a-priori* define what "asymptotically" means.

CRLB for MAP Height estimation
The bound for random parameter case can be derived considering that in the Bayesian framework the Fisher information matrix consists of two parts [Van Trees, 2001]:

$$I_T(h) = I_L(h) + I_P(h). \quad [18]$$

$I_L(h)$ denotes the Fisher information matrix for the unknown image h relative to the likelihood term, whose element is:

$$\left[\mathbf{I}_L(\boldsymbol{h})\right]_{ij} = -E\left[\frac{\partial^2 \prod_s^{M \times P} F_{mf}\left(\Phi_s | h_s\right)}{\partial h_i \partial h_j}\right]. \quad [19]$$

Due to the statistical independence of phase noise in different pixels, such matrix is diagonal. $I_P(h)$ denotes the Fisher information matrix for the unknown image h relative to the *a priori* term, whose element is:

$$\left[\mathbf{I}_P(\boldsymbol{h})\right]_{sk} = -E\left[\frac{\partial^2 \ln g_H(\boldsymbol{h})}{\partial h_s \partial h_k}\right] = E\left[\frac{\partial^2}{\partial h_s \partial h_k}\sum_m \sum_{n \in \mathcal{N}_m} \frac{(h_m - h_n)^2}{2\sigma_{mn}^2}\right] =$$

$$E\left[\frac{\partial}{\partial h_s}\left(2\sum_{m\in\mathcal{N}_k}\frac{(h_k-h_m)}{2\sigma_{km}^2}-2\sum_{n\in\mathcal{N}_k}\frac{(h_n-h_k)}{2\sigma_{nk}^2}\right)\right]=E\left[\frac{\partial}{\partial h_s}\left(\sum_{m\in\mathcal{N}_k}\frac{(h_k-h_m)}{\sigma_{km}^2}+\sum_{n\in\mathcal{N}_k}\frac{(h_k-h_n)}{\sigma_{nk}^2}\right)\right] \quad [20]$$

$$\overset{\sigma_{km}=\sigma_{mk}}{=}E\left[\frac{\partial}{\partial h_s}\left(2\sum_{m\in\mathcal{N}_k}\frac{(h_k-h_m)}{\sigma_{km}^2}\right)\right],$$

where we have supposed that the MRF is symmetric ($\sigma_{km}=\sigma_{mk}$).

$$\left[\mathbf{I}_P(\boldsymbol{h})\right]_{sk}=-E\left[\frac{\partial^2\ln g(\boldsymbol{h};\sigma)}{\partial h_s\partial h_k}\right]=\begin{cases}2\sum_{m\in\mathcal{N}_s}\dfrac{1}{\sigma_{sm}^2}, & s=k\\[12pt]-2\dfrac{1}{\sigma_{sk}^2}, & s\neq k,\quad s\in\mathcal{N}_k\\[12pt]0, & s\neq k,\quad s\notin\mathcal{N}k\end{cases} \quad [21]$$

$I_P(h)$ is a diagonal predominant matrix. As an example, if we consider an isotropic MRF ($\sigma_{sm}=\sigma_s$), the elements on the main diagonal are 8 times larger than the other non null elements out of the main diagonal. The resulting matrix $I_T(h)$ given by [18] provides, after inversion, the lower bound for the variance of the estimated height values. In particular, the covariance matrix of any estimator of H will satisfy the following condition: the matrix

$$\mathbf{C}_{\hat{H}}-\mathbf{I}_T^{-1}(\boldsymbol{h}) \quad [22]$$

is positive semidefinite, and the CRLB of the of s-th image pixel will be given by:

$$CRLB_{h_s}=\left[\mathbf{I}_T^{-1}(\boldsymbol{h})\right]_{ss} \quad [23]$$

Figure 7 - Two-baselines CRLB for the MAP estimator for $\gamma_0=0.7$ and $B_{\perp min}=70$ m (dotted), $B_{\perp min}=98$ m (dashed) and $B_{\perp min}=163.3$ m (solid), for a Gaussian profile with an average hyperparameter $\sigma_{ave}=82$.
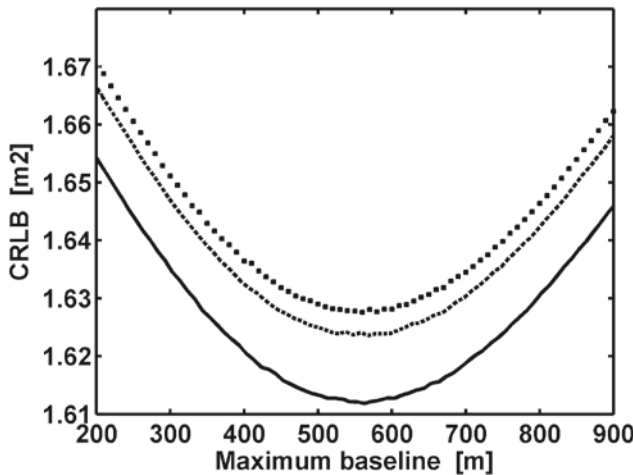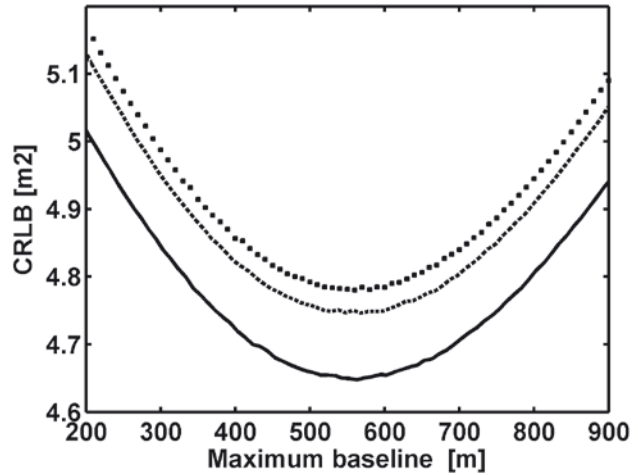
Figure 8 - Two-baselines CRLB for the MAP estimator for γ_0=0.7 and $B_{\perp min}$= 70 m (dotted), $B_{\perp min}$= 98 m (dashed) and $B_{\perp min}$= 163.3 m (solid), for a Gaussian profile with an average hyperparameter σ_{ave}= 147.

In order to qualitatively discuss Equation [23], we can note that, as also matrix $I_T(h)$ is a diagonal predominant matrix (is the sum of a diagonal and a diagonal predominant matrix), its inversion will be ruled by its diagonal, and its inverse matrix can be approximated by a diagonal matrix whose elements can be approximated by the inverse of the elements of the $I_T(h)$ diagonal. The larger the element of the $I_T(h)$ diagonal, the smaller the element of the $I_T^{-1}(h)$ diagonal, and then the smaller the CRLB for the estimated parameter.

Larger elements of the $I_T(h)$ diagonal will be generated by small hyperparameter values. Then, for flat-like height profiles, typical of some regions of urban areas, the reconstruction will be very accurate also in case of low coherence values, whereas for steep height profiles, like in correspondence of height discontinuities, the reconstruction will be less accurate.

The CRLB behaviour for the MAP method in the same case of Figures 5 and 6 is shown in Figures 7 and 8 for two different Gaussian shaped height profiles, exhibiting an hyperparameter slowly changing across the image. As expected, the CRLB values are lower for the first profile, less steep than the second and characterized by an average hyperparameter value σ_{ave}= 82, while the latter is characterized by an average hyperparameter value σ_{ave}= 142, confirming the above qualitative discussion. However, in both cases, we note a weak sensitivity to the baseline values, and then to the images coherence, due to the dominant contribution of the a priori term.

Numerical results

To test the quality of the MAP based estimation method, we considered the height profile shown in Figure 9a (2D representation) and Figure 9b (3D representation). In Figure 9c, the reference hyperparameter's map is represented, too.

With reference to this profile, we simulated the interferometric phases, obtained with 5 baselines with a minimum value $B_{\perp min}$= 98 m and maximum value $B_{\perp max}$= 568 m and γ_0= 0.7. The MAP estimation of height profile (2D and 3D representations) are in Figures 10a and 10b, whereas the ML estimation of hyperparameter's map is in Figure 10c. The obtained reconstruction exhibits a mean square error (mse) of 2.25 m^2, which is also the variance of the image pixel MAP estimation. However, this is only a mean value of the local image variance; in particular, in a region where the estimated mean hyperparameter value is 0.8, the mse is equal to 0.35 m^2, in a region where the estimated mean hyperparameter
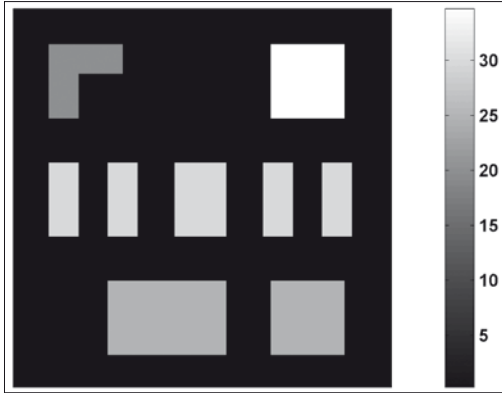
Figure 9a - 2D Reference height profile.   **Figure 10a - 2D Reconstructed height profile.**
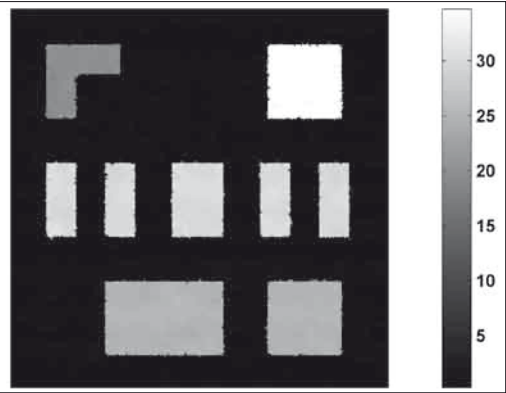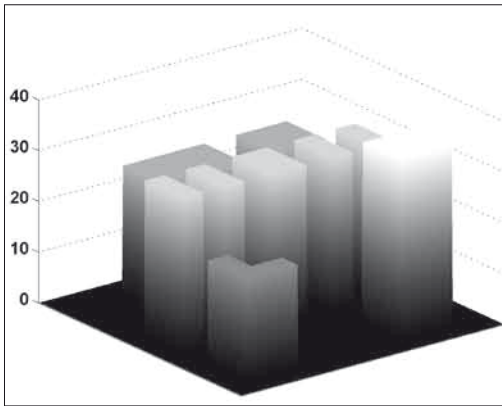
Figure 9b - 3D Reference height profile.   **Figure 10b - 3D Reconstructed height profile.**
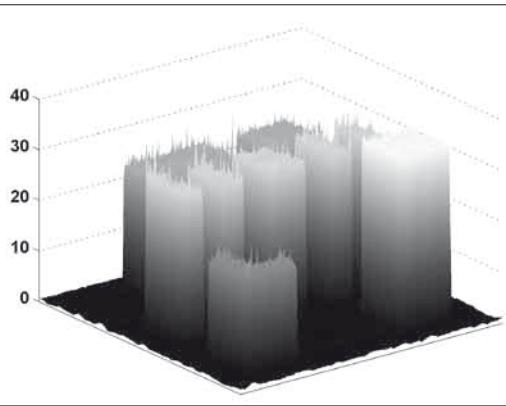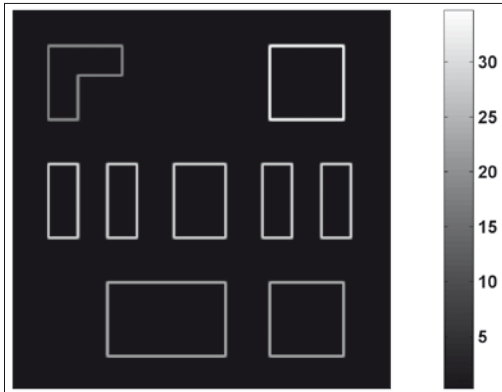
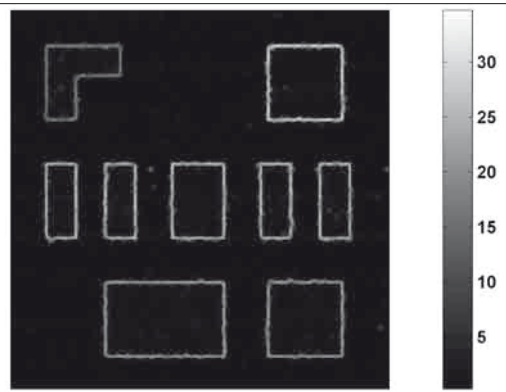**Figure 9c - Reference hyperparameter's map.**   **Figure 10c - Estimated hyperparameter's map.**

value is 3.35, the mse is equal to 8.41 m^2. However, in presence of elevation profiles of regular geometrical structure, these effect can be reduced by a proper post-processing taking into account also the image intensity.

The above observations confirm the behavior of the CRLB previously presented for the MAP estimator, in the sense that for regions characterized by low values of the hyperparameters a good quality height estimation can be obtained.

Conclusions

It has been proved in the scientific literature that (in the lack of strong a-priori information) only methods based on multi-channel data (multi-frequency and/or multi-baseline) can allow to recover steep or discontinuous height profiles, as the ones characterizing urban contexts.

The multi-channel height reconstruction algorithms proposed in this paper, based on statistical estimation methods, belong to this category.

Such a capability to recovering discontinuous height profiles is in principle obtained using at least two different baselines or frequencies. In this paper we showed how to choose the different baselines, showing that there is an optimal choice from the point of view of the minimization of the CRLB of the estimated quota values. Moreover, as expected, the best results in terms of estimation accuracy are obtained with the MAP height estimation method, and the performance further improve in the case of low hyperparameter values.

As far as the computational burden of the multi-channel algorithms proposed is concerned, the necessary processing time can be sometimes significantly larger than the one relative to conventional single-channel algorithms. But, it is as much true that there are classes of profile (steep and discontinuous) that can be reconstructed *only* adopting multi-channel based algorithms, and this circumstance can justify the use of time consuming algorithms.

The algorithms have been proved on simulated data, and further work will be made to demonstrate the full applicability of the method to real cases. Preliminary experiments on real data have been made on multi-channel SAR data relative to ground-based SAR [Ferraiuolo, 2004].

References

Bamler R., Hartl P. (1998) - *Synthetic Aperture Radar Interferometry*. Inverse Problems, 14: R1-R54.

Ferraiuolo G., Pascazio V., Schirinzi G. (2004) - *Maximum a Posteriori Estimation of Height Profiles in InSAR Imaging*. IEEE Geosci. Rem. Sensing Letters: 66-70.

Ferretti A., Prati C., Rocca F. (2001) - *Multibaseline Phase Unwrapping for INSAR Topography Estimation*. Il Nuovo Cimento, 24: 159-176.

Geman S., Geman D. 1(984) - *Stochastic Relaxation, Gibbs' Distributions, and Bayesian Restoration of Images*. IEEE Trans. Pattern Anal. Mach. Intell., 6: 721-741.

http://edc.usgs.gov/products/elevation.html (accessed 20th Oct. 2005).

Kay S.M. (1993) - *Fundamentals of Statistical Signal Processing*. Estimation Theory, Prentice-Hall.

Li S. Z. (2001) - *Markov Random Field Modelling in Computer Vision*. (Berlin: Springer, Computer Science Workbench).

Pascazio V., Schirinzi G. (2001) - *Estimation of Terrain Elevation by Multi-Frequency Interferometric Wide Band SAR Data*. IEEE Signal Processing Letters, 8: 7-9.

Pascazio V., Schirinzi G. (2002) - *Multi-Frequency InSAR Height Reconstruction through Maximum Likelihood Estimation of Local Planes Parameters*. IEEE Trans. Image Proc., 11: 1478-1489.

Saquib S.S., Bouman C.A., Sauer K.A. (1998) - *ML Parameter Estimation for Markov Random Fields with Applications to Bayesian Tomography*. IEEE Trans. Image Proc., 7: 1029-1044.

Sang-Ho Y., Jun J., Zebker H., Segall P. (2005) - *On merging high- and low-resolution DEMs from TOPSAR and SRTM using a prediction-error filter.* IEEE Trans. Geosci. Remote Sens., 43: 1682 -1690.

Van Trees H. L. (2001) - *Detection, Estimation, and Modulation Theory.* (New York: John Wiley & Sons).

Zebker H.A., Villasenor J. (1992) - *Decorrelation in interferometric radar echoes.* IEEE Trans. Geosci. Remote Sens., 30 (5): 950-959.

Ferraiuolo G., Leva D., Nico G., Pascazio V., Schirinzi G., Tarchi D. (2004) - *A Bayesan Technique for Terrain Mapping Using Multi-Frequency Ground Based Interferometric SAR Systems.* 2004 Int. Geoscience and Remote Sensing Symposium (IGARSS'2004), Anchorage (USA), pp. 469-472.

Low and high resolution differential interferometry monitoring of the Sarno urban area

Leonardo Cascini[1], Settimio Ferlisi[1], Gianfranco Fornaro[2], Dario Peduto[2], Michele Manunta[2,3] and Giovanni Zeni[2,4]

[1]Dipartimento di Ingegneria Civile, Università di Salerno, via Ponte don Melillo - 84084 Fisciano (Salerno). E-mail: dpeduto@unisa.it
[2]IREA-CNR, via Diocleziano 328 - 80124 Napoli.
[3]Dipartimento di Ingegneria Elettrica ed Elettronica, Università di Cagliari, p.zza d'Armi - 09100 Cagliari.
[4]Dipartimento di Ingegneria Ambientale e Fisica, Università della Basilicata, via dell'Ateneo Lucano 10 - 85100 Potenza.

Abstract

The paper discusses the potentialities offered by the Small BAseline Subset (SBAS) Differential Synthetic Aperture Radar Interferometry (DInSAR) technique to investigate subsidence phenomena in urban areas and, thus, to provide useful information for the detection of building damage susceptibility, the management of groundwater resources and the urban planning. With reference to Sarno town (Italy), whose urban area is affected by ground surface settlements ascribed to groundwater withdrawals, results at low and high resolution, obtained by using data acquired by ERS-1/2 and Envisat satellites in the period from 1992 to 2004, are shown.
Keywords: Synthetic Aperture Radar (SAR), Differential Interferometry (DInSAR), ground deformation

Riassunto

La memoria evidenzia le potenzialità d'impiego di una tecnica DInSAR di elaborazione di dati da Radar ad Apertura Sintetica (SAR) nello studio di fenomeni di subsidenza che interessano aree urbane. Con riferimento al territorio del Comune di Sarno (Italia), affetto da cedimenti della superficie topografica ascrivibili allo sfruttamento delle risorse idriche sotterranee, si illustrano i risultati delle analisi condotte a bassa ed alta risoluzione con l'algoritmo Small Baseline Subset (SBAS) su dati acquisiti dai satelliti ERS 1 e 2 ed Envisat nel periodo 1992-2004; si discute, infine, il contributo che tali studi possono offrire nella individuazione delle più adeguate strategie di mitigazione degli effetti al suolo.
***Parole chiave**: Radar ad Apertura Sintetica (SAR), Interferometria Differenziale (DInSAR), deformazioni del suolo*

Introduction

Differential SAR Interferometry (DInSAR) is an advanced technique that combines two or more SAR images of the same area to measure ground deformations with accuracy on the wavelength order. Since the first description of the technique [Gabriel et al., 1989] and first demonstrations with real (ERS-1) data [Goldstein et al., 1993; Massonnet et al., 1993], most of the DInSAR applications were based on single interferograms (*i.e.* using an image pair) or few interferograms. The advantage of these simple configurations is the flexibility to provide (qualitative) information on ground surface deformations, even with a reduced SAR data availability. More recently, significant technological improvements have been achieved by

jointly using a large number of DInSAR images [Ferretti et al., 2000; Strozzi et al., 2001; Berardino et al., 2002; Mora et al., 2003]. Two different types of strategy are generally pursued: the coherence-based technique [e.g. Berardino et al., 2002; Mora et al., 2003] and the so-called permanent scatterers (PS) [Ferretti et al., 2000] method. Both techniques involve a large number of images, that allow the reduction of error sources (atmosphere, etc.) and thus a fully quantitative deformation monitoring [Crosetto et al., 2005].

At present several examples of DInSAR application are available, regarding various natural phenomena related, for instance, to crustal deformation [Vadon and Sigmundsson, 1997], earthquakes [Massonnet et al., 1993; Stramondo et al., 1999], volcanoes [Massonnet et al., 1995; Borgia et al., 2000] and slope instabilities [Hilley et al., 2004].

Another relevant activity is represented by the extensive validation of the technique especially in urban areas affected by subsidence/uplift phenomena caused by either mining [Crosetto et al., 2005; Kircher et al., 2003] or water extraction [Cascini et al., 2006] or underground construction works [Jurina et al., 2003; Fruneau et al., 2003]. The main effect of the validation process is the increasingly growing reliability of the information achieved via the DInSAR technique, as in the case of the settlement induced damages to some historical buildings in Rovigo town, Italy [Jurina et al., 2003].

Main aim of this paper is to further discuss the usefulness of SBAS DInSAR technique developed at IREA-CNR (Naples, Italy) for building damage susceptibility detection, for urban planning and, once complemented by the necessary knowledge on geotechnical and hydrogeological aspects, for management of public and private groundwater withdrawals.

To this end a validation test carried out by jointly processing ERS-1/2 and Envisat data is addressed. The test area is represented by Sarno town where, during the time, noticeable settlements where locally recorded due to both an intensive groundwater extraction and a random spatial distribution of high deformable soils. The SBAS deformation analysis is carried out at low and full resolution in order to test the potentialities of the technique to monitor large and small scale deformations.

The technique

The DInSAR principle is simple and founds its basis on radar interferometry. The interference (phase difference) given by the beating (conjugate product) of the response of a target in two SAR images, acquired at different times (whose separation is commonly referred to as temporal baseline) and from different orbits (whose separation is commonly referred to as spatial baseline), is the composition of several terms that can be classified in two main categories:

   a) geometric (deterministic) terms associated to the target-to-radar path difference (scaled by the factor 4π/wavelength);
   b) stochastic phase shift (noise) terms.

Mathematically, we can express the phase difference $\Delta\phi$ related to a generic pixel as follows:

$$\Delta\phi = \Delta\phi_{geo} + \Delta n \qquad [1]$$

wherein, $\Delta\phi_{geo}$ is the geometric term and Δn the stochastic one.

Geometric contributions is induced by the target topography, for the presence of an angular view difference associated to the spatial baseline, and a possible target displacement occurring between the passes:

$$\Delta\phi_{geo} = \Delta\phi_{top} + \frac{4\pi}{\lambda}\Delta s \qquad [2]$$

wherein λ is the wavelength, $\Delta\phi_{top}$ the topographic phase component and Δs the displacement occurring between the two acquisitions projected in the line of sight.
Stochastic contributions are due to:
  1) changes of the scattering properties due to temporal modification (temporal decorrelation) and/or to the different interaction mechanisms between the electromagnetic wave and the target associated to the   angular view difference (spatial decorrelation);
  2) propagation delay variation due to the presence of the atmosphere (atmospheric bias);
  3) receiver noise contributions (thermal noise decorrelation);
  4) processing artefacts and orbital information inaccuracies.
The stochastic terms can be expressed as following:

$$\Delta n = \Delta n \_ low + \Delta n \_ high \qquad [3]$$

wherein Δn_low represents the phase term related to the atmospheric artefacts and to the orbital errors and Δn_high to the decorrelation effects, the thermal noise and processing artefacts. The former is a spatially correlated contribution and, as consequence, can be estimated by using a set of the interferograms as better explain later.
Accordingly, if stochastic contributions are "low", or "kept low" via averages or ad-hoc filtering procedures, by knowing the target height from an external Digital Elevation Model (DEM), the topography contribution can be subtracted from the interferogram (differential interferogram generation).
After topography removing, the differential phase $\Delta\phi_{diff}$ can be written as follows:

$$\Delta\phi_{diff} = ctop \cdot \Delta z + \frac{4\pi}{\lambda}\Delta s + \Delta n \qquad [4]$$

wherein Δz is the topography error associated with the external DEM, *ctop* is the phase conversion coefficient and depends on the geometric parameters of the two acquisitions, in particular, on the spatial baseline in a proportional way.
Thus, should Δz and Δn be "low" enough, the target displacement, or better, its component along the radar look direction – the radar line of sight (l.o.s.) – can be reliably measured with an accuracy of the order of the radar wavelength (5.6 cm for the C-Band radar systems mounted onboard the ERS and Envisat satellites of the European Space Agency).
Processing artefacts can be limited by using accurate algorithms for focusing and, particularly for the alignment (registration) of the two images before the image beating. Orbital information inaccuracies can be controlled because they appear as low order spatial contributions on images covering 80x80 km, such as those associated to a frame of ERS and Envisat-ASAR (ERS-like mode) data. Thermal noise decorrelation is generally negligible, unless target backscattering is somewhat low (weak targets or targets in shadow). On the other hand, spatial decorrelation is relevant only at large spatial baseline (say 150 m for ERS and Envisat case) over homogeneous scenes. This noise contribution can be tackled, by either limiting the baseline and restricting the analysis to a networks of bright target (permanent scatterers), or reduced by ad-hoc filtering techniques.
Reduction of the influence of temporal decorrelation and atmospheric bias on the phase measure is more critical issue. Temporal decorrelation [Zebker et al., 1992] has been observed, at C-Band, on time scales as short as a few hours in vegetated areas experiencing windy conditions. On the other hand, a phase correlation over several years in non-vegetated areas was demonstrated by Usai and Klees [1999]. Qualitatively arid is better than forest, dry conditions are better than wet, and long radar wavelength is better than short.

With respect to this aspect, application of the DInSAR technique to urban areas is particularly favourable. In such a case, due to the presence of stable and bright (manmade) targets, high correlation may be observed even at temporal separation of several years.

Atmospheric contribution shows correlation lengths on the order of 0.5-1 km spatial separation, and together with DEM inaccuracy, Δz in [4], which introduces errors in the topographic contribution cancellation for the generation of the differential interferogram especially at large baseline, represent a major limitation of standard two-pass DInSAR. Atmospheric contribution, that is usually independent over the takes for passes acquired at the monthly rate, and topographic inaccuracies errors can be reduced by jointly processing a large number of passes. This is the fundamental advance offered by recent multipass DInSAR techniques such as PS and SBAS, over standard two-pass differential interferometry. In fact, key points of the techniques are the joint estimation of surface deformations and residual topography contributions starting from a large number of observations. The peculiarity of SBAS, able to work with small baselines, offers the advantage of limiting the influence of topography errors and the effects of spatial decorrelation when mapping deformations at small scale over wide areas. Moreover, SBAS allows naturally the implementation of DInSAR analysis at both low and full resolution, thus providing a flexible tool for investigating small scale as well as localized ground deformations.

The first step of the SBAS algorithm is the estimation of the low resolution components [Berardino et al., 2002]: atmospheric artefacts, orbital errors, spatial low frequency deformation and DEM errors. In particular, the set of interferogram is unwrapped by applying the unwrapping operation of Costantini and Rosen [1999]. From the unwrapped phase the topographic and linear deformation components are estimated by exploiting the availability of a set of spatial and temporal baselines. Finally, after residual non linear deformation estimation, atmospheric artefacts are removed.

Then all the spatial low frequency terms are estimated, they are removed from the full resolution data in order to estimate the residual spatial high frequency velocity, deformation and topography terms [Lanari et al., 2004]. In particular, topography and linear deformation components are estimated, via a coherence maximization by exploiting the baseline dependencies, and removed; the non linear deformation component is obtained by applying the SVD method.

Finally, the achieved high and low resolution terms are added to obtain the products.

Case study

The SBAS DInSAR techniques was tested in Sarno urban area (around 30,000 inhabitants) located in the coastal graben of the Campanian Plain, Italy, extending for almost 170 km^2, bordered to the south by the carbonatic ridge of Lattari Mountains, east by the Sarno Mountains and north by the volcanic complex of the Somma-Vesuvius (Fig.1).

Due to intensive agricultural activities as well as numerous food industries, all over the highly urbanised Campanian Plain, the water demand for different uses constantly increased during the last century resulting in intensive, and sometimes uncontrolled, massive withdrawals.

The exploitation of Campanian Plain's rich water resource started since the 1940s with the construction of numerous deep wells; then, by the end of the Second World War, other huge water-catchments were built, essentially in the Lufrano zone (Fig.1). A similar intensive exploitation of the underground water resource has been carried out in Sarno area since 1960 by means of both public works built in close proximity to natural springs and private withdrawals, with a basically seasonal use, ranging up to $30 \cdot 10^6$ m^3/year.

The captation works, either inside or outside Sarno area, caused a marked lowering of the

Figure 1 - Campanian Plain (Campania Region, South Italy) and test site.

groundwater table within the urban area. The relationship between the drop in the groundwater table and the surface settlements is discussed in Cascini and Di Maio (1994). The Authors outline the presence, inside the superficial deposits, of very deformable peat layers, strongly influencing both the magnitude and the spatial distribution of the recorded settlements; moreover they furnish a preliminary relationships between the settlements and the damages recorded to the buildings.

Validation and interpretation of the results
In order to investigate several aspects of subsidence at different scales, low and full resolution processing, almost 80x80 m and 20x5 m (range-x-azimuth) pixel spacing respectively, were performed by processing 83 passes of the ERS1/2 and ENVISAT satellites between 1992 and 2004 (descending passes; track 36, frame 2781). Azimuth is approximately parallel to the North-South direction, whereas range is approximately parallel to the East-West direction.
In Figures 2a and 2b the coherent SAR pixels (marked by circles) referring to low and high resolution analyses, are shown respectively. Low resolution SAR pixels exhibit a regular spatial distribution; on the other hand, high resolution SAR pixels has an improved localization of the measures on elements where the signal attains the highest coherence (mainly building in urban areas)
The validation of the SAR data was achieved via a point-wise comparison with traditional ground levelling (mean square deviation of 0.3 mm/km) data referring to a net of 18 benchmarks, some of them corresponding to the heads of boreholes equipped with piezometers (Fig. 2a, 2b).
A first levelling survey, carried out from July 1992 to October 1993, produced four sets of topographic measurements; an additional survey has been accomplished in March 2004. Five sets of topographic measurements were thus available.
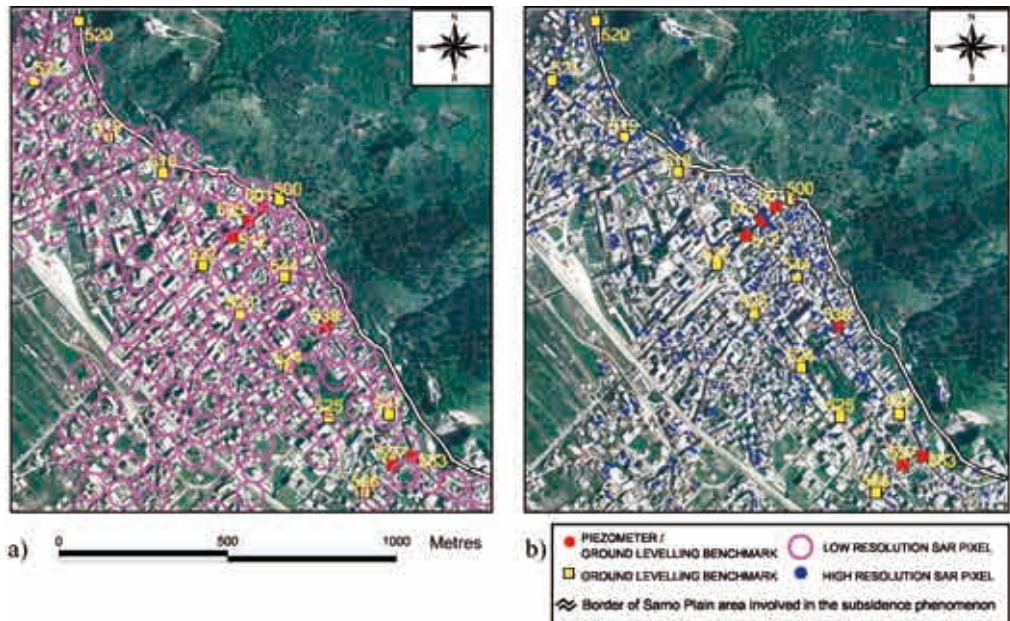
Figure 2 - Maps of Sarno Town study area: localization of ground levelling benchmarks and coherent SAR pixels at both low (a) and full (b) resolution.

Figure 3 shows a comparison between low-resolution DInSAR data and levelling results, in terms of settlements evolution in time, with reference to four ground levelling benchmarks. Particularly, the four selected circular SAR pixels (80 meter diameter) are the closest to each single benchmark and their vertical components, corresponding to the measured l.o.s. deformations, were computed assuming that the displacements mainly occurs on along the vertical direction.

The results obtained for the period 1992-1993, when the highest settlement rates occurred (Fig. 3), show a good fitting so confirming the above assumption. Furthermore they also highlight that remotely sensed settlements increase almost linearly in time from the beginning of 1995, reaching cumulative values that again fit well the most recent available levelling measurements (March 2004). This result agrees with the spatial distribution of cumulative ground settlements [Cascini et al., 2006] whose magnitude increase where the thickest peat layer were recovered [Cascini and Di Maio, 1994].

As far as the validation of full-resolution DInSAR analysis [Lanari et al., 2004] is concerned, Figure 4 shows the comparison between the evolution of ground surface settlements in time, deriving from SAR and geodetic data, for two sample benchmarks. Both diagrams confirm a good fitting, like previously obtained for low resolution data (Fig. 3), albeit the full-resolution DInSAR settlement refers to a mean value computed, for a fixed time, on a smaller area.

A key point of the full resolution SAR data is the precision in estimating the residual topography that allows accurate geo-localization of the pixels monitored by the DInSAR technique.

Although effects of sidelobes, that concentrate in ground view geometry, can be frequent in urban areas, the presence of more than a single phase centre can turn out to be a useful tool
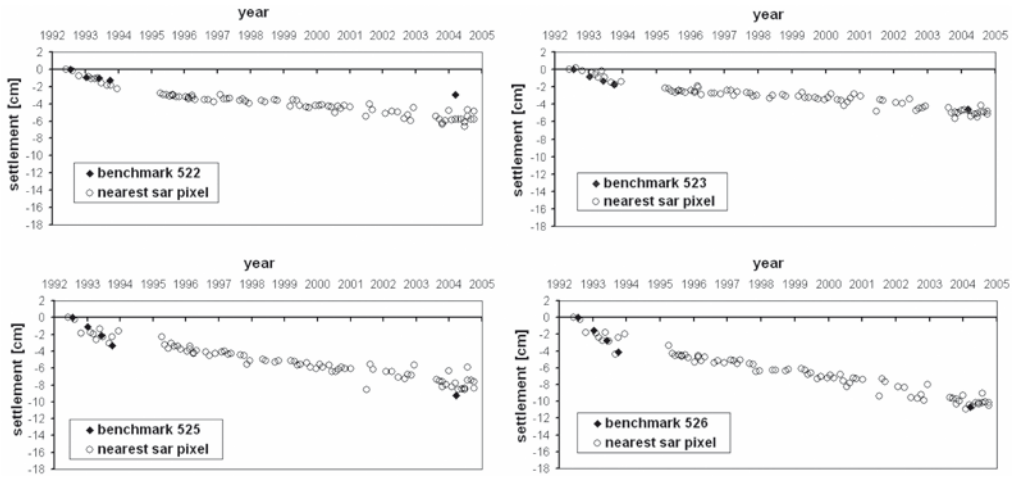
Figure 3 - Settlement point-wise comparisons (from low resolution SAR and ground levelling data).
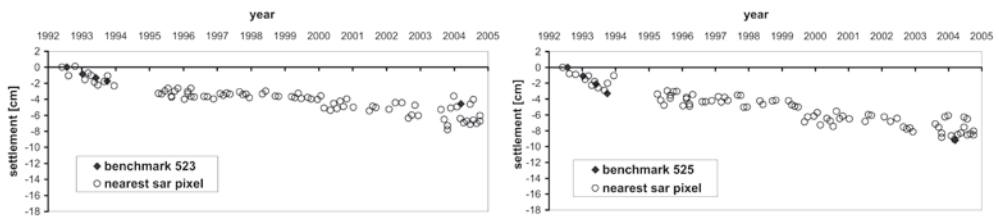

Figure 4 - Settlement point-wise comparisons (from full resolution SAR and ground levelling data).
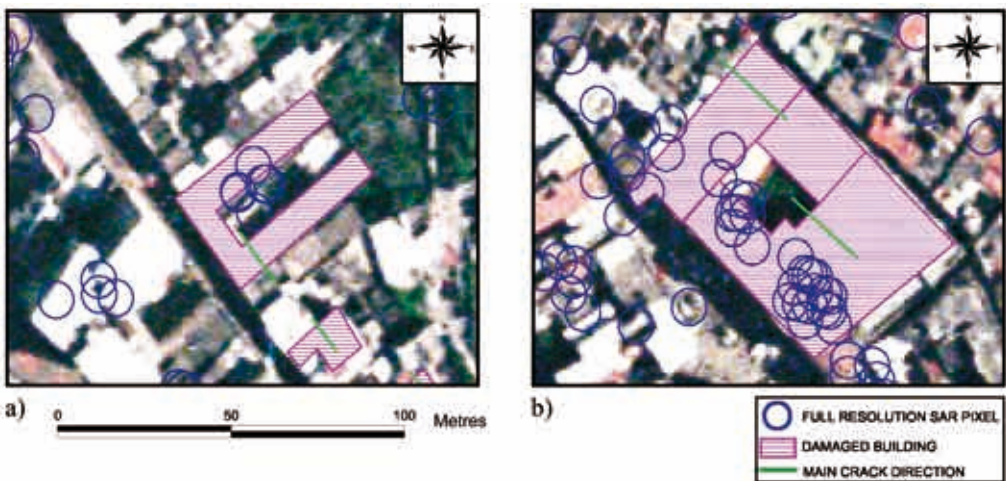
Figure 5 - Close-up view of the spatial distribution of coherent SAR pixels detected at full resolution on damaged buildings.

in the detection of the local effects, in terms of spatial settlement distribution, induced by the subsidence phenomenon.

It is worth observing that, in most cases, detected coherent pixels are located on building roofs (Fig. 5a), so improving the knowledge on the building behaviour in time, especially when several pixels are available (Fig. 5b). Moreover, the assumption of a hyperbolic-type settlement trend in time could allow back-analyses aimed to determine the beginning and the end of the subsidence phenomenon [Viggiani, 1999].

As far as the relationship between the magnitude of settlements (both absolute and differentials) and the building damage occurrence is concerned, a first attempt at "urban scale" was made by Cascini et al. (2006) who used low resolution DInSAR data referring to the urban area of Sarno. In particular, the deformation gradient magnitude, computed on the ground pixel grid starting from SAR measured settlements, was compared with the localization of recorded damages in ancient low-rise masonry buildings with shallow footings (Fig. 6). It is worth pointing out that the main directions of damages, often consisting of vertical cracks, seem to be almost normal to the gradient deformation direction shown in Figure 6 as arrows. Similar evidence is shown for the r.c. framed buildings, signed with the number 1 and 2 in Figure 6.

Finally, the use of full-resolution SAR data for pursuing similar purposes at "building scale" is not straightforward since SAR data ought to be point-wise validated by geodetic measurements just within the pixel area.

Result exploitation perspectives

A comprehensive study of a subsidence phenomenon and its related effects calls for several aspects to be adequately investigated such as ground surface settlements, building damage distribution, subsurface stratigraphy, underground water regime, etc.

Figure 6 - Deformation gradient map of the investigated area and spatial distribution of damaged buildings [Cascini et al., 2006].

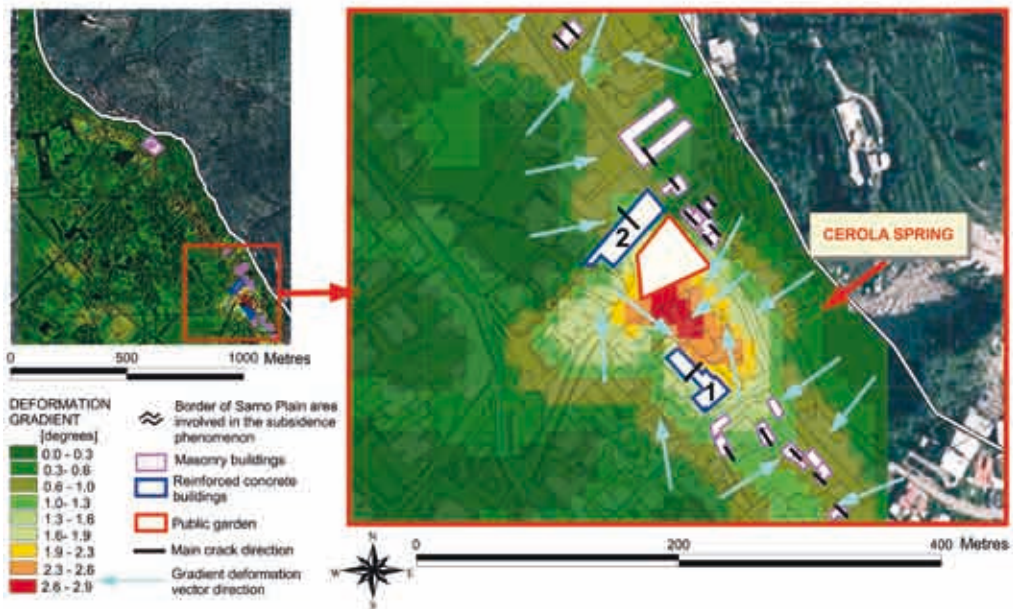With reference to ground-surface settlements, the results obtained via low-resolution analysis over Sarno urban area highlight that DInSAR technique is able to furnish settlement data in agreement with the measures achieved via traditional optical levelling. Such encouraging results suggest that low-resolution SAR data could be used in an early detection of ground surface settlements over large areas. This is, for instance, the case of the Campania Region, that is widely affected by subsidence phenomena due to huge groundwater withdrawals.

Of course, such purpose must be pursued by a systematic validation of the obtained results inside sample areas, with the aid of conventional monitoring systems. At this regard a further contribution can be furnished by other remote sensing techniques, *i.e.* GPS monitoring, that can allow the reduction of systematic errors generally affecting SAR data processing, especially when the analysis focuses on short critical periods where only few satellite data may be available.

Once an accurate building damage survey is also available, the DInSAR technique can be used to identify the relationships between causes (ground settlements) and effects (building damages). This is again the case of Sarno urban area where the deformation gradient of the ground surface, obtained via remote sensing, matches the spatial distribution of the damaged buildings (building damage susceptibility).

Of course, the knowledge improvement on building damage susceptibility calls for a deepening of the role played by the contributing factors on the subsidence phenomenon. Referring to the case of Sarno urban area, they can be identified by the spatial distribution of deformable peat layers and the groundwater regime [Cascini and Di Maio, 1994]. Thanks to the available DInSAR maps, the effects produced by such factors seem to be easily highlighted once accurate *in-situ* investigation are performed.

As far as full-resolution analysis is concerned, the use of a grid cell of at least 20x20 m, allows to improve the results - regarding, for instance, the spatial settlement distribution and their influence on the building response - obtained via low-resolution analysis; to this aim, a more detailed building survey, including structure typologies and damages, and further *in-situ* investigations, are required.

Moreover, the achieved results at full resolution could be profitably improved via a skilful joint use of remotely sensed data and available cartography (base maps and derived maps). Nevertheless, key points of investigation are the assessment of the accuracy of the DInSAR velocity measures at full resolution, that should reach a limit of 1mm/yr, and the degree of spatial density of the measures, which cannot be directly controlled, and that may impact the evaluation of the differential settlements experienced by the structures. As a consequence, despite multipass DInSAR has been successfully applied to monitor large scale deformations, such as those associated to volcanic and tectonic activity, monitoring of infrastructures and building may be challenging especially for the damage susceptibility detection.

On the basis of all the above considerations, it can be concluded that an integrated approach - based on an accurate and updated cartography, increasingly innovative techniques, traditional geodetic surveys, geotechnical investigations and analyses - must be strongly encouraged for the monitoring of urban areas affected by subsidence phenomena.

References

Berardino P., Fornaro G., Lanari R., Sansosti E. (2002) - *A new algorithm for surface deformation monitoring based on small baseline differential SAR interferograms*. IEEE Trans. Geosci. Remote Sens., 40(11): 2375-2383.

Borgia A., Lanari R., Sansosti E., Tesauro M., Berardino P., Fornaro G., Neri M., Murray J. (2000) - *Actively growing anticlines beneath Catania from the distal motion of Mount*

Etna's decollement measured by SAR interferometry and GPS. Geophysical Research Letters, 27(20): 3409-3412.

Cascini L., Di Maio C., (1994) - *Emungimento delle acque sotterranee e cedimenti dell'abitato di Sarno: analisi preliminare.* Riv. It. di Geotecnica, 28(3): 217-231.

Cascini L., Ferlisi S., Fornaro G., Lanari R., Peduto D., Zeni G. (2006) - *Subsidence monitoring in Sarno urban area via multitemporal DInSAR technique*. Int. J. Remote Sensing 27(8): 1709-1716.

Costantini M., Rosen P. A. (1999) - *A generalized phase unwrapping approach for sparse data.* Proc. of Geosci. and Remote Sensing Symposium, IGARSS '99, 1: 267-269.

Crosetto M., Crippa B., Biescas E. (2005) - *Early detection and in-depth analysis of deformation phenomena by radar interferometry*. Engineering Geology, 79: 81-91.

Ferretti A., Prati C., Rocca F. (2000) - *Nonlinear subsidence rate estimation using the permanent scatterers in differential SAR interferometry*. IEEE Trans. Geosci. Remote Sens., 38(5): 2202-2212.

Fruneau B., Deffontaines B., Rudant J.P., Le Palmentier A.M., Colesanti C., Le Mouleic S., Carnec C., Ferretti A. (2003) - *Conventional and PS differential SAR interferometry for monitoring vertical deformation due to water pumping: the Haussmann-St-Lazare case example (Paris, France).* Proc. of FRINGE 2003 Workshop, Frascati, Italy.

Gabriel A.K, Goldstein R.M., Zebker H.A. (1989) - *Mapping small elevation changes over large areas: differential radar interferometry*. J. Geophys. Res., 94 (B7): 9183-9191.

Goldstein R.M., Englehardt H., Kamb B., Frolich R.M. (1993) - *Satellite radar interferometry for monitoring ice sheet motion: application to an Antarctic ice stream.* Science, 262: 1525-1530.

Hilley G.E., Burgbman R., Ferretti A., Novali F., Rocca F. (2004) - *Dynamics of slow-moving landslides from Permanent Scatterer Analysis.* Science, 304: 1952-1955.

Jurina L., Ferretti A., Franchioni G. (2003) - *Valutazione degli effetti di scavi in falda sui cedimenti strutturali di edifici mediante utilizzo di tecniche satellitari SAR*. Convegno Internazionale "Crolli e affidabilità delle strutture" Università degli Studi di Napoli Federico II- Napoli, 15-16 maggio 2003.

Kircher M., Hoffmann J., Roth A., Kampes B., Adam N., Neugebauer H. J. (2003) - *Application of Permanent Scatterers on mining-induced subsidence*. Proceedings of FRINGE 2003 Workshop, Frascati, Italy.

Lanari R., Mora O., Manunta M., Mallorqui J.J., Berardino P., Sansosti E. (2004) - *A Small Baseline Approach for Investigating Deformations on Full Resolution Differential SAR Interferograms* IEEE Trans. Geosci. Remote Sens., 42: 1377-1386.

Massonnet D., Rossi M., Carmona C., Adragna F., Peltzer G., Feigl K., Rabaute,T. (1993) - *The displacement field of the Landers earthquake mapped by radar interferometry*. Nature, 364: 138-142.

Massonnet D., Briole P., Arnaud A. (1995) - *Deflation of Mount Etna monitored by Spaceborne Radar Interferometry*, Nature, 375: 567-570.

Mora O., Mallorqui J.J., Broquetas A. (2003) - *Linear and nonlinear terrain deformation maps from reduced set of interferometric SAR images*. IEEE Trans. Geosci. Remote Sens. 41(10): 2243-2253.

Stramondo S., Tesauro M., Briole P., Sansosti E., Salvi S., Lanari R., AnzideiI M., Baldi P., Fornaro G., Avallone A., Buongiorno M. F., Franceschetti G., Boschi E. (1999) - *The September 26, 1997 Colfiorito, Italy, Earthquakes: Modeled Coseismic Surface Displacement from SAR Interferometry and GPS.* Geophysical Research Letters, 26(7): 883-886.

Strozzi T., Wegmuller U., Tosi L., Bitelli G., Spreckels V. (2001) - *Land subsidence moni-*

toring with differential SAR interferometry. Photogramm. Eng. Remote Sens., 67(11): 1261-1270.

Usai S., Klees R. (1999) - *SAR interferometry on a very long time scale: a study of the interferometric characteristics of man-made features.* IEEE Trans. Geosci. Remote Sens., 37(4): 2118-2123.

Vadon H., Sigmundsson F. (1997) - *Crustal deformation from 1992 to 1995 at the midatlantic ridge, southwest Iceland, mapped by satellite radar interferometry.* Science, 275: 193-197.

Viggiani C. (1999) - *Fondazioni.* Hevelius Edizioni.

Zebker H.A., Villasenor J. (1992) - *Decorrelation in Interferometric Radar Echoes* IEEE. Trans. Geosci. Remote Sens., 30: 950-959.

Remote sensing for developing countries:
Landsat data and GIS

Gerardo Di Martino[1,2]**, Antonio Iodice**[2]**, Mario Pansera**[1]**, Daniele Riccio**[2] **and Giuseppe Ruello**[1,2]

[1]Ingegneria Senza Frontiere Napoli, via Bonito, 27 - 80128 Napoli. E-mail: info@isf-napoli.org
[2]Dipartimento di Ingegneria Elettronica e delle Telecomunicazioni Università di Napoli "Federico II", via Claudio, 21 - 80125 Napoli

Abstract

The efficient management of big cities requires the knowledge and the integration of the several data necessary to describe the huge number of variables that govern the urban environment evolution. In developing countries, where the resources are scarce or in-homogeneously distributed, the problem of acquiring reliable data is amplified by the unfavourable local conditions and the integration of data of different nature can be extremely complicated without appropriate instruments. In this paper we present a project devoted to develop cost-effective Geographycal Information System solutions for the integration of data (remotely sensed, social, economical, and so on). Both the organization and the technical issues of the project are presented. The project validity has been tested in the frame of a case study implemented in the city of Goma, Democratic Republic of Congo (RDC). The project was born by the collaboration with local institutions (the Don Bosco Centre and the United Nations mission in Congo (MONUC)). These organizations needed a GIS supported decision to sort out two specific problems: the location where to build up refugee camps in case of the Nyiragongo volcano eruption, and the places where to build permanent houses for local people. *In situ* data have been retrieved thanks to the cooperation with international and local organization and then efficiently organized. In addition, value added maps have been developed, providing efficient solutions for the proposed problems.
Keywords: Geographycal Information System, urban remote sensing

Riassunto

Per gestire in maniera efficiente grandi città è necessario avere a disposizione i dati necessari a caratterizzare le numerose variabili che governano l'evoluzione dell'ambiente urbano. Nei paesi in via di sviluppo, dove le risorse sono scarse e non omogeneamente distribuite, il problema dell'acquisizione di dati affidabili risulta aggravato dalle condizioni locali sfavorevoli. Spesso tali dati hanno provenienza e natura completamente diverse ed il problema della loro integrazione può risultare complicato se non viene gestito con strumenti adeguati. In questo lavoro presentiamo un progetto volto allo sviluppo di soluzioni GIS economicamente convenienti per l'integrazione dei dati (da telerilevamento, sociali, economici e così via). Presentiamo sia gli aspetti organizzativi che quelli più propriamente tecnici del progetto, testati per mezzo di un caso di studio portato avanti nella città di Goma, Repubblica Democratica del Congo (RDC). Il progetto nasce dalla collaborazione con istituzioni locali, quali il Centro Don Bosco e la missione delle Nazioni Unite in Congo (MONUC). Queste organizzazioni avevano la necessità di un supporto GIS per risolvere

due problemi specifici: localizzare zone adeguate alla costruzione, da un lato, di campi per rifugiati in caso di un'eruzione del vulcano Nyiragongo, e, dall'altro, di nuove abitazioni per la popolazione locale. I dati in loco sono stati raccolti grazie alla collaborazione di organizzazioni internazionali e locali e, successivamente, sono stati organizzati in maniera efficiente. Infine, sono state prodotte mappe a valore aggiunto, che forniscono soluzioni adeguate ai problemi proposti.
Parole chiave: *GIS, telerilevamento urbano*

Introduction

Urban settlements are complex environments, in continuous evolution, where most of the world population lives. The organization and the distribution of the available resources in big cities is an intriguing issue, which requires continuous and large scale monitoring on geophysical, economical, social and political variables. In developing countries most of the cities were developed without a rationale and the life conditions are often intolerable. In the poorest urban settlements it is difficult to have a reliable idea of the dimension of the existing problems, and local authorities are unable to get the minimal data necessary to control and efficiently drive the urban expansion. The access to the information is often limited by unsafe working conditions; in addition, traditional methods require acquisition time much higher than the typical changing rates of the studied area.

Despite the existing remote sensing instruments are already able to extract useful information in this scenario, so far scarce interest has been focused by the scientific community toward specific applications for developing countries. In this paper we present a project whose goal is the efficient exploitation of existing remote sensing sensors data and Geographical Information System (GIS) facilities in order to provide numerical instruments to support the urban monitoring and organization processes.

The implementation of such a project poses intriguing challenges for the solution of both technical and social issues. In fact, beside the typical technical problems related with integration of data coming from different sources and the efficient extraction of information from them, the definition of the GIS classification criteria has to obey to social and ethic principles, often neglected in traditional projects.

Up to now, remote sensing technology has been scarcely exploited in developing countries because of its high costs. In the presented project the acquisition and the integration of data are thought with the aim of reducing the costs, also thanks to the use of dedicated Open Source software.

The presented project has been implemented in a case study, in the city of Goma, Democratic Republic of Congo (RDC). The case study is particularly significant, because the presence of the Nyragongo volcano and the unstable political situation add further difficulties in the phase of decision-making for the city organization.

In second section we present the general project rationale, introducing the basic concepts that drive the organization and the time scheduling. The implementation of such a project is strongly influenced by the local conditions, hence in the following sections we focus our attention on the Goma case study. In particular, the third section is devoted to present the preliminary studies necessary to prepare the operative phase and to define the project objectives.

The collaboration with local actors (mainly ONU and Don Bosco centre) allowed to define two test problems related to the building of refugees camps and new safe districts in the Goma area. Finally in the fourth section the solutions proposed by the joint work of Ingegneria Senza Frontiere Napoli and the University of Napoli are presented. The last section is devoted to the final conclusions.

Remote sensing for developing countries
Project organization
The efficient implementation of an operative project requires a precise schedule of the actions to be performed. In this Section we present a general framework whose rationale is intended to be a guide for specific implementation. In particular, the operative work has been structured in seven steps, here defined as Macro Work Packages (Wp).
  − Wp1: Definition of users' requirements
  − Wp2: Existent background survey
  − Wp3: Study of technical specifics
  − Wp4: Study of resources availability
  − Wp5: Data elaboration
  − Wp6: Training
  − Wp7: Education
The first part of the project (Wp1 and Wp2) involves the preliminary study of the local situation, *i.e.* a social analysis on people actual needs. This is a crucial step in this project because it affects the fullfillment of needs felt by the local population. In addition, in this phase, it is necessary to identify typical problems of developing countries which can be studied with remote sensing techniques. As for the urban areas, we have detected four main classes of topics:
  −Water: lack of sewers and of drinkable water.
  − Enormous demographic flows, runaway development of Bidonvilles, favelas and so on.
  − Air, land and water pollution.
  − Rubbish logistic and management.
  − Management of emergencies.
In the present work we focuse our attention mainly on ready and effective urban pianification in case of emergencies and on the importance of water management in this kind of situations.
Once the object of the work has been defined, the appropriate remote sensing instruments for the identified purposes have to be chosen (Wp3, Wp4). The data useful for the project success have to be defined and the processing algorithms designed. In addition, the availability of resources (funds, hardware, software, data and so on) has to be tested, in order to dimension the project on the actual possibilities.
Then, the proposed solutions can be implemented according to the goals and the constraints identified in the previous project steps (Wp5). In this phase, the remote sensing data are interpreted, geo-coded and integrated with data of any other type. Dedicated software and solutions are implemented and the required information are retrieved from the data, in order to provide a solution to the given problem.
The last part of the project (Wp6 and Wp7) consists in the knowledge transfer phase. In fact, it is crucial that all the developed applications could be repeated by local subjects. Therefore, the know-how of the proposing group has to be shared, mainly with local operators.
The developing countries cities are very different with respect to ours, so, in order to test the validity of the proposed framework, in the following the attention is posed on the implementation of the project in the city of Goma in the Republic Democratic of Congo. The implementation of the described steps is treated with details in the next sections.

The Goma case study: preliminary studies and data collection
Users' requirements
In this Section we present a case study, developed to give an answer to the requests of Ngangi Don Bosco Center, in the city of Goma, in the Nord Kivu region of RDC. The

project has been implemented in collaboration with the ONU mission in Congo (MONUC) and the Volcanologic Observatory of Goma (OVG).

According to the project schedule outlined in the previous section, it is crucial a preliminary analysis of the Nord Kivu region specific problems, in order to define the "users' requirements". Goma is a city with nearly 400.000 inhabitants, which presents most of the typical problems of urban areas in developing countries (lack of infrastructure, of water networks, of sewers, overpopulation and so on). Since 1998, two and a half millions of people have died in the Eastern RCD from infectious diseases and malnutrition.

The city is located under the active volcano Nyragongo, which frequently destroys part of the urban area. The last Nyragongo eruption, in January 2002, burned out the city centre, making the need to find appropriate reactions to the next volcanic events arise.

Furthermore, the city is situated in an area affected by an unsafe political context. The political situation determines significant displacements of persons in the Goma area. The examined region is afflicted by a humanitarian crisis and a chronic complex emergency due to the presence of armies and armed groups of at least six countries [Baxter et al. 2002].

An analysis of the needs felt by the population, developed in conjunction with the Don Bosco center and the MONUC office for the coordination of humanitarian affairs (OCHA), which supplied us some maps, demographic data and so on, led us to focus the project on two main goals: the identification of areas with low volcanic risk, where it is possible to build permanent districts for local people and the planning of a quick strategy to locate sites where to build refugees camps.

Technical specifics and resource availability

In the context presented in the previous section, the use of remote sensing technology can be crucial in order to retrieve useful information for the project objectives. Anyway, as usual in developing countries, the available resources are scarce, sparse and unreliable. In this section we present how we collected the available data and how we re-organized them in order to have a useful database for the achievement of our tasks.

The available raw data are listed in the following:

– UN - GIS UNIT non-georeferenced maps were provided by OCHA on the Goma city centre topography and the Nord Kivu region; demography, childish mortality rate, environment and health punctual informations were also provided.

– Old non-georeferenced topographic map of Goma, made during Belgian colonialism was provided by the "Don Bosco Ngangi" center.

– Landsat ETM+ images of Nord Kivu region, acquired from the Michigan State University's Center for Global Change & Earth Observations. These data have been realized by the U.S. Geological Survey (USGS) and consist of 7 data files organized according to the Hierarchical Data Format (HDF); the sensor is the Enhanced Thematic Mapper Plus (ETM+) and the area of interest is located in between three different countries: D.R. of Congo, Rwanda e Uganda, between 1° and 1°50" south, and between 29° and 30° est. This set of data has already passed through the image restoration phase. The geodetic-cartographic system used in georeferencing our images is WGS 84 - UTM (zone 35).

Further information on local infrastructures and first aid centers were acquired via *in situ* studies in collaboration with the Ngangi center personnel and volunteers and via contacts with local authorities.

Available data could not provide useful informations if not appropriately integrated and processed. Therefore, the first step of the technical part of the project was focused on the organization of available data. In particular, we synthesized the most relevant Goma parameters in three maps, presented in the following.

Figure 1 - Recent lava flows effect in the Goma center.

We georeferenced and merged the images. We georeferenced the available data using the open-source software GRASS-GIS, commonly referred to as GRASS, a GIS used for geospatial data management and analysis, image processing, graphics/maps production, spatial modeling and visualization. In Figure 1 we present the result of our analysis concerning the areas of Goma affected by the lava flows of the Nyragongo eruption in January 2002. It is shown that the city center was strongly affected and some districts completely destroyed. One of the two main lava flows shown in the figure crossed the city and reached the Kivu lake. This lava flow destroyed the administrative centre of the city, where the most important buildings of city authorities were located. A second flow (in the center of Figure 1) destroyed two popular districts of the city, principally made up of wooden shacks. In the map the distribution of humanitarian offices and of health centers (Centres de santè) are also shown.

In Figure 2 the water supply network, as acquired by in situ surveys, is shown. The dotted

Figure 2 - Water supply in the city of Goma.

Figure 3 - Power supply in the city of Goma.

blue lines represent the drinkable water supply, the yellow ones identify the pipes destroyed by the 2002 Nyragongo eruption. The water distribution for the Goma population is not uniform. In the map in Figure 2, the darker the colour of the area, the more regular is the water supply. Note that most of the water is taken from the lake (the two uplifting points in the North-East area of the map are shown): such a procedure poses safety warnings because water contains volcanic minerals and can be often contaminated by sludge.

In Figure 3 the electrical distribution service is presented. The darker the area in the map, the more regular the electricity distribution service. Note that the richest districts (located in the North-East area of Goma) and the airport area (the straight line near the Rwanda border) are regularly reached by water and electricity supplies. Conversely, the poorest zones of the city (North of Goma) are actually not reached by water and electrical supplies.

The produced maps summarize and make easily interpretable the pre-project information. In the following Section we present the GIS applications developed to give an answer to the problems identified by our local partners.

The Goma case study: gis applications

In this Section we present the solution we provided to face the problems identified in the second section.

Identification of safe areas for new districts
Why to analyse the lava?

In order to define the criteria to classify the most dangerous districts, a preliminary study on the lava flow characteristics is required.

It is possible to identify two main Nyragongo's lava types: a fast and fluid one, known in literature as "pahoehoe", and a slow and rough one, known in literature as "AA".

The first is very dangerous for the people, because it is very fast, up to 40 Km/h. However, the "pahoehoe" lavas are not dangerous for the buildings because the pressure applied on the constructions is not very high. Conversely, the "AA" lavas are destructive for every type of building. Therefore, the knowledge of the past eruption lava composition is crucial to foresee its behaviour in case of new eruptive phenomena.

In order to do it, we made an in situ survey with the volcanologists of OVG, picking up
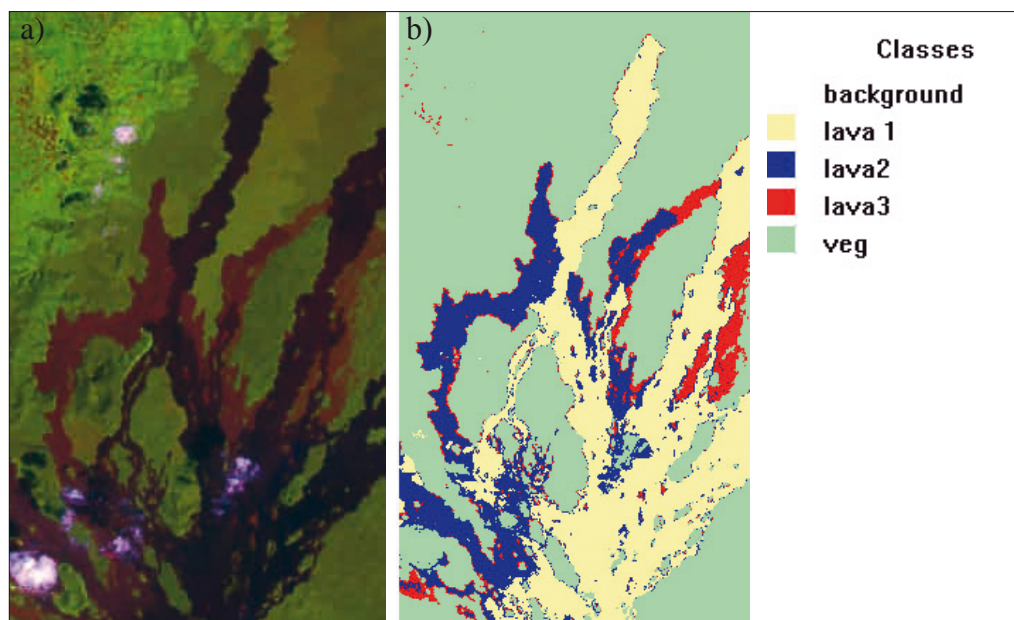
Figure 4 - a) False colour Landsat image (bands 5-4-1); b) Results of the Multi-Spec classification.

several samples of lava. But, it is impossible to reach some sites of the Nyragongo volcano because of the insecurity of the zone. Hence, remote sensing instruments are suitable to retrieve crucial informations [Flynn et al., 2002].

The Landsat data described in the second section are extremely useful for lava classification purposes. In particular, we studied the lava flows using four different techniques:

  – Study of LWIR band (8-12 µm), [Harris et al. 2002; Wright et al. 2003].
  – Image classification on singles bands with MultiSpec software.
  – Image classification on three-bands images with MultiSpec software, [Serpico 2004].
  – Index method.

We discovered that the most effective way to study the overlapped lava flows is the classification on three-bands images. With this approach we can detect and separate flows coming from up to three different eruptions. As an example, we present the supervised classification of these three different lava flows in the northern region of the Nyragongo volcano.

In Figure 4a we show the false colour image obtained by the merging of the bands 5-4-1 of the Landsat data. The obtained image has been classified via a supervised maximum likelihood criterion and the result is presented in Figure 4b. In the classified image we can distinguish three overlapped flows marked in three different colours [Serpico 2004]. The users' accuracy of the classification is adequate for the first lava type (87.7%); conversely, being the other two lava flows covered with vegetation, we obtained a good classification accuracy (96.5% for lava2 and 100% for lava3), but a poor users' classification accuracy (43.2% for lava2 and 42% for lava3) [Arnoff 1982].

With the same approach we can study the two lava streams which destroyed Goma city centre. In the classification of the region a further "urban" class has been added to show Goma buildings. The city is made essentially of wooden slums laid on the lava of volcano Nyragongo, and so it's really difficult to distinguish the flows from the urban buildings. In Figure 5 is possible to see secondary flows in the north of the city.
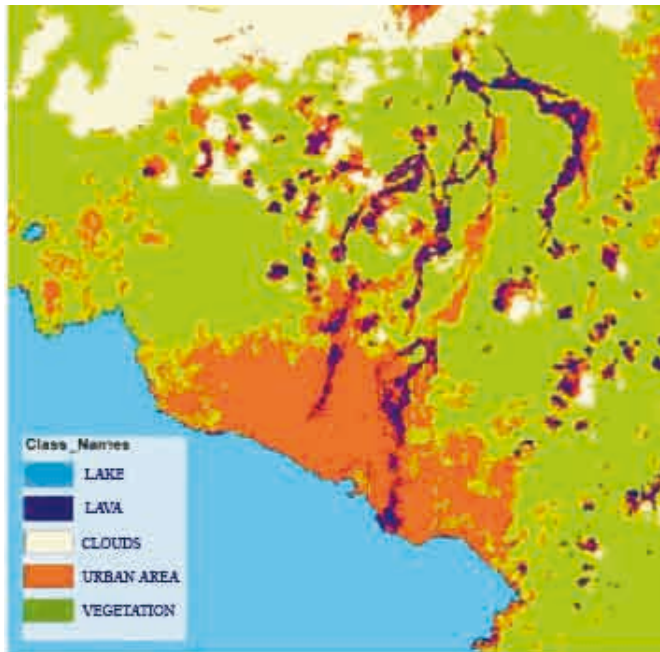
Figure 5 - Lava classification in the Goma area.

Goma city volcanic risk map

As usual in developing countries, available data are scarce and a complete risk map requires financial funding. Anyway, in this paragraph, we show that important information can be extracted by few data, via efficient GIS techniques. We generated a map to individuate the best area where to build houses for the refugees of the January 2002 eruption. The construction of the buildings is financiated by the "Don Bosco Ngangi" centre and intends to build up 200 houses with 5m x 10m base. In order to locate the most suitable place where to build up this district, we have selected four criteria (Tab.1).

The Nyragongo lava flows in the last 50 years came out from several fractures located between lake Kivu and Nyragongo's top. In Figure 6 we present a geological map provided by the OVG. During the last eruption the lava that destroyed most of the city centre spurt out from two main fractures, closer than 3 km to the city borders and identified in Figure 7 by the dashed red lines.

Using the GIS-GRASS, we identified the city areas where all the proposed criteria were fulfilled. In Figure 7 we present an easily readable map with the result of our analysis.

Table 1 - GIS buffering criteria.

Feature	Criterion	Motivation
Volcanic fractures	2 km afar	Future eruptions prevention
Roads	Less than 400m afar	Communication ways accessibility
Water pipes	Less than 400m afar	Drinkable water accessibility
Lake	More than 350 m afar	Water contamination and epidemics prevention

The red areas represent those areas in which the district for the refugees can be built with a low volcanic risk, sufficient water supply and so on.

Identification of suitable areas for refugees camps
As stated in the second section, it was also required to identify the best area where to build up an emergency camp, in case of a new volcano eruption or civil war.

The zone under study is one of the most vegetated areas in the world and is characterized by the presence of a large National Park. In this context it is crucial to monitor the vegetation around the urban settlements also because it is forbidden to build up in the National Park area.

The proposed study has been carried out also using a vegetation index, the GVI (Green Vegetation Index) [Crist et al. 1984; Crist et al. 1984] defined as follow:

$$GVI = -(0.2848 \times band1) - (0.2435 \times band2) - (0.5436 \times band3) + (0.7243 \times band4) + (0.0840 \times band5) - (0.1800 \times band7)$$
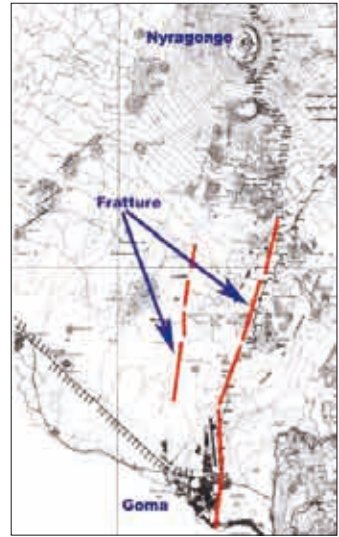
Figure 6 - OVG geological map.

Using this index we were able to distinguish very clearly on the available images the borders of the National Park of Virunga.

Note that we choose the GVI also because GRASS calculates automatically indexes generated by Tasseled Cap Transformation of Landsat images.

In order to identify the areas in where it is possible to build the refugees camps, we stated the following criteria (Tab.2).
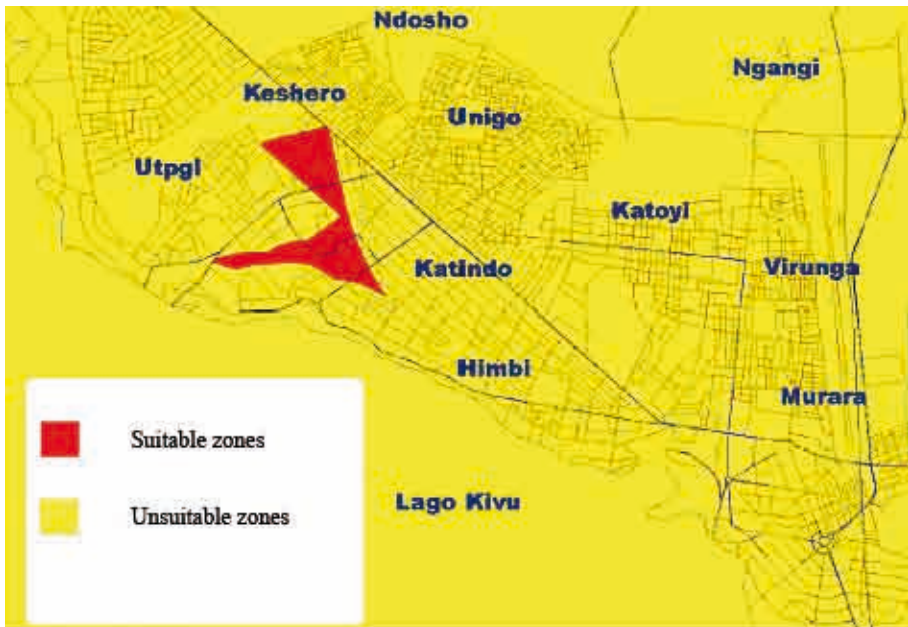
Figure 7 - Identification of areas suitable for new districts.

Table 2 - GIS buffering criteria.

Feature	Criterion	Motivation
Virunga National Park	1 km afar	Habitat and rainforest protection
Roads	Less than 500 m afar	Communication ways accessibility
City boarders	More than 1 km afar	Public order and health management
Lake	More than 400 m afar	Water contamination and epidemics prevention

In addition, we must obviously consider that we have to build the camps far away (at least 2 km) from the volcano fractures.

It's easy enough to achieve the last three criteria using GRASS on the maps we obtained and elaborated previously. On the other hand the first criterion was fulfilled working on the GVI elaborated image of the zone: from the GVI map we created a vectorial map containing the borders of Virunga National Park and then from this second map we obtained the required criterion of distance from these borders.

In this way we obtained the image shown in Figure 8 where the areas of interest are marked in green. Now we have to consider the distance from Rift Valley: as we have seen in the lava study one of the two resulting zones is just near a crack. So we have to consider only the green zone on the far left of our image.

Conclusions

In this paper an innovative project for the use of remote sensing data and GIS applications in developing countries has been presented. The project organization has been shown and a significant test case implemented. Efficient solutions for specific problems born by local organizations requirements have been proposed.

Acknowledgments
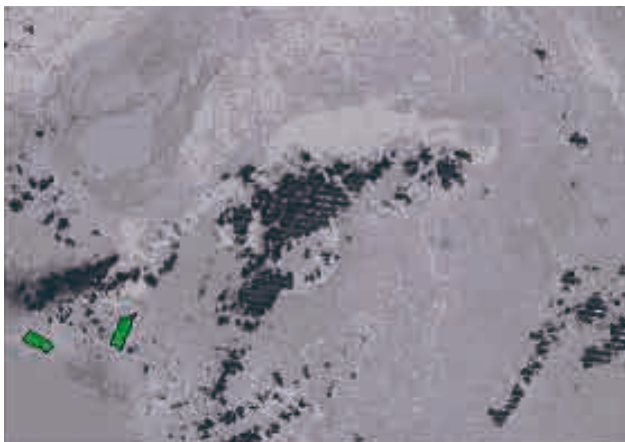
Figure 8 - Identification of areas suitable for refugee camps.

United Nation Mission in Congo and the Jaques Dureux of the Volcanologic Observatory of Goma for their support.

References

Arnoff S. (1982) - *Classification accuracy: a user approach.* Photogramm. Eng. Remote Sensing, 48:1299-1307.

Baxter P.J., Ancia A. (2002) - *Human Health and vulnerability in Nyragongo Volcano crisis in D.R. Congo.* WHO, University of Cambridge.

Crist E.P., Cicone R.C. (1984) - *Application of the Tasseled Cap Concept to Simulated Thematic Mapper Data.* Photogramm. Eng. Remote Sensing, 52(3): 343-352.

Crist E.P., Eric P., Cicone R.C. (1984) - *A physically-based transformation of thematic mapper data.* The TM tasseled cap. IEEE Trans. Geosci. Remote Sensing 22(3):256-263.

Flynn L.P., Wright R., Donegan S. (2002) - E*O-1 Observations of Volcanoes.* EO-1 SVT Meeting.

Harris A.J.L., Flynn L.P., Matìas O., Rose W.I. (2002) - *The thermal stealth flows of Santiaguito dome, Guatemala.* Geological Society of America Bulletin.

Serpico S.B. (2004) - *Classificazione statistica di immagini telerilevate del territorio.* Dip. Ing. Elettronica, Università di Genova.

Wright R., Flynn L.P. (2003) - *On the retrieval of lava-flow surface temperatures from infrared sat. data.* Geological Society of America.

Application of SAR tomography in urban areas

Francesco Serafino and Gianfranco Fornaro

Istituto per il Rilevamento Elettromagnetico dell'Ambiente (IREA), Consiglio Nazionale delle Ricerche (CNR), via Diocleziano 328 I - 80124 Napoli. E-mail: fornaro.g@irea.cnr.it

Abstract

Scattering of microwaves in urban areas is a rather complex mechanism due to the presence of a high density of structures, with high topographic variations, where responses of different targets may interfere in the same resolution cell. This work discusses the results obtained via a coherent multiple-view processing, namely the 3D SAR tomography technique based on the Singular Value Decomposition, to discriminate targets in elevation. With respect to classical SAR interferometry, that allows mapping the height only of the mean or dominant target, the technique here discussed provides a full three-dimensional reconstruction capability, by providing measure of the scattering power distribution at different heights in the same resolution cell. Results obtained by processing real data acquired by the satellites ERS-1/2 on the Napoli urban area are presented.
Keywords: SAR 3D focusing, SAR tomography

Riassunto

Lo scattering in aree urbane è un fenomeno complesso dove, a causa della presenza di una alta densità di strutture e della variabilità della topografia, si generano sovrapposizioni di risposte dei bersagli all'interno della stessa cella di risoluzione. Questo lavoro presenta i risultati ottenuti utilizzando una tecnica di ricostruzione tomografica basata sulla Decomposizione a Valori Singolari. Rispetto alle tecniche classiche interferometriche che misurano solo l'elevazione elevazione del target dominante, la tecnica tomografica consente di ottenere una ricostruzione 3D e quindi di analizzare la distribuzione dello scattering in quota. I risultati prestati sono relativi ad acquisizioni dei satelliti ERS-1/2 sull'area urbana di Napoli.
Parole chiave*: Focalizzazione SAR 3D, tomografia SAR*

Introduction

In modern technology, the availability of active sensors has generated interest in the development of innovative processing techniques able to enhance the capabilities and/or overcome the physical limits of the imaging device. This happens for instance with 3D ultrasound or Computer-aided Tomography (CAT), where the technology offers new options in imaging modes, such as: simultaneous rotation and translation of the three perpendicular planes displayed, surface rendering, or transparent modes.

As far as earth observation is concerned, unique potentialities are associated to active microwave remote sensing imaging and particularly to Synthetic Aperture Radars, where the transmitted radiation can be controlled in amplitude and phase.

One of the most celebrated applications of active microwave imaging is SAR Interferometry (Bamler and Hartl 1998). By using two or more images acquired from two slightly different view angles, this technique allows generating the Digital Elevation Model (DEM) of the scene under investigation. Accurate DEMs are obtained, even with satellite systems orbiting at hundreds of kilometres from the surface, when the scattering mechanism is simple (dominant target, distributed scattering on surface cells, etc.). On the other hand, whenever the radiation penetrates under the ground interface (a situation that rarely occurs with existing satellite sensors operating at relatively high frequencies) or the topography is particularly steep in such a way that it generates critical projection of the scatterers in the slant imaging geometry (layover), or there is an high spatial density of strong scatterers, the received signal may contain the superposition of multiple scattering responses in a single image pixel. The last two conditions are frequent when data are acquired over urban areas: indeed, due to the high irregularity of the surface profile, the scattering mechanism may involve different elementary linear and non linear contributions [Franceschetti et al. 2002] such as those associated to the ground and to the walls, or those arising from the interaction between ground and wall.

As a consequence, beside an increase of difficulties in interpreting the scene, DEM derivation or target movements monitoring (an option offered by differential SAR interferometry) could be impaired.

To overcome this limitation recently a new technique has been proposed: SAR tomography. Parallel to CAT Tomography, SAR Tomography is based on a fundamental principle: the object is imaged from different angles (views) to collect 3D samples and then the data stack is processed to convert the collected projections into a focused 3D image of the illuminated volume.

SAR tomography differs from the X-ray CAT in some points that generate processing problems: first of all samples are generally highly non-uniformly distributed; moreover they cannot be collected simultaneously but rather with repeated passes separated in time (typically at monthly rate for existing satellite systems). This fact causes the presence of phase miscalibration terms associated to atmospheric variations that needs to be properly faced in a pre-processing step before the 3D focusing step.

For this reason, only a few contributions in the literature address the application of SAR tomography to real data. First experiments with real data were carried out in laboratory [Pasquali et al., 1995] with ideal experimental conditions or by using airborne systems [Roessing and Ender 1998; Reigber and Moreira 2000; Lombardini and Reigber 2003], whereas the application of tomography to spaceborne systems is limited [Homer et al. 2002; She et al., 2002]. Notwithstanding, developments for spaceborne systems would couple the potentials of tomography with the synoptic view of orbiting sensors, and could encourage future 4D (space-time) SAR imaging thus allowing separating different targets at different velocities in the same resolution cell. A different, approach tuned to the separation of scatterers pairs to extend the Permanent Scatterers technique has been proposed in Ferretti et al 2005 and tested on real ERS data.

In this work we present the results of a tomographic study, started in 2003 [Fornaro et al., 2005] and based on the exploitation of ERS data for long-term tomography with satellite systems. In particular :

- we extend the experiment carried out in [Fornaro et al. 2005] to a higher number of passes
- we discuss the advances in the compensation procedure necessary at the pre-processing step
- we perform a first attempt of validation of the results by comparing it in terms of scatterers location to an orthophoto image.

Acquisition model and inversion

Let us refer to Figure 1 where we show the imaging geometry: let N be the number of images acquired with different spatial baselines with respect to a reference master image, over the investigated scene: x is the azimuth, r is the range, s (orthogonal to the azimuth and range plane) is the elevation or normal to the slant range direction (n.s.r.) and z is the height. Let us pick the signal g_n in a fixed pixel in the generic image, after an accurate image registration process aimed at aligning the ground cell in the same position in the different images.

Let $\gamma(s)$ be the function that models the scene complex scattering properties for the area at hand as a function of the elevation s. It is easily shown that [Fornaro et al., 2005]:

$$g_n = \int_{-a}^{a} \gamma(s) \exp\left[j2\pi\zeta_n s\right] ds \qquad [1]$$

where 2a is the extension in the elevation direction of the imaged scene, and $\zeta_n = 2b_{\perp n}/(\lambda r)$, with $b_{\perp n}$ the orthogonal baseline components of the passes with respect to the master track, λ the operating wavelength. Equation [1] illustrates the fundamental principle of the 3D imaging, and states that the measured data represent samples of the spectrum of the unknown scattering distribution in the elevation direction; in practical multiple-view (multibaseline) applications these spectral samples are not equi-spaced. Thus, we easily recognize that the problem of reconstructing the unknown function $\gamma(s)$ consists of inverting the "irregular" Fourier transform in Eq. [1]. In a dual framework, one can consider that the wavefront impinging on the calibrated tracks from a point source component produces a phase history along the baselines, thus a spatial frequency, which is proportional to the source elevation. As such $\gamma(s)$ is a complex amplitude spatial distribution or spatial spectrum [Gini et al. 2002] and the elevation image reconstruction can be cast as a spatial spectral estimation problem from irregularly sampled data.
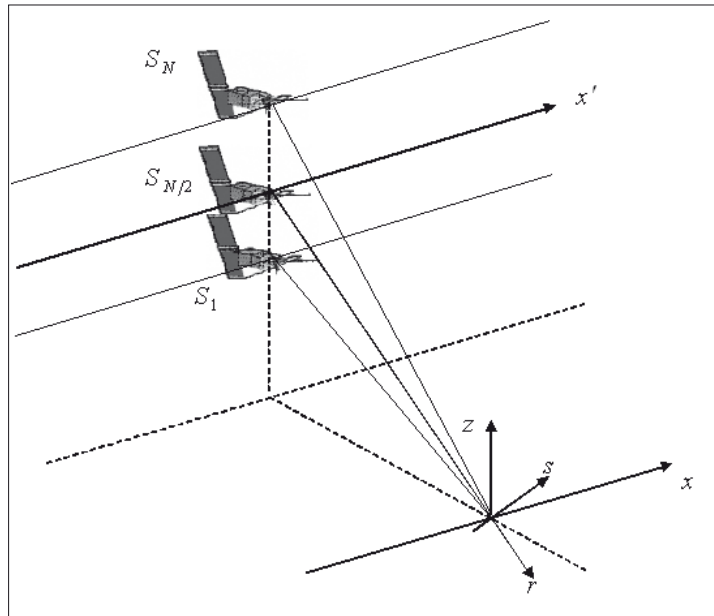

Figure 1 - Acquisition geometry.

The classical inversion technique to invert the linear relation in Eq. [1] is the BeamForming (BF) inversion [Pasquali et al. 1995; Reigber et al., 2000; She et al., 2002] where an irregular inverse Fourier Transform is applied.

In the dual framework, this corresponds to Fourier spatial spectral estimation, *i.e.* to the classical array processing technique of beam-steering, here applied in the elevation plane. Note that the final elevation resolution of BF cannot exceed the value:

$$\delta s = \frac{\lambda \ r}{2B} \qquad\qquad [2]$$

where B is the total orthogonal baseline span (Rayleigh diffraction limit). Also, from the sampling of the data in Eq. [1], an elevation unambiguous range interval can be defined; for the irregular sampling it can be approximated to:

$$\Delta s_{max} = \frac{\lambda \ r}{2b_{\perp}} \qquad\qquad [3]$$

where $b_{\perp}$ is the mean orthogonal baseline separation.

As an alternative to plain BF, the recent literature proposes a number of innovative techniques, both model based and adaptive, that allows moving from the data stack to the elevation scattering profile: they are either framed in the context of linear inverse problems [Fornaro et al., 2003; Fornaro et al., 2005] or of spatial spectral estimation [Webb et al., 1995; Roessing et al., 1998; Gini et al., 2002; Lombardini et al., 2003, Fornaro et al. 2004]. Such approaches allow one, at least in ideal conditions, to effectively overcome the limitations regarding the uneven baseline distribution and the limited number of images which cause poor resolution, high side-lobes and leakage in the elevation Point Spread Function (PSF). In the following we focus on Singular Value Decomposition (SVD) inversion which is a non model-based inversion technique widely used in the context of linear inverse problems [Bertero 1989].

The SVD method represents the linear operator in terms of a singular system and achieves a robust reconstruction by restricting the solution space, by considering only the singular functions corresponding to singular values that lay above the noise level. The SVD method also allows the inclusion of limited *a priori* information, the maximum expected dimension along the elevation direction of the scene to be reconstructed within the inversion algorithm.

Data calibration processing chain

Geometric, radiometric and phase calibration of the image stack are crucial issues, especially for data acquired over large temporal intervals, before application of the inversion procedure that implements the tomographic reconstruction. In Figure 2 it is shown the block diagram related to the complete procedure of amplitude and phase calibration. The first step of the compensation algorithm is a precise co-registration.

The importance of this procedure is due to the fact that the tomographic reconstruction requires the extraction of the amplitude and phase information from the same ground pixel which is located at different positions in the focused images. Accurate registration is a challenging issue in tomography due to the need to register images acquired with large temporal gaps and spatial baseline. In fact, these are characterized by high, spatially variable, geometrical distortion and decorrelation phenomena that may impair the precise location of tie-points used for registration.

In our case the technique is based on the use of orbital information and an external reference DEM [Serafino 2004; Fornaro et al., 2005] and refinements based on the use of the response
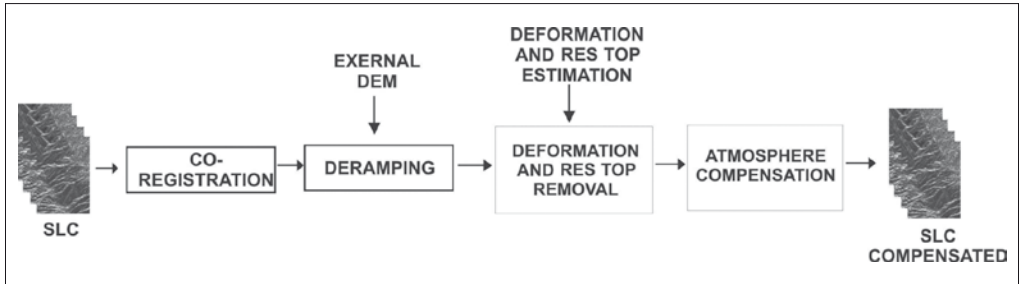
Figure 2 - Block diagram related to the complete compensation procedure of the focused images.

of Isolated Point Scatterers (IPS) that are characterized by a high level of signal to clutter (SCR) ratio and thus a high coherence even at large baselines.

The second step of image pre-processing implements a phase compensation of a phase distortion, mainly of quadratic nature, over the multibaseline array. This procedure, called de-ramping, is carried out by exploiting again the external DEM and the satellite orbits. As a consequence, the final elevation (height) distribution of the tomographic reconstruction is thus referred to the external DEM (local topography).

The following step is the compensation of the signal terms related to possible ground deformation and to errors caused by inaccuracies of the external DEM. Both the terms can be estimated from the stack (and separated from atmospheric contribution by exploiting the different spatio-temporal correlation properties [Berardino et al., 2002; Ferretti et al., 2000]. After the removal of these terms it is necessary to compensate the phase contribution due to the change of the atmospheric propagation during the acquisitions. This step is carried out in our case by working with image pairs (Stepwise Processing) according to a Minimum Spanning Tree (MST) strategy, as proposed in [Refice et al., 2003], in order reduce decorrelation effects due to large temporal and baseline separations and thus limit

Figure 3 - Spatial baseline vs. the temporal baseline (in years) and the tree obtained by using the MST algorithm related to the 63 SAR images.

their effect in the branch summation needed to estimate the atmospheric contribution at the different nodes. Figure 3 shows the 'tree' (nodes represent the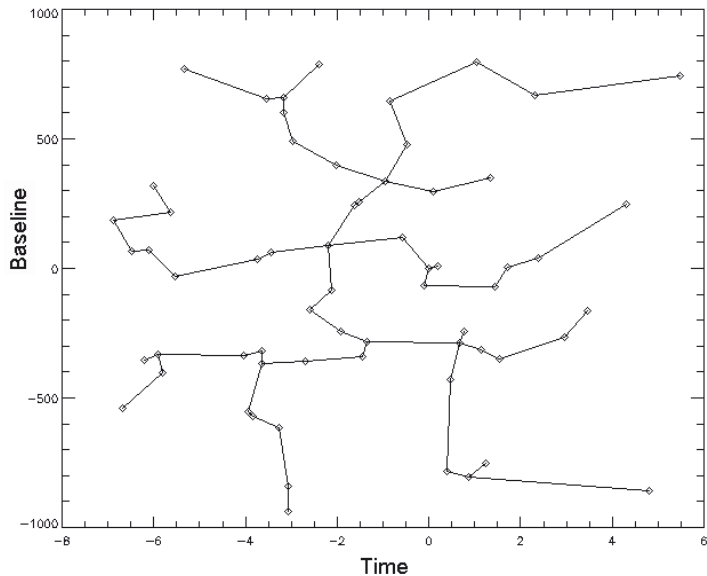 acquisition dates and branches their connections) obtained by considering the experimental data set consisting of 63 images of the ERS-1/2 satellite, track 36 frame 2781.

The structure of the tree may be modified by changing temporal and/or spatial constants to trade off between the temporal and the spatial decorrelation.

Figure 4 shows, together with the amplitude image (Fig. 4a), the images resulting from the three phase compensation steps. In particular we show the interferometric phase between two images prior and after deramping (Fig. 4b, 4c): the latter figure shows the deformation patter associated to the subsidence of the Campi Flegrei area, which is of volcanic nature. The interferogram (Fig. 4d) resulting from the next step (residual topography and deformation compensation) does no more exhibit any deformation pattern, but rather phase variations caused by atmospheric variations.

Also this contribution can be eliminated in the final interferogram (Fig. 4e). The next picture, Figure 5, aims to show that urban areas are particularly favourable for implementing long-term tomography experiments because of their high degree of coherence, even after many years. In particular, we show the coherence map of a tandem pair (Fig. 5 left) at 1 day time separation and after six years (Fig. 5 right): spatial decorrelation is low negligible due to the choice of small baseline pairs. In the left image we see that high coherence is retained almost everywhere, but for the sea area; in the right image, coherence is relatively high only on urbanized areas.
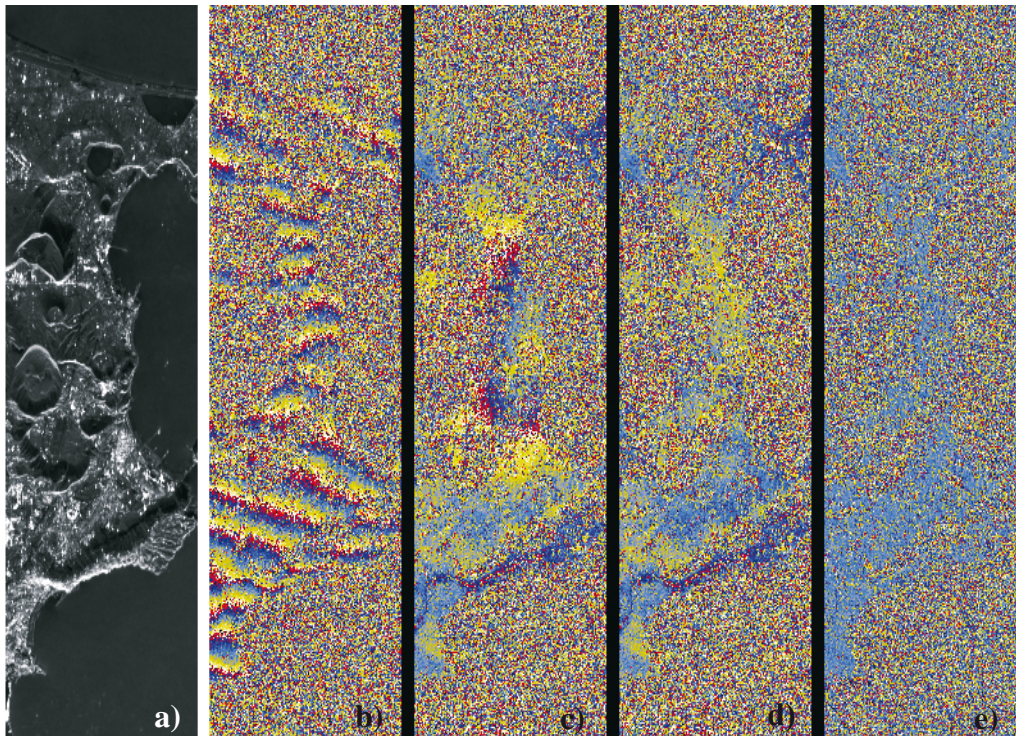
Figure 4 - Amplitude image (a) and interferograms associated to the compensation steps, before (b) and after (c) deramping, after residual topography and deformation compensation (d) and after atmospheric correction (e) for a selected image pair.

Figure 5 - Coherence at 1 day (left) and 6 years (right) temporal separation, colorscale is between 0 and 1.
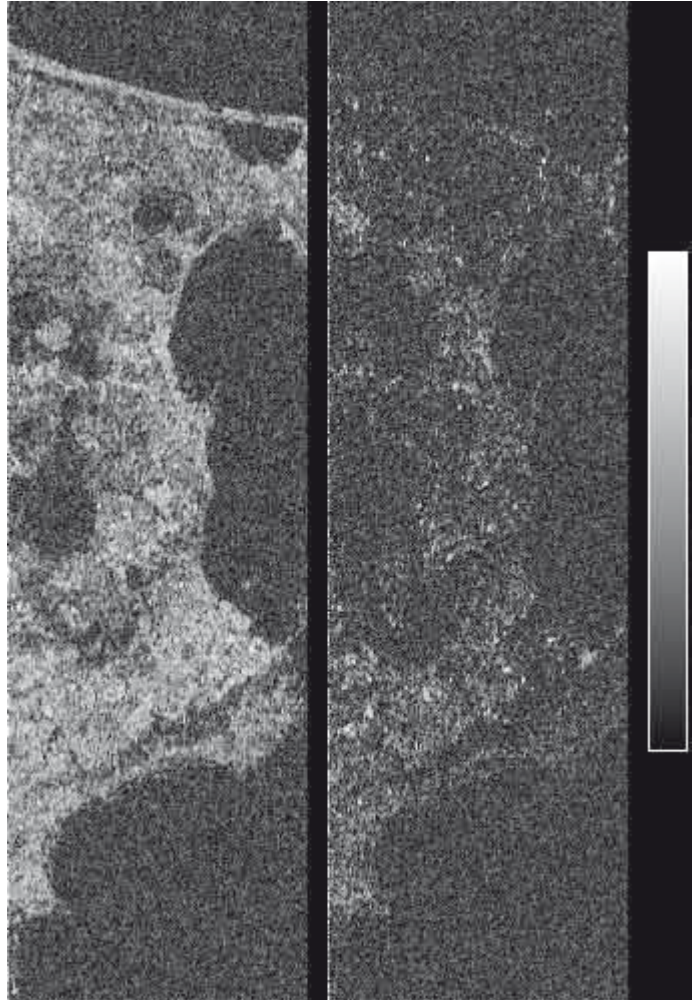
This suggests that, with future satellite constellations, for which daily acquisitions can be possible, SAR tomography could be reliably carried out even in non urbanized areas.

Experimental results

The tomographic technique has been applied to the 63 images of the ERS-1/2 satellite, whose baseline and time distribution is shown in Figure 3. The baseline span is about 1700 m, with a mean baseline separation of 28 m. The range to the scene centre is of about 847 Km; according to Eq. [2] and Eq. [3], the expected resolution is of about 14 m in elevation (5.5 m in height) and the unambiguous range of 870 m in elevation (340 m in height) .

Data have been calibrated according to the procedure explained in the previous section. Advantages related to the use of SVD instead of standard beamforming are described in Fornaro et al. [2003] and Fornaro et al. [2005].

The first experiment is aimed at verifying the capability to distinguish double scatterers: no a-priori information on the extension of the imaged scene is introduced. Figure 6 shows the data collected on the different antennas from a fixed azimuth and range pixel and the

reconstruction obtained by the SVD technique: two targets at 17 m height separation are clearly distinguishable from the reconstruction in the lower plot. From Eq. [1] it is easy to show that if two scatterers are present on the scene, a sinusoidal behaviour of the amplitude of g_n is achieved: this effect is also clearly visible in the amplitude and phase plots in Figure 6. Moreover, from Eq. [1] it results that, letting $b_{\perp p}$ to be the baseline period, that is the oscillation period of the signal along the multibaseline array, the relation between the target separation Δz and the baseline period $b_{\perp p}$ is given by:

$$\Delta z = \frac{\lambda r_0 \sin \vartheta}{b_{\perp p}} \overset{ERS}{=} \frac{19\,Km}{b_{\perp p}} m \qquad [4]$$

From Figure 6 we have $b_{\perp p} \approx 1,1$ km that is in perfect agreement with the observed target separation.

The second experiment refers to the reconstruction of extended scenes. In particular we focus our analysis on the San Paolo stadium. The data stack has been focused in 3D in all
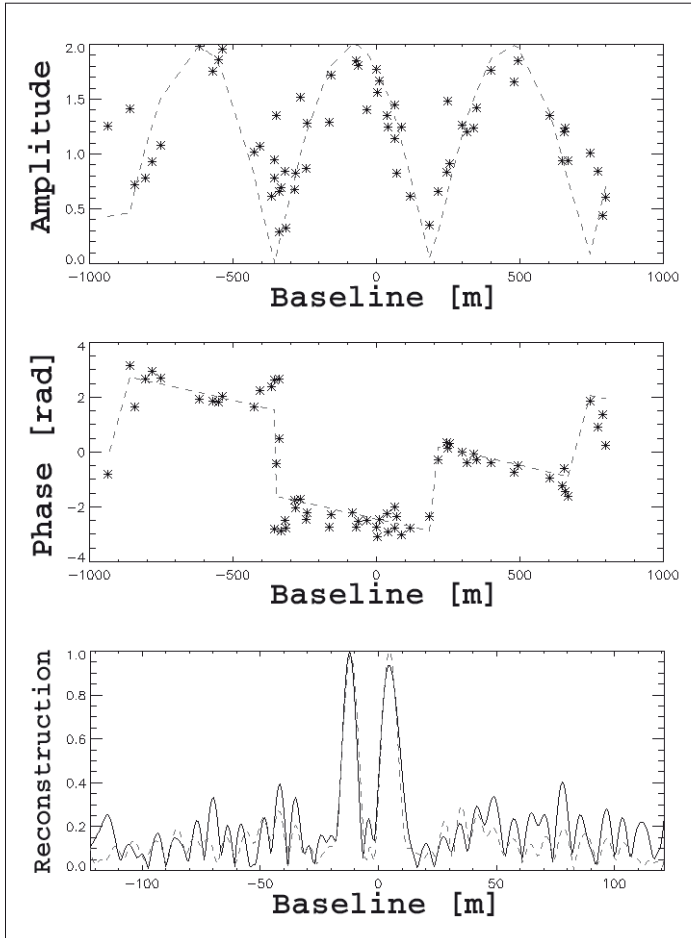
Figure 6 - Amplitude, phase and height profile for a double target.
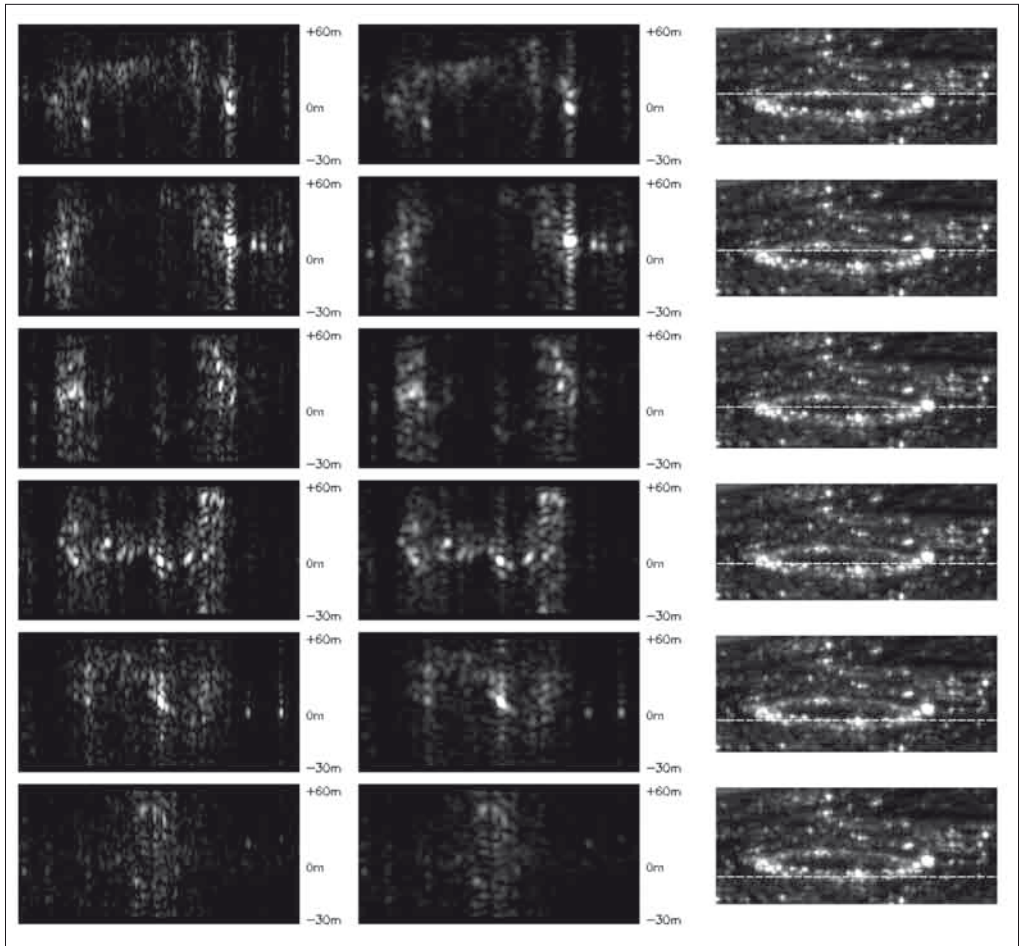
Figure 7 - Five different azimuth and height sections of the tomographic reconstructions over the San Paolo stadium obtained with the SVD at full resolution (left images) and with 5 azimuth looks (middle images), together with planar views of the stadium (right images) with the indication (dot line) of the section range position.

the pixels relative to this structure by using the SVD and restricting the domain of investigation by a factor of 3. The results, without and with a multilook of 5 in azimuth, in five different azimuth-height sections, are shown in Figure 7. From down to top, is clearly visible the metallic coverage structure of the stadium, appearing in the first and last section at image centre, whereas in the remaining sections the same structure is confined at left and right image borders.

To carry out a validation test of the imaging algorithm, we applied the SVD inversion to each spatial pixel in the area of Figure 4. Then we applied an algorithm aimed at locating all pixels that are characterized by a single scattering mechanism. To this end we correlated the elevation reconstruction in each azimuth and range pixel with the response of a single scatterer and applied a threshold of 0.58.

The threshold choice has been experimentally set as a good compromise between false detection and missing detection due to blurring caused by decorrelation (f.i., temporal) or
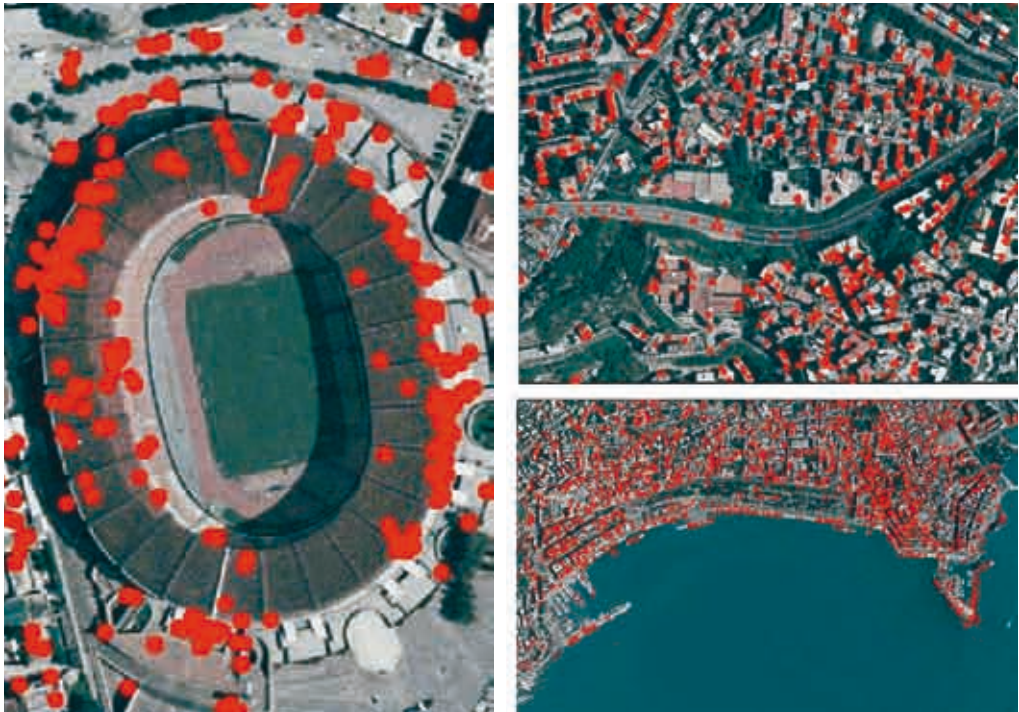
Figure 8 - Comparison between the location of single scatterers and a rectified orthophoto image for three different areas: the Stadium (left), the urban highway (top right) and the area of Castel dell'Ovo (down right).

residual atmospheric terms. For all pixels above the threshold we calculated the elevation and we applied a precise geo-location procedure. The results of the geolocation of these single scatterers (red dot) have been overlaid to a rectified orthophoto image.

Figure 8 shows the results for three different areas and demonstrate the capability of the algorithm to precisely locate the targets.

Conclusions

The development of an experiment started in 2003 and aimed at applying the tomographic technique to real data of the ERS-1/2 satellite has been discussed. The encouraging results show that, despite the critical condition where acquisitions are not simultaneous or nearly simultaneous but span an interval of 12 year, the technique is able to roughly reconstruct the shape of objects on the ground in complex scenarios such as urban areas.

Aknowledgements

References

Bamler R., Hartl P. (1998) - *Synthetic aperture radar interferometry.* Inverse Problems, 14: R1-R54.

Berardino P., Fornaro G., Lanari R., Sansosti E (2002) - *A new Algorithm for Surface Deformation Monitoring based on Small Baseline Differential SAR Interferograms.* IEEE Trans. Geosci. Remote Sens., 40: 2375-2383.

Bertero M. (1989) - *Linear inverse and ill-posed problems.* Advances in Electronics and Electron Physics, Academic Press.

Ferretti A., Prati C., Rocca F. (2000) - *Nonlinear subsidence rate estimation using the permanent scatterers in differential SAR interferometry.* IEEE Trans. Geosci. Remote Sens., 38 (5): 2202-2212.

Ferretti A., Bianchi M., Prati C., Rocca F. (2005) - *Higher-Order Permanent Scatterers Analysis.* EURAISP Journal on Applied Signal Processing, 20: 3231-3242.

Fornaro G., Serafino F., Soldovieri F. (2003) - *Three Dimensional Focusing With Multipass SAR Data.* IEEE Trans. Geosci. Remote Sens., 41: 507-517.

Fornaro G., Lombardini F., Serafino F. (2004) - *First Experiments of Adaptive 3D SAR Tomography with Repeat-pass Spaceborne Data.* Proc. EUSAR 2004, Ulm, Germany.

Fornaro G., Serafino F., Lombardini F. (2005) - *3D Multipass SAR Focusing: Experiments with Long-Term Spaceborne Data.* IEEE Trans. Geosci. Remote Sens., 43: 702-712.

Fornaro G., Manunta M., Serafino F., Berardino P., Sansosti E. (2005) - *Advances in Multipass SAR image registration.* Proceedings of IGARSS, Seul, Corea.

Franceschetti G., Iodice A., Riccio D. (2002) - *A Canonical Problem in Electromagnetic Backscattering From Buildings.* IEEE Trans. Geosci. Remote Sens., 40(8): 1787-1801.

Gini F., Lombardini F., Montanari M. (2002) - *Layover Solution in Multibaseline SAR Interferometry.* IEEE Trans. Aerosp. Electron. Syst., 38: 1344-1356.

Homer J., Longstaff I.D., She Z., Gray D. (2002) - *High resolution 3-D imaging via multipass SAR.* IEE Proc. Pt.-F, 149(1): 45-50.

Lombardini F., Reigber A. (2003) - *Adaptive spectral estimation for multibaseline SAR tomography with airborne L-band data.* Proc. of IEEE Int. Geosci. Remote Sens. Symposium, 3: 2014-2016.

Pasquali P., Prati, Rocca F., Seymour M. (1995) - *A 3D SAR experiment with EMSL data.* Proceedigns of IGARSS05, Firenze, 784-786.

Refice A., Bovenga F., Nutricato R. (2003) - *Stepwise approach to InSAR processing of multitemporal datasets.* Proceedings of FRINGE'03, ESA-ESRIN, Frascati, Italy.

Reigber A., Moreira A. (2000) - *First Demonstration of Airborne SAR Tomography Using Multibaseline L-Band Data.* IEEE Trans. Geosci. Remote Sens., 38: 2142-2152.

Roessing L., Ender J.H.G. (1998) - *Advanced SAR Interferometry Techniques with AER-II.* Intern. Radar Symposium DGON, IRS, Munich, 1261-1269.

Serafino F. (2004) - *Innovative processing of multipass SAR data.* Ph.D. Thesis, University of Napoli.

She Z., Gray D. A., Bogner R. E., Homer J., Longstaff I.D. (2002) - *Three-dimensional spaceborne synthetic aperture radar (SAR) imaging with multipass processing.* Int. J. Remote Sensing, 23: 4357-4382.

Webb J.L.H., Munson Jr. D.C. (1995) - *Radar imaging of three-dimensional surfaces using limited data.* Proc. of IEEE Int. Conference on Image Processing, Washington 136-139.

A novel MRF model for the detection of urban areas in optical high spatial resolution images

Federico Causa, Gabriele Moser and Sebastiano B. Serpico

Dipartimento di Ingegneria Biofisica ed Elettronica (DIBE), Università di Genova, via Opera Pia 11a - 16145 Genova. E-mail: vulcano@dibe.unige.it

Abstract

In this paper, a novel Markov random field (MRF) model is proposed for the classification of high spatial resolution data. The key idea is that each thematic class can be described by a set of clusters, which represent spectral subclasses related to material responses. Accordingly, the proposed MRF model describes the contextual information by using the relationship between the (user-defined) thematic classes and the clusters extracted by a clustering procedure. This approach permits one to avoid penalizing configurations of cluster labels of neighboring pixels corresponding to the same thematic label. The proposed model has been validated on a real data set acquired by an IKONOS sensor.

Keywords: Markov random field, high spatial resolution images, urban area detection, hybrid supervised/unsupervised classification, hierarchical clustering

Riassunto

In questo articolo, si propone un modello "Markov random field" (MRF) innovativo per la classificazione di dati ad elevata risoluzione spaziale. L'idea chiave è basata sulla descrizione delle classi tematiche (definite dall'utente) come insiemi di classi naturali ("cluster") che rappresentano sottoclassi legate alle risposte di differenti materiali. Il modello MRF proposto descrive l'informazione contestuale sfruttando la corrispondenza tra classi tematiche e "cluster", estraendo questi ultimi mediante una procedura di "clustering". Tale approccio consente di non introdurre penalizzazioni quando le etichette di "cluster" dei pixel vicini sono associate ad una stessa etichetta tematica. L'approccio proposto è validato su un insieme di dati reali acquisiti da un sensore IKONOS.

Parole chiave*: Campi aleatori markoviani, immagini ad alta risoluzione spaziale, identificazione di aree urbane, classificazione ibrida supervisionata/non supervisionata, clustering gerarchico.*

Introduction

In the past three decades, the spatial resolution of satellite imagery has been substantially improved. Recently, 1-5 m resolution imagery (e.g., IKONOS, Quickbird, SPOT 5, Orbview) has become available. Very High spatial Resolution (HR) data provide plenty of detailed information about the ground on a regular basis for applications such as urban planning. However, the complex nature of the urban environment, due to the presence of various land cover types, makes the detection of the "urban" thematic class a difficult task. The materials that can be found in the urban environment may include concrete, asphalt, metal, plastic, glass, water, grass, trees, shrubs, and bare soil, to list just a few. In general, these materials are arranged into very complex configurations in an image, such as housing developments, industrial facilities, etc. Hence, HR data may allow more details to be obtained and the urban

areas to be better characterized, but, on the other hand, the presence of such different material responses give rise to additional problems in terms of information extraction. Also in the case of moderate and coarse spatial resolution data, urban areas are often much more heterogeneous than natural landscapes, so the conventional automatic per-pixel classification procedures do not always provide a good discrimination of the "urban" class. This issue becomes even much more critical when dealing with HR data, due to the high within-class spectral variance of the classes. A finer resolution yields a decrease in the number of mixed pixels thus increasing the classification accuracy by possibly reducing the overlapping among different classes in the feature space. On the other hand, the finer the resolution, the larger the number of subclasses based on material responses; this implies a high within-class spectral variance of some thematic classes and a stronger multi-modality of the class-conditional statistics, which affect the class detection accuracy. In particular, pixel-wise classification methods, which detect object classes only according to the spectral information about the individual pixels, while neglecting the spatial relationships among distinct pixels, may be expected to be poorly effective when applied to HR data. From this viewpoint, the use of spatial information, such as contextual or texture information, can be expected to play a basic role in HR data classification, especially in the case of urban areas. Several works have demonstrated the contribution of texture information to discriminating different land cover types, showing that this information can lead to meaningful improvements in the classification accuracy of urban areas. During the last decade, studies on HR data related to urban areas have proposed the use of the grey-level co-occurrence matrix for the extraction of the second-order statistics of grey levels [Hsu, 1978] [Gong et al., 1990], as well as morphological profiles [Benediktsson et al., 2002], neural networks [Tatem et al., 2001] or segmentation and object-based classification approaches [Pesaresi et al., 2001; Kressler et al., 2002].

Another tool for exploiting contextual information is represented by Markov random fields (MRFs). MRFs play an important role in image analysis and modeling, thanks to their ability to integrate the use of contextual information associated with image data into the analysis process [Geman et al., 1984; Dubes et al., 1989]. MRFs are a wide class of probabilistic models for the statistical interactions among the grey levels and/or the class labels of the pixels in an image, and have been applied by the remote-sensing community in many applications such as, for instance, classification of multi-sensor [Solberg et al., 1996], multi-temporal [Melgani et al., 2003], multi-resolution [Storvik et al., 2005] and hyper-spectral data [Jackson et al., 2002], segmentation [Smits et al., 1997], change detection [Bruzzone et al., 2000], texture analysis [Dubes et al., 1989], and denoising [Datcu et al., 1998]. In particular, the most widespread MRF models for image classification, such as the Ising or the Potts models [Dubes et al., 1989], have been proved to be often effective in the moderate and coarse spatial resolution contexts, also because the thematic classes are generally homogeneous, which makes the above-mentioned class heterogeneity problem less critical. On the contrary, in the HR context, the classical MRF models are likely to be less effective, since they deal with all land covers as single classes, *i.e.*, without taking into account that such classes are actually sets of subclasses, each of them being related to a specific material spectral response. As discussed above, this problem is especially important for the "urban" class.

In the present paper, a novel MRF model is proposed and employed for hybrid supervised/unsupervised classification of HR data; such a model aims at overcoming the afore-mentioned drawbacks. The key idea of the method is to use jointly information both about user-defined classes (characterized by training data) and about material subclasses (identified by a clustering approach) by integrating all such information through a case-specific hybrid supervised/unsupervised MRF model. Hence, the method exploits explicitly the relationships between user-defined classes and their spectral subclasses for contextual information modelling and classification purposes.

The paper is organized as follows. First, a general description of the proposed classification architecture is provided. Then, the proposed MRF model is detailed and compared with the conventional MRF Potts one. Classification results, obtained on a multi-spectral data set acquired by a 3-band IKONOS sensor, are reported. Finally, conclusions about the proposed classification methodology are drawn.

Architecture of the proposed classification scheme

The proposed MRF model relies on the idea of jointly using the information about the thematic classes and the spectral subclasses for the analysis of the spatial context. Therefore, in order to apply the proposed MRF model, the set of spectral subclasses has to be identified. This task has been accomplished by applying a clustering algorithm, thus identifying each subclass as one of the resulting clusters.

The proposed MRF model exploits both cluster and class information in order to avoid penalizing the transitions between cluster labels corresponding to the same thematic class label. This allows one both to keep the possibility (typical of MRF models) of integrating the contextual information into the classification process and to exploit the information about spectral material classes, conveyed by the clustering result, in order not to penalize the discrimination among user-defined classes. In particular, the hierarchical clustering method developed by Wong and Posner (W&P) [Wong et al., 1993] is adopted to extract the spectral subclasses, since this method has been proved to be an effective classification tool for HR data [De Martino et al., 2004].

In the next section, the proposed MRF model is described in detail. The architecture of the resulting classification scheme is shown in Figure 1 and consists of the following processing phases:
- "Hierarchical clustering" phase: the clustering information is extracted by the hierarchical clustering method proposed in [Wong et al., 1993]. Such a method generates a complete hierarchy of clustering maps to different degrees of spatial detail.
- "Clustering map selection" phase: given the hierarchical clustering result, the hybrid approach proposed in [Serpico et al., 2003] is used to select an optimal clustering map from the hierarchy, whose clusters best represent the subclasses of the user-defined classes. Such an approach integrates the clustering information with the training information (represented by a training map) to assign a thematic class label to each cluster according to the "maximum *a-posteriori*" (MAP) criterion by maximizing a criterion function that estimates the probability of correct classification of the related hybrid classification map. Therefore, the clustering map is selected in such a way as to maximize the related criterion function value.
- "MRF parameter estimation" phase: the estimation of the internal parameters of the model is carried out by the automatic algorithm presented in [Moser et al., 2005], which formulated the MRF parameter optimization problem as the solution of a set of linear inequalities, addressed by using the Ho-Kashyap method [Duda et al., 2001]. The optimal MRF parameters are obtained by running the Ho-Kashyap procedure up to convergence.
- "Energy minimization" phase: the proposed classification method adopts the Iterated Conditional Mode (ICM) approach [Dubes et al., 1989], which is initialized with the above-mentioned non-contextual hybrid classification result. It iteratively modifies the clustering map according to the cluster-labelling information derived from the "clustering map selection" phase, and converges to a local maximum point of the global posterior probability distribution [Dubes et al., 1989]. This phase generates a contextual clustering map. Specifically, ICM is chosen thanks to its well-known capability to obtain
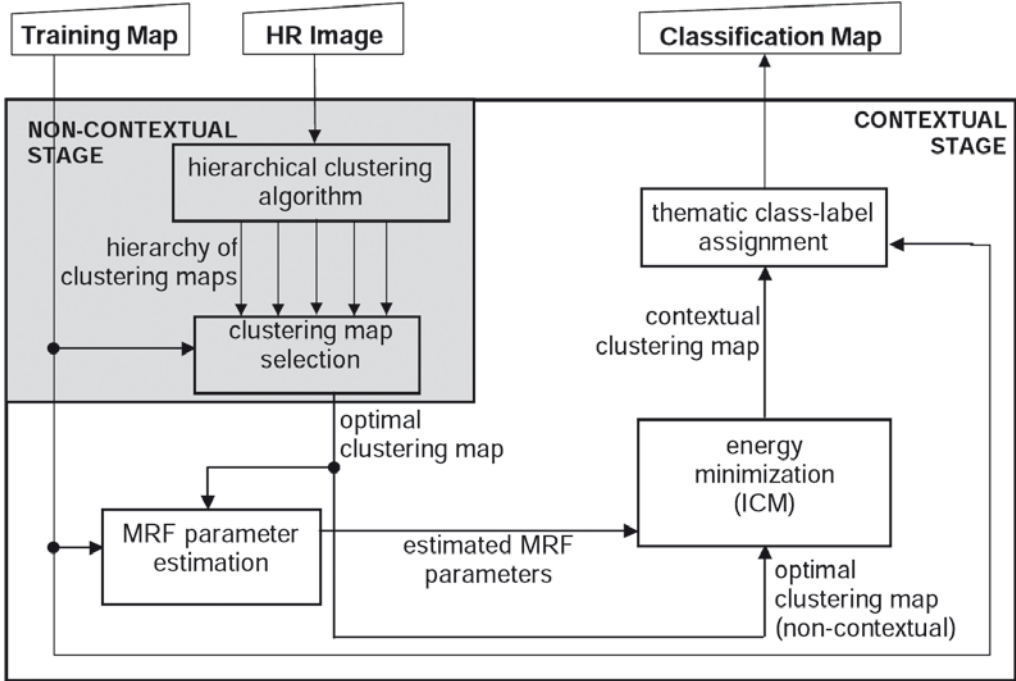
Figure 1 - Architecture of the proposed classification method.

accurate results without taking unacceptable computation times (slightly more accurate classification strategies, like simulated annealing [Geman et al., 1984], could be used, but much longer execution times would be required).

- "Thematic class label assignment" phase: the hybrid classification result is updated according to the contextual clustering map provided by the "energy minimization" phase. Specifically, the MAP criterion is applied again to assign a thematic class label to each cluster in this map (as in the "clustering map selection" phase), thus resulting in a hybrid contextual classification map.

MRF models
Problem definition

Let $I = \{y_1, y_2, \ldots, y_N\}$ be a given n-band remote sensing image (observation field), modeled as a set of N identically distributed n-variate random vectors. We assume M thematic classes, defined by the training map, to be available, and we collect them to the set $\Theta = \{\omega_1, \omega_2, \ldots, \omega_M\}$. We stack all the feature vectors of the N image pixels in a single $(N\,n)$-dimensional vector $Y = (y_1, y_2, \ldots, y_N)$ and all the pixel class labels in a discrete random vector $X = (x_1, x_2, \ldots, x_N)$.

The MAP decision rule assigns to the image data Y the label vector X^* that maximizes the joint posterior probability $P_{X|Y}(X|Y)$, i.e.:

$$X^* = \arg\max_{X \in \Theta^N} P_{X|Y}(X \mid Y) = \arg\max_{X \in \Theta^N}\left[p_{Y|X}(Y \mid X) \cdot P_X(X) \right] \qquad [1]$$

where $p_{Y|X}$ is the conditional probability density function (pdf) of the image data, given the

label configuration, and P_X is the probability mass function (pmf) of the label configuration itself.

Assuming for the observation model $p_{Y|X}$ that the feature vectors of distinct pixels (observations) are conditionally independent and identically distributed, *i.e.*:

$$p_{Y|X}(Y \mid X) = \prod_{i=1}^{N} p_{y|x}(y_i \mid x_i) \qquad [2]$$

and postulating the pmf P_X, of the class label vector, to be an MRF [Dubes et al., 1989], the Hammersley-Clifford theorem allows expressing the global posterior probability [1] in terms of an energy function $U(X|Y)$ that can be expressed by a set of locally defined energy contributions:

$$P_{X|Y}(X \mid Y) = \frac{e^{-U(X|Y)}}{Z(Y)} \qquad [3]$$

where $Z(Y)$ (the so-called "partition function") is a normalizing constant. Therefore, the MAP classification rule [1] can be regarded as the minimization of the global energy function $U(X|Y)$. Specifically, a local maximum of $U(X|Y)$ can be reached by the ICM algorithm, which iteratively minimizes a "local energy function," given for each k-th pixel ($k = 1, 2, …, N$), by:

$$U_\lambda(x_k \mid y_k, C_k) = \lambda_s \cdot \varepsilon_s(x_k \mid y_k) + \lambda_c \cdot \varepsilon_c(x_k \mid C_k) \qquad [4]$$

The local energy function is expressed as a linear combination of two distinct local energy contributions, *i.e.*, a spectral contribution ε_s related to the feature vector of each k-th pixel ($k = 1, 2, …, N$) and a spatial contribution ε_c related to the context C_k of the k-th pixel (*i.e.*, the set of class labels of the neighbors of the k-th pixel). The model presents two parameters, λ_s and λ_c, which represent the weights assigned to each energy contribution in the linear combination.

The Potts model
A typical model, often employed for the classification of optical data [Jackson et al., 2002] [Bruzzone et al., 2000], presents the following energy contributions:
  a) Spectral energy contribution: a parametric Gaussian model is assumed for the ω_i-conditional pdf; it yields [Dubes et al., 1989]:

$$\varepsilon_s(\omega_i \mid y_k) = (y_k - \hat{m}_{\omega_i})^T \hat{\Sigma}_{\omega_i}^{-1}(y_k - \hat{m}_{\omega_i}) + \ln(\det\hat{\Sigma}_{\omega_i}) \qquad [5]$$

where $\hat{m}_{\omega_i}$ and $\hat{\Sigma}_{\omega_i}$ are the sample-mean and the sample-covariance estimates of the mean and the covariance matrix, computed according to the training samples of ω_i ($i = 1, 2, …, M$), respectively, and the superscript "T" denotes the matrix transpose operation.
  b) Spatial energy contribution: a penalty term related to spatial class transitions is introduced, *i.e.*:

$$\varepsilon_c(\omega_i \mid C_k) = -\sum_{\omega_j \in C_k} \delta(\omega_i, \omega_j) \qquad [6]$$

where C_k is a second-order neighborhood system, *i.e.*, it includes the thematic class labels of the eight pixels surrounding the k-th pixel ($k = 1, 2, …, N$), and $\delta(\cdot, \cdot)$ is the Kronecker delta function (*i.e.*, $\delta(a, b) = 1$ for $a = b$ and $\delta(a, b) = 0$ for $a \neq b$). If such a model represents the contextual information (the so-called Potts model), a penalty

depends only on the presence or absence of a spatial class transition in order to enforce the spatial regularity of the classification map.

The proposed MRF model

The proposed model relies on the idea of integrating clustering information to describe each user-defined class in terms of a set of spectral (material) subclasses [Jia et al., 2001]: this aims at taking into account the complexity of the information classes in HR data. This model aims at avoiding the penalties related to the transitions between cluster labels belonging to the same thematic class.

Specifically, we assume P clusters to have been obtained by the procedure proposed in [Serpico et al., 2003], and we denote by $\Omega = \{\sigma_1, \sigma_2, \ldots, \sigma_P\}$ the resulting set of extracted clusters and by $s_k \in \Omega$ the cluster label of the k-th image pixel ($k = 1, 2, \ldots, N$). Also in this case, all the feature vectors of the N image pixels are collected in a single ($N\,n$)-dimensional vector $Y = (y_1, y_2, \ldots, y_N)$, but now we stack all the pixel cluster labels, rather than the class labels, in a discrete random vector $S = (s_1, s_2, \ldots, s_N)$. According to such a choice, the local energy function is still modeled as a linear combination of a spectral and a spatial contribution, but it depends on the cluster labels:

$$U_\lambda(s_k \mid y_k, C_k) = \lambda_s \cdot \varepsilon_s(s_k \mid y_k) + \lambda_c \cdot \varepsilon_c(s_k \mid C_k) \qquad [7]$$

Specifically, the energy contributions of the proposed model are defined as follows:

   a) Spectral energy contribution: this contribution is similar to the one related to the above-mentioned model [4], *i.e.*:

$$\varepsilon_s(\sigma_i \mid y_k) = (y_k - \hat{m}_{\sigma_i})^T \hat{\Sigma}_{\sigma_i}^{-1}(y_k - \hat{m}_{\sigma_i}) + \ln(\det \hat{\Sigma}_{\sigma_i}) \qquad [8]$$

   where $\hat{m}_{\sigma_i}$ and $\hat{\Sigma}_{\sigma_i}$ are the sample-mean and the sample-covariance estimates of the mean value and of the covariance matrix, respectively; however, note that such estimates are computed by using the observations related to the cluster σ_i ($i = 1, 2, \ldots, P$) and not to a user-defined class. Since each class is modeled as a set of clusters, this yields a Gaussian mixture model for the distribution of each class ω_i ($i = 1, 2, \ldots, M$), *i.e.*, a more general model than the single component Gaussian model used for the classical approach.

   b) Spatial energy contribution: as previously mentioned, the spatial energy contribution exploits a relationship between the thematic classes (defined by the training information) and the set of extracted clusters. The proposed MRF model exploits this hybrid supervised/unsupervised information by using both the cluster and the thematic class labels in order to avoid penalizing the transitions between cluster labels corresponding to the same thematic class label.

Formally, a matrix Z is introduced to represent the relationship between clusters and classes. The (i, j)-th entry of Z, $z(i, j)$, is equal to 1 if the cluster σ_i belongs to the thematic class ω_j, and is equal to 0 if σ_i does not belong to ω_j ($i = 1, 2, \ldots, P; j = 1, 2, \ldots, M$). As previously mentioned, this cluster-class assignment is obtained by the method proposed in [Serpico et al., 2003]. Denoting by D_j and B_i the sets of pixels assigned to ω_j in the training map and to σ_i in the optimal clustering map, respectively, the cluster-labelling rule introduced into [Serpico et al., 2003] gives:

$$z(i, j) = \begin{cases} 1 & \text{if } j = \arg \max_{k=1, 2, \ldots, M} |B_i \cap D_k| \\ 0 & \text{otherwise} \end{cases} \qquad [9]$$

i.e., the cluster-class assignment is based on the spatial overlappings between the clusters and the training areas. For each cluster σ_i, denoting by $t = t(i)$ the index of the only thematic class label such that $z(i, t) = 1$ ($i = 1, 2, \ldots, M$), the spatial energy contribution of the proposed MRF model is defined as follows:

$$\varepsilon_c(\sigma_i \mid C_k) = \sum_{\substack{j=1 \\ j \neq t(i)}}^{M} \sum_{\sigma_r \in C_k} z(r, j)\left[1 - \delta(\sigma_i, \sigma_r)\right] \qquad [10]$$

Like the spatial energy contribution of the classical model, this term is a contribution to the energy function to be minimized. If all the neighbors of the *k*-th pixel belong to clusters assigned to the same thematic class, then ε_c is equal to 0. On the contrary, if all the neighbors of the *k*-th pixel belong to clusters assigned to different thematic classes, ε_c is equal to 8. In such a model, a penalty is introduced for each transition inside the neighborhood between clusters corresponding to different information classes. On the contrary, no penalty is introduced for a couple of different neighboring cluster labels, both assigned to the same thematic class.

In this case, all the cluster transitions are equally weighted by the parameter λ_c, which is estimated together with λ_s by using the iterative method proposed in [Moser et al., 2005]. Hence, this modification to the model does not increase the number of MRF parameters, as compared with the classical approach.

Experimental results

The proposed hybrid MRF-based method for HR data (in the following denoted by HR-ICM) was tested on a real data set acquired over an urban area near Itaipu (Brazil/Paraguay border) by a 3-band IKONOS MS sensor with 4-m resolution. The validation phase was carried out by performing two different experiments, each related to a different set of thematic classes. Experiment 1 involved a (330x200) pixel-sized version of the data set, including five thematic classes, whereas Experiment 2 adopted a larger version of the data set (700x400) pixels, presenting a larger number of strongly overlapping classes. This set of two tests aims at assessing the behavior of the proposed method under different conditions concerning the complexity of the classification problem at hand. The HR image of the first set of classes (Fig. 2) represents a scene contained in the one used for Experiment 2.

In both experiments, the results of the proposed method were compared with those obtained by the standard MRF-ICM classifier based on the above-mentioned classical model (here denoted simply by Potts-ICM) and with those yielded by a standard non-contextual MAP classifier under the assumption of Gaussian class-conditional distributions (hereafter denoted simply by GMAP), often used to classify optical multi-spectral images. Note that Potts-ICM generates a contextual classification map only according to the thematic class information. The MRF parameters of both the Potts-ICM and HR-ICM classifiers were estimated by the Ho-Kashyap algorithm [Moser et al., 2005], initialized by setting unitary values for all the MRF parameters (*i.e.*, by assigning initially the same weight to all the energy contributions). For both MRF models, 50 ICM iterations were sufficient to reach convergence in all the experiments. In particular, Potts-ICM was initialized with the classification map obtained by GMAP. A quantitative evaluation and a comparison of the different methods were carried out by using confusion matrices.

Experiment 1

A preliminary visual analysis of the HR image considered in Experiment 1 (Fig. 2) pointed out that the scene presented a strongly heterogeneous urban area in the leftmost part of the
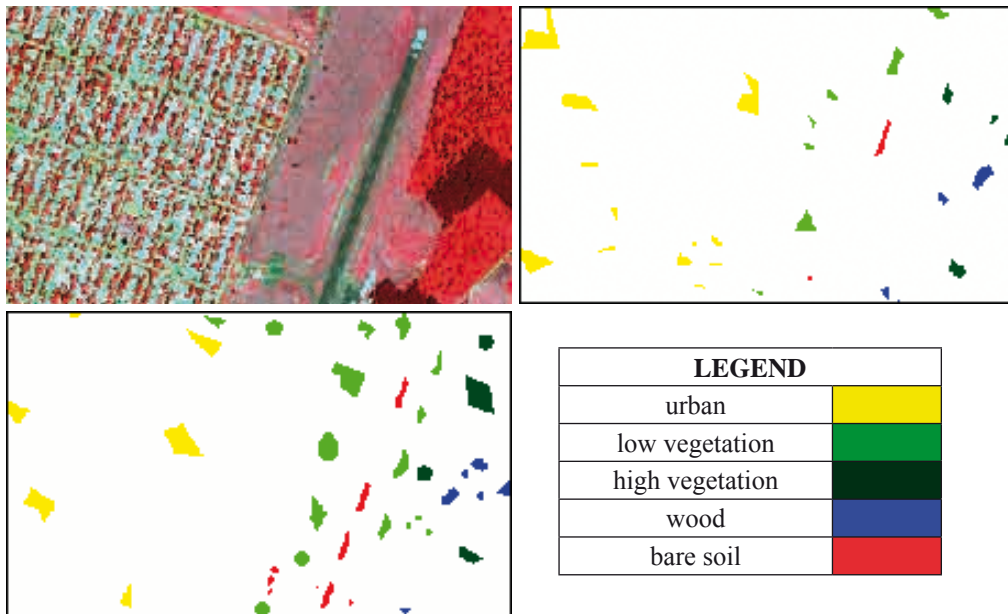
Figure 2 - Experiment 1: false-color HR image of an area near Itaipu, Brazil/Paraguay border (top left), training map (top right), test map (bottom left).

image (including buildings, streets, and small vegetation areas around the buildings), a low-vegetation region and a long bare-soil structure (maybe a runway) in the middle part of the image, and high-vegetation and wood areas in the rightmost part of the image. Accordingly, a ground-truth map was generated that presented five thematic classes (*i.e.*, "urban," "low vegetation," "high vegetation," "wood," and "bare soil"). Specifically, 3459 training pixels and 2007 test pixels, gathered into spatially disjoint sets, were available (Fig. 2). Note that the "urban" thematic label is referred to the whole urban area in order to assess the capability of the proposed method to identify this class, irrespective of its spatial heterogeneity, in the presence of the buildings, the street, and the vegetation subclasses (Fig. 2).

As regards HR-ICM, the optimal clustering map, identified by the "clustering map selection phase," was made up of 20 clusters. Specifically, 9 clusters were assigned to "urban," 5 clusters to "low vegetation," 2 clusters to "high vegetation," 2 clusters to "wood," and 2 clusters to "bare soil." As expected, the "urban" thematic class turned out to be the class with the largest number of spectral subclasses, which confirms the heterogeneity of this land-cover typology.

Table 1 gives the confusion matrices obtained by GMAP, Potts-ICM, and HR-ICM over the test set: GMAP already provided good classification performances, with accuracies above 83% for all the classes. The results confirm the effectiveness of using contextual information for the classification of HR data, since the classification accuracies reached by Potts-ICM and HR-ICM were significantly better than the ones given by GMAP. However, HR-ICM provided a better classification result than Potts-ICM, with a 3.7% increase in the overall accuracy, a 5.3% increase in the accuracy for "urban," and a 4.4% increase in the accuracy for "high vegetation."

These numerical results are confirmed by a qualitative visual analysis of the corresponding classification maps. As shown in Figure 3, the image areas corresponding to the same infor-

Table 1 - Experiment 1: confusion matrices for GMAP, Potts-ICM, and HR-ICM. Note that 17 test pixels of the class "urban" turned out not to be classified since they belonged to small clusters with empty spatial intersections with the training regions.

GMAP						
Test map	Classification map					Class accuracy (%)
	Urban	Low-veg	High-veg	Wood	Bare-soil	
Urban	943	89	47	22	29	83.451
Low-veg	12	379	0	0	0	96.930
High-veg	12	0	183	11	0	88.835
Wood	1	0	11	177	0	93.650
Bare-soil	1	0	0	0	90	98.901
					Overall accuracy (%)	88.291
Potts-ICM						
Test map	Classification map					Class accuracy (%)
	Urban	Low-veg	High-veg	Wood	Bare-soil	
Urban	1068	5	20	21	16	94.513
Low-veg	3	388	0	0	0	99.232
High-veg	4	0	197	5	0	95.631
Wood	0	0	2	187	0	98.941
Bare-soil	0	0	0	0	91	100
					Overall accuracy (%)	96.213
HR-ICM						
Test map	Classification map					Class accuracy (%)
	Urban	Low-veg	High-veg	Wood	Bare-soil	
Urban	1128	0	0	0	2	99.823
Low-veg	0	391	0	0	0	100
High-veg	0	0	206	0	0	100
Wood	0	0	0	189	0	100
Bare-soil	0	0	0	0	91	100
					Overall accuracy (%)	99.900

mation class were better detected in the classification map obtained by HR-ICM, whereas the maps generated by Potts-ICM and GMAP exhibit a noisier aspect, due to the fact that such classifiers do not take into account the presence (on the ground) of distinct material classes related to the same information class.

The classification map obtained by HR-ICM is less noisy, as compared with the classification maps of Potts-ICM and GMAP. In particular, note that the almost-100% classification accuracy given in Table 1 for HR-ICM refers to the classification of the test fields. As can be seen in Figure 3, some classification errors are still present also in the HR-ICM map, especially near the borders between distinct thematic classes. Actually, no test pixels are available in such border areas (which are also likely to contain mixed pixels). We note that the behavior of HR-ICM in such areas could be improved by introducing into the model

LEGEND	
urban	
low vegetation	
high vegetation	
wood	
bare soil	
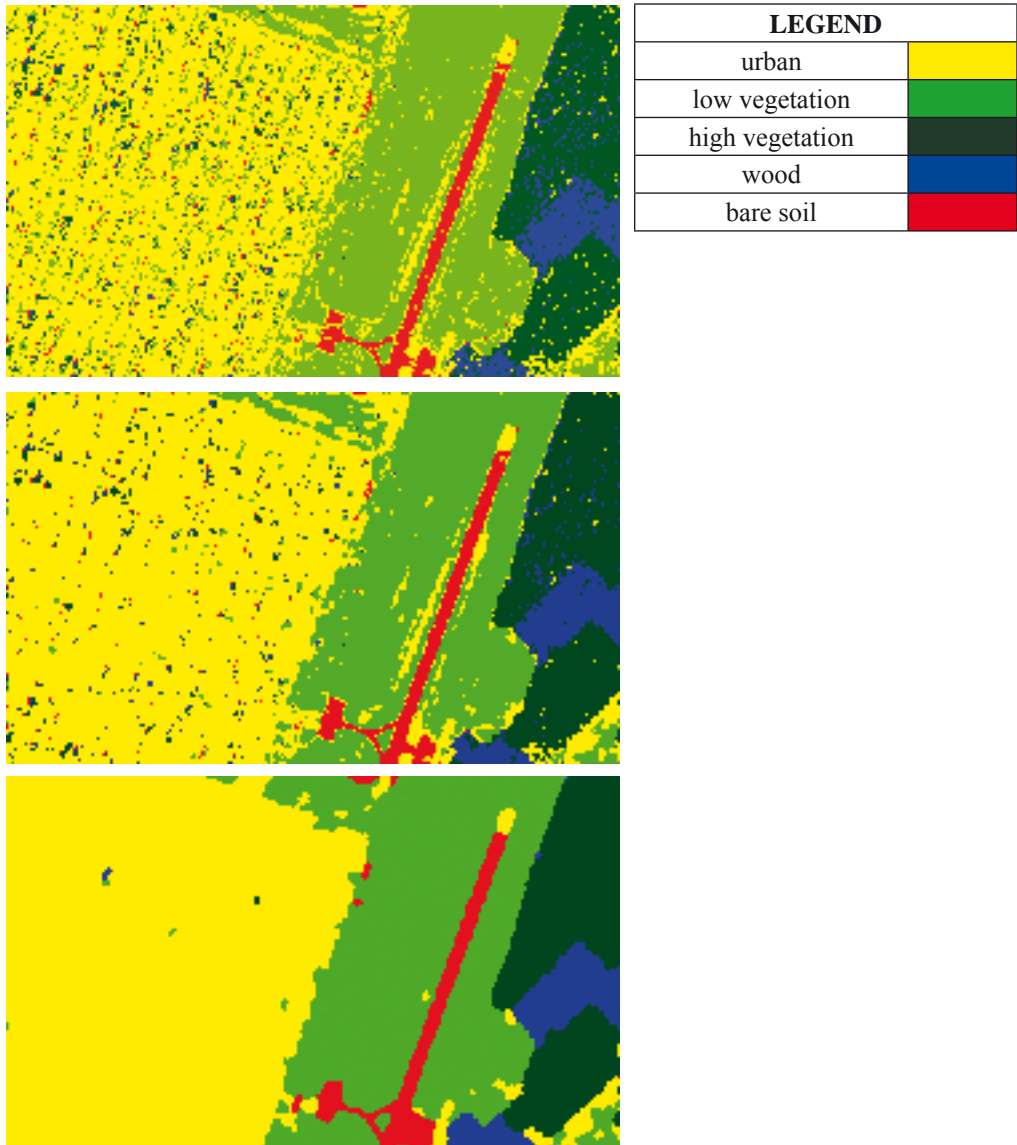
Figure 3 - Experiment 1: classification maps generated by GMAP, Potts-ICM, and HR-ICM.

further penalty terms related to the presence of edges in the image (edges are not explicitly taken into account in the present version of the MRF model).

Experiment 2

A ground-truth map was generated that presented eight thematic classes (*i.e.*, "urban", "low vegetation", "high vegetation", "sparse vegetation", "sea", "sand", "wood" and "bare soil"). Specifically, 4565 training pixels and 4212 test pixels, collected in spatially disjoint sets, were available. The optimal clustering map included 162 clusters, 91 clusters being assigned to "urban", and the remaining 71 clusters being almost evenly distributed among the

other 7 thematic classes. This further confirms the strong heterogeneity of "urban" (also as compared with the other land-cover typologies), which can be interpreted as a consequence of the presence of many distinct material spectral responses directly affecting the clustering result. Table 2 shows the confusion matrices provided by GMAP, Potts-ICM, and HR-ICM over the test set.

Also in this case, the obtained results confirm the greater effectiveness of the contextual approaches, as compared with the non-contextual one: GMAP provides an overall accuracy (OA) equal to 87.46%, whereas Potts-ICM and HR-ICM significantly improved the results,

Table 2 - Experiment 2: confusion matrices for GMAP, Potts-ICM, and HR-ICM.

GMAP									
Test map	Classification map								Class accuracy (%)
	Urban	Low-veg	High-veg	Sparse-veg	Wood	Sand	Sea	Bare-soil	
Urban	556	11	20	52	1	68	17	18	74.83
Low-veg	41	804	6	0	0	0	0	0	94.47
High-veg	0	6	739	0	0	0	47	0	93.30
Sparse-veg	16	2	40	85	0	0	6	6	54.83
Wood	0	0	0	0	774	0	0	0	100
Sand	153	0	0	0	0	360	0	0	70.17
Sea	0	0	9	0	0	0	189	0	95.45
Bare-soil	7	0	0	2	0	0	0	177	95.16
							Overall accuracy (%)		87.46
Potts-ICM									
Test map	Classification map								Class accuracy (%)
	Urban	Low-veg	High-veg	Sparse-veg	Wood	Sand	Sea	Bare-soil	
Urban	605	2	16	55	1	36	15	13	81.42
Low-veg	17	829	1	4	0	0	0	0	97.41
High-veg	0	0	779	0	0	0	13	0	98.35
Sparse-veg	4	2	40	105	0	0	3	1	67.74
Wood	0	0	0	0	774	0	0	0	100
Sand	140	0	0	0	0	373	0	0	72.70
Sea	0	0	0	0	0	0	198	0	100
Bare-soil	0	0	0	2	0	0	0	184	98.92
							Overall accuracy (%)		91.33
HR-ICM									
Test map	Classification map								Class accuracy (%)
	Urban	Low-veg	High-veg	Sparse-veg	Wood	Sand	Sea	Bare-soil	
Urban	675	42	7	0	0	2	0	0	90.84
Low-veg	8	843	0	0	0	0	0	0	99.05
High-veg	0	0	792	0	0	0	0	0	100
Sparse-veg	6	2	54	92	0	0	0	1	59.35
Wood	0	0	0	0	774	0	0	0	100
Sand	151	0	0	0	0	362	0	0	70.56
Sea	0	0	0	0	0	0	198	0	100
Bare-soil	0	0	0	8	0	2	0	176	94.62
							Overall accuracy (%)		92.87

providing values of OA equal to 91.33% and 92.87%, respectively.

Specifically, focusing on the detection accuracies of urban areas, the proposed method provides the best result, yielding a classification accuracy equal to 90.84%, as compared with the 74.83% accuracy of GMAP and the 81.42% accuracy of Potts-ICM. Such results suggest a good effectiveness of the proposed MRF approach to modelling the contextual information related to HR data and to exploiting such information to optimize the discrimination of urban regions.

On the other hand, worse accuracies were given by HR-ICM than by Potts-ICM for "sparse vegetation", "sand" and "bare soil." This is interpreted as a consequence of the small numbers of training samples that were available for such three classes: such numbers corresponded to 3.81%, 8.65%, and 5.26% of the total number of training pixels, respectively.

According to Equation [9], the adopted MAP cluster-labelling strategy is expressed in terms of size of the spatial overlapping of each cluster with the set of training pixels of each thematic class. Even though this rule minimizes the overall probability of classification error [Duda et al., 2001; Serpico et al., 2003], it may penalize the classes with the smallest training-sample sizes. This issue turned out to be especially critical for the above-mentioned three classes because they exhibited considerable spectral overlappings with one another (especially "sparse vegetation" with "bare soil") and/or with other thematic classes that were provided with larger sets of training pixels (e.g., "sparse vegetation" with "low vegetation" and "high vegetation," which represented 22.41% and 17.17% of the training set, respectively, and "sand" with "urban", which made up 13.71% of the training set). This is also confirmed by the fact that "bare soil" was classified with very high accuracy in Experiment 1, even though it was a minority class in the training map of Figure 2 as well. Such a result was obtained thanks to the good spectral separation between "bare soil" and all the other classes considered in the scene of Experiment 1.

Potts-ICM does not perform a cluster-labelling stage and seems to be slightly less sensitive to the training-set sizes of the single classes, even though it provides a globally less accurate result and a lower detection accuracy for "urban".

Conclusions

A novel MRF model for the classification of optical HR data has been developed. Such a model extends the classical MRF models by integrating a relationship between the (user-defined) information classes and the corresponding subclasses, related to different material responses and extracted by a clustering procedure.

The experimental results suggest that the contextual classifier based on the proposed MRF model outperforms the contextual classifier based on the conventional Potts model and the non-contextual MAP classifier for Gaussian classes, thus reducing the typical problems of HR data related to both the considerable spectral overlapping and the great class variance. In particular, a more accurate result was obtained by the proposed approach in the discrimination of the "urban" class; such a result seems to suggest the effectiveness of the proposed hybrid supervised/unsupervised approach to the analysis of this difficult heterogeneous land-cover typology. On the other hand, a slightly higher sensitivity to small-sample-size problems was noticed for the proposed method than for the Potts one, especially in the case of strongly overlapping classes in the feature space. This is due to the direct relationship between the cluster-level MAP rule applied to generate the hybrid classification map and the training-sample size of each class. In order to reduce this sensitivity, alternative cluster-labelling rules, based on the maximum-likelihood approach [Moser et al., 2004] or the minimum-risk one, could be used.

An interesting future development of the present research might involve both the integra-

tion of an edge detection procedure (e.g., based on line processes [Geman et al., 1984]) into the proposed MRF model (in order to improve the capability of the method to correctly detect structures in urban areas) and the extension of the method to anysotropic MRF modelling [Dubes et al., 1986]. A further generalization of the method might lie in the use of different weight parameters for distinct spatial class transitions; it might sharply increase the generality of the MRF model, although at the cost of a larger number of model parameters and of a possibly heavier computational burden.

References

Benediktsson J.A., Arnason K., Pesaresi M. (2002) - *The use of morphological profiles in classification of data from urban areas.* Proc. IEEE/ISPRS Joint workshop on Remote Sensing and Data Fusion Over Urban Areas, pp. 30-34.

Bruzzone L., Prieto D.F. (2000) - *Automatic analysis of the difference image for unsupervised change detection,* IEEE Trans. Geosci. Remote Sensing 38(3): 1171-1182.

Chen Q., Gong P. (2004) - *Automatic Variogram Parameter Extraction for Textural Classification of the Panchromatic IKONOS Imagery.* IEEE Trans. Geosci. Remote Sensing, 42 (5): 1106-1115.

Datcu M., Seidel K., Walessa M. (1998) - *Spatial information retrieval from remote sensing images: Part I. Information theoretical perspective.* IEEE Trans. Geosci. Remote Sensing, 36 (5): 1431-1445.

De Martino M., Macchiavello G., Serpico S.B. (2004) - *Partially supervised classification of optical high spatial resolution images in urban environment using spectral and textural information.* Proc. IGARSS-2004, 1: 77-80.

Dubes R.C., Jain A. K. (1989) - *Random Field models in image analysis.* J. Appl. Stat., 16 (2): 131-163.

Duda R.O., Hart P. E., Stork D.G. (2001) - *Pattern Classification.* 2nd Edition, Wiley Interscience.

Geman S., Geman D. (1984) - *Stochastic relaxation, Gibbs distributions, and the Bayesian restoration.* IEEE Trans. Pattern Anal. Machine Intell., 6(6): 721-741.

Gong P., Howarth P.J. (1990) - *Frequency-based contextual classification and gray-level vector reduction for land-use identification.* Photogramm. Eng. Remote Sensing, 58 (4): 423-437.

Hsu S.Y. (1978) - *Texture tone analysis for automated land-use mapping.* Photogramm. Eng. Remote Sensing, 44(11): 1393-1404.

Jackson Q., Landgrebe D.A. (2001) - *Adaptive Bayesian contextual classification based on Markov Random Fields.* IEEE Trans. Geosci. Remote Sensing, 40 (11): 2454-2463.

Kressler F.P., Bauer T.B., Steinnocher K.T. (2002) - *Object-oriented perparcel land use classification of very high-resolution images.* Proc. IEEE/ISPRS Joint workshop on Remote Sensing and Data Fusion Over Urban Areas, pp. 164-167.

Melgani F., Serpico S.B. (2003) - *A Markov random field approach to spatio-temporal contextual image classification.* IEEE Trans. Geosci. Remote Sensing, 41 (11): 2478-2487.

Moser G., Serpico S.B., De Martino M., Coppolino D. (2004) - *Automatic partially supervised classification of multitemporal remotely sensed images.* Proc. 2004 SPIE Conference on Image and Signal Processing for Remote Sensing X, pp. 126-137.

Pesaresi M. (1999) - *Textural classification of very high-resolution satellite imagery: Empirical estimation of the interaction between window size and detection accuracy in urban environment.* Proc. ICIP-1999, vol. 1: 114-118.

Pesaresi M., Benediktsson J.A. (2001) - *A new approach for the morphological segmentation of high-resolution satellite imagery.* IEEE Trans. Geosci. Remote Sensing, 39 (2): 309-320.

Serpico S.B., Datcu M., Moser G., Mansi S., Pecciarini P. (2003) - *Hybrid supervised/ unsupervised multisensor fusion of remote sensing images based on hierarchical clustering.* Proc. 2003 Tyrrhenian International Workshop on Remote Sensing (TIWRS):17-30.

Serpico S.B., Moser G. (2005) - *MRF model parameter estimation for contextual supervised classification of remote-sensing images.* Submitted to IEEE Trans. Geosci. Remote Sensing.

Serpico S.B., Moser G., Causa F. (2005) - *MRF model parameter estimation for contextual supervised classification of remote-sensing images.* Proc. IGARSS-2005, 1: 308-311.

Smits P., Dellepiane S. (1997) - *Synthetic aperture radar image segmentation by a detail preserving Markov Random Field approach.* IEEE Trans. Geosci. Remote Sensing, 35 (4): 844-857.

Solberg A.H.S., Taxt T., Jain A.K. (1996) - *A Markov Random Field model for classification of multisource satellite imagery.* IEEE Trans. Geosci. Remote Sensing, 34 (1): 100-113.

Storvik G., Fjortoft R., Solberg A.H.S. (2005) - *A Bayesian approach to classification of multiresolution remote sensing data.* IEEE Trans. Geosci. Remote Sensing, 43 (3): 539-547.

Tatem A.J., Lewis H.G., Atkinson P.M., Nixon M.S. (2001) - *Super-resolution mapping of urban scenes from IKONOS imagery using a Hopfield neural network.* Proc. IGARSS-2001, 7: 3203-3205.

Wong Y., Posner E. (1993) - *New clustering algorithm applicable to multispectral and polarimetric SAR images.* IEEE Trans. Geosci. Remote Sensing, 31(3): 634-644.

L'aggiornamento al 2004 della mappa di copertura del suolo della regione Lombardia mediante classificazione di immagini satellitari

Dario Bellingeri, Michele Bocci e Enrico Zini

ARPA Lombardia, Sistemi Informativi Ambientali, v.le Restelli 3/1 - 20124 Milano.
E-mail: d.bellingeri@arpalombardia.it

Riassunto

L'elaborazione semi-automatica di immagini satellitari multitemporali Landsat TM relative all'intero territorio della Regione Lombardia ha consentito la redazione della carta di copertura del suolo aggiornata al 2004, con la stessa metodologia seguita per la redazione della carta ottenuta con immagini del 1999, al fine di analizzare le principali variazioni avvenute sul territorio lombardo, ponendo particolare attenzione ai fenomeni di neo-urbanizzazione.

Parole chiave: Copertura del suolo, neo-urbanizzazione, Lombardia, monitoraggio ambientale

Abstract

A multitemporal set of Landsat TM images has been used to update to 2004 the land cover map of Lombardy. The principal application is to monitor the major land cover changes occurred between 1999 and 2004, with particular attention on urban sprawl phenomena.

Keywords: Land cover, urban sprawl, Lombardy, environmental monitoring

Introduzione

Il progetto SINA SENTINEL-1 "Sistema di Analisi Ambientale mediante Immagini Satellitari" ha per scopo la realizzazione in ARPA Lombardia di un Laboratorio di Telerilevamento per il monitoraggio dell'ambiente [Zini et al., 2003]. Le principali attività del Laboratorio riguardano lo sviluppo di metodiche operative di analisi di immagini satellitari ai fini del monitoraggio della dinamica della copertura del suolo, della mappatura del manto nevoso e dello stato della vegetazione naturale [ARPA RSA, 2006].

Accanto a queste attività a scala regionale ne sono state sviluppate altre a scala locale riguardanti, ad esempio, il monitoraggio dei ghiacciai, basato su immagini stereoscopiche ad altissima risoluzione, e la mappatura delle aree esondate mediante immagini SAR [Bellingeri et al., 2003; Spirolazzi et al., 2004; Bellingeri et al., 2005].

Questo articolo descrive gli ultimi risultati ottenuti dal Laboratorio di Telerilevamento nell'attività di monitoraggio della copertura del suolo, in particolare riferiti all'aggiornamento della carta di copertura del suolo ottenuta dalla classificazione di immagini Landsat dell'anno 2004.

Le principali applicazioni dei risultati del progetto sono monitorare tempestivamente l'espansione delle aree urbanizzate ed i principali mutamenti nel territorio agrario e delle aree naturali, fornire statistiche aggiornate di copertura del suolo a livello comunale e di

bacini idrografici, stimare le superfici impermeabilizzate ed i coefficienti di infiltrazione e la loro variazione nel tempo, permettere la redistribuzione di alcuni parametri statistici dal livello comunale ad altre unità geografiche per, ad esempio, la stima dei carichi inquinanti potenziali sulle acque.

Il progetto per il monitoraggio della copertura del suolo sviluppato dal Laboratorio di Telerilevamento di ARPA Lombardia si basa su alcuni principi, come la standardizzazione delle procedure e la ripetibilità delle tecniche di analisi, e la possibilità di aggiornamento dei prodotti in tempi relativamente rapidi.

La standardizzazione delle procedure è affidata in primo luogo alla omogeneità dei dati e quindi alla fonte dei dati stessi. Un programma di monitoraggio delle dinamiche evolutive del territorio deve necessariamente basarsi sull'impiego di immagini telerilevate dallo stesso sensore, o quantomeno da sensori con caratteristiche spettrali e geometriche confrontabili.

Per quanto riguarda la ripetibilità delle tecniche di analisi ci si riferisce alla metodologia di elaborazione dei dati di base per l'estrazione del contenuto tematico. Per la programmazione di una attività di monitoraggio è fondamentale disporre di una metodologia replicabile con omogeneità procedurale, in modo che i dati prodotti possano essere confrontati per l'individuazione di fenomeni di mutamento ambientale.

La possibilità di realizzare la cartografia tematica in oggetto in tempi relativamente brevi (pochi mesi dopo l'acquisizione delle immagini satellitari), garantisce di ottenere una visione aggiornata delle principali variazioni riscontrabili sul territorio, in modo da poter stimare gli impatti sull'ambiente e fornire uno strumento efficace di pianificazione del territorio. I tradizionali strumenti di analisi territoriale, come ad esempio la fotointerpretazione di immagini aeree, se da un lato hanno migliori caratteristiche di dettaglio spaziale o tematico, spesso non consentono una visione aggiornata di un territorio, come quello lombardo, caratterizzato da una notevole dinamica.

Descrizione dei dati utilizzati e delle cartografie tematiche prodotte

Alla luce di una valutazione del rapporto costi/benefici, si è ritenuto che le immagini Landsat TM fornissero una informazione adeguata agli scopi di un monitoraggio a scala regionale a fronte di un costo relativamente contenuto che permette di acquisire più riprese nel corso di uno stesso anno (migliorando l'accuratezza della classificazione) e di ripetere le acquisizioni a distanza di due o tre anni per aggiornare la classificazione.

La mappa di copertura del suolo della Lombardia è stata ottenuta da una serie multitemporale di immagini satellitari Landsat TM acquisite nell'anno 2004; una precedente versione della carta, realizzata con metodologia analoga, è riferita al 1999.

In Figura 1 sono riassunte le date di acquisizione delle immagini satellitari Landsat scelte per il 2004, in relazione alle differenti scene che interessano il territorio lombardo.

Le quattro scene Landsat che interessano il territorio lombardo presentano delle sovrapposizioni che sono di grande utilità per minimizzare il disturbo dato dalla nuvolosità. Le date di acquisizione, compatibilmente alla disponibilità di immagini il più possibile libere da nubi, sono state scelte in periodi rappresentativi in relazione ai cicli fenologici delle principali colture presenti nell'area. In particolare, sono state scelte immagini che coprissero il periodo primaverile, estivo e di inizio autunno (anche per garantire l'acquisizione di immagini con buona luminosità generale, buon rapporto segnale/disturbo e per ridurre le ombre topografiche).

Considerate le caratteristiche geometriche delle immagini satellitari utilizzate, la scala di utilizzo delle classificazioni tematiche prodotte è 1:50.000 mentre l'area minima classificata è pari a tre pixel contigui, corrispondenti a 2700 m².

La legenda delle carte di copertura del suolo prodotte è a 2 livelli, di 11 e 19 classi tematiche (dettagliate in Tab. 1).
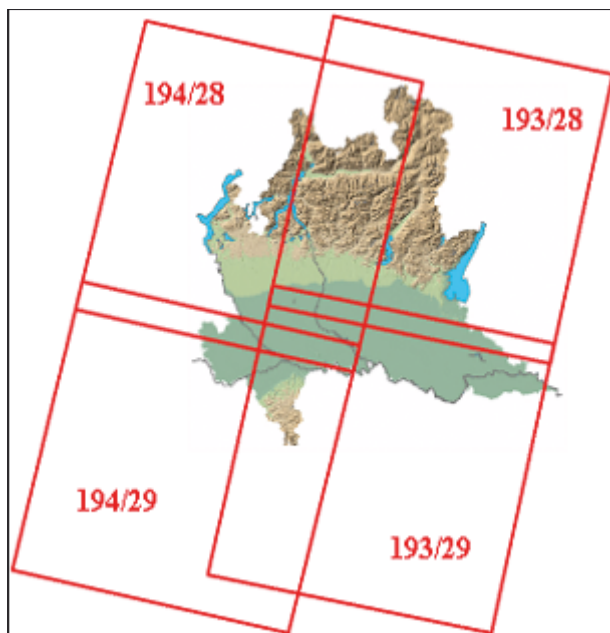
Scena	2004
194-28	17 marzo
	20 maggio
	9 settembre
	25 settembre
194-29	17 marzo
	20 maggio
	9 settembre
	25 settembre
193-28	11 aprile
	1 agosto
	18 settembre
193-29	11 aprile
	1 agosto
	18 settembre

Figura 1 - Copertura della Lombardia delle scene Landsat e date acquisite per il 2004.

Pre-elaborazioni e classificazione delle immagini

Le immagini satellitari Landsat sono state sottoposte ad una serie di pre-elaborazioni, al fine di renderle adatte alle fasi successive di classificazione. Tutte le fasi di pre-elaborazione delle immagini sono state effettuate utilizzando gli stessi standard seguiti per le immagini del 1999, al fine di ottenere dati di base e prodotti il più possibile confrontabili.

Ortoproiezione delle immagini

Le immagini satellitari Landsat, opportunamente trasformate nel formato .img di ERDAS Imagine, sono state georiferite utilizzando il software ERDAS *OrthoBase*, con un modello specifico per il sensore in oggetto, che implementa l'ortoproiezione. Tale procedura è assolutamente necessaria per garantire la corretta sovrapponibilità delle immagini (e dei prodotti derivati) alla cartografia esistente, eliminando le distorsioni presenti nelle immagini (distorsioni panoramiche, dovute all'ottica di ripresa, errori di parallasse, ecc…). Più in particolare la georeferenziazione delle immagini è stata effettuata utilizzando dei set di punti di controllo (GCP, in media 21 per scena) individuati sulle ortoimmagini ed il modello digitale di elevazione del terreno con passo di 40 metri sull'intero territorio regionale. Per il ricampionamento si è utilizzato l'algoritmo *"Nearest Neighbour"*, al fine di non modificare i valori spettrali originali. L'errore di georeferenziazione medio (RMSE, *Root Mean Square Error*) per le diverse scene Landsat, verificato tramite una serie di punti di verifica (VP, in media 15 per scena) indipendenti, è risultato di 0,63 pixel (pari a circa 19 metri).

Eliminazione nuvole e ombre connesse e ombre topografiche

Al fine di garantire la migliore accuratezza possibile nella fase di classificazione semi-automatica delle immagini è stato necessario "ripulire" quelle aree all'interno delle immagini che presentano risposte spettrali anomale. Tali aree sono costituite essenzialmente da nu-

Tabella 1- Legenda lc2004, versione a 19 classi.

Classe	Codice	Descrizione
Antropizzato non vegetato	1.1.	Superfici antropizzate non vegetate: edificato di tipo residenziale, commerciale e industriale, cantieri, aree di cava non vegetate
Verde urbano arboreo	1.2.	Verde urbano (pixel vegetati ma appartenenti alla "urbanizzato" nello strato accessorio DUSAF) prevalentemente arboreo
Verde urbano erbaceo	1.3.	Verde urbano (pixel vegetati ma appartenenti alla "urbanizzato" nello strato accessorio DUSAF) prevalentemente erbaceo
Seminativi - generici	2.1.	Seminativi per i quali, causa insufficienti informazioni multitemporali o risposte spettrali non univoche, non è stata possibile l'assegnazione alle classi 2.2, 2.3, 2.4, 2.5, 2.6 o 2.7
Seminativi -invernali	2.2.	Superfici agricole vegetate nel periodo primaverile-inizio estivo e non vegetate in estate inoltrata (es.: frumento, orzo, ecc..)
Seminativi - estivi	2.3.	Superfici agricole non vegetate nel periodo primaverile, vegetate in estate inoltrata (es.: mais, soia, ecc..)
Seminativi - doppio raccolto	2.4.	Superfici agricole vegetate nel periodo inizio-primaverile, non vegetate in tarda primavera-inizio estate, di nuovo vegetate in estate inoltrata (es.: rotazioni colturali frumento/mais a crescita breve, ecc...)
Seminativi - mai vegetati	2.5.	Superfici agricole non vegetate in tutte le date analizzate
Seminativi - foraggere	2.6.	Superfici agricole con risposta vegetativa costantemente bassa in tutte le date analizzate
Seminativi - risaie	2.7.	Superfici agricole caratterizzate da andamento spettrale nel tempo compatibile con l'andamento fenologico delle risaie
Colture permanenti e arboree	3.	Colture permanenti e arboree, legnose agrarie
Latifoglie	4.	Vegetazione arborea prevalentemente di latifoglie
Conifere	5.	Vegetazione arborea prevalentemente di conifere
Cespuglieti	6.	Vegetazione prevalentemente arbustiva, comprende la vegetazione cespugliosa o rada negli alvei fluviali
Prati e praterie	7.	Prati e praterie alpine, anche con presenza di vegetazione arborea sparsa
Vegetazione rada	8.	Vegetazione erbacea rada di alta quota
Rocce, ghiaie	9.	Superfici naturali non vegetate: rocce, ghiaie, greti fluviali
Corpi idrici	10.	Corpi idrici: fiumi, laghi, maggiori canali irrigui, laghi di cava
Nevi e ghiacci	11.	Superfici coperte da neve o ghiacci, al minimo della loro estensione

vole e dalle rispettive ombre al suolo e dalle ombre prodotte dai versanti non illuminati per motivi orografici. Nel primo caso si è proceduto con la digitalizzazione a video dei corpi nuvolosi e delle relative ombre proiettate a terra, con scale di lavoro comprese tra 1:75.000 e 1:150.000. Sono state costruite quindi delle banche dati vettoriali e da queste delle maschere binarie delle aree non osservabili a causa delle nuvole. Per quanto riguarda le ombre topografiche, invece, è stata utilizzata una procedura di riconoscimento automatico utilizzando il software ATCOR, un modulo aggiuntivo specifico per l'ambiente ERDAS *Imagine*.

Tale modulo implementa un procedura per il riconoscimento delle aree non illuminate al momento delle acquisizioni delle immagini, utilizzando come input i valori di azimut ed elevazione solare al momento del passaggio del satellite ed il modello altimetrico del terreno. Sono quindi state prodotte delle specifiche maschere binarie che, integrate poi con quelle relative alla copertura nuvolosa hanno consentito di obliterare le porzioni di immagini satellitari caratterizzate da risposta spettrale anomala.

Correzioni radiometriche e topografiche

Le correzioni radiometriche delle immagini sono state effettuate al fine di ottenere dei valori fisici di riflettività spettrale, a partire dai *Digital Number* originari, utilizzando i coefficienti di calibrazione associati alle immagini. Le correzioni topografiche sono state invece necessarie per minimizzare il disturbo causato dagli effetti dell'orografia sul segnale registrato dal satellite. Quest'ultima operazione risulta di fondamentale importanza, in particolare per un territorio con notevoli variazioni morfologiche come quello lombardo. Nelle aree a forte intensità di rilievo i versanti a diversa esposizione, ma con le stesse tipologie di copertura del suolo, danno origine a segnali di entità differente, che condizionano negativamente le successive fasi di classificazione. Ad esempio, in versanti esposti a nord i boschi di latifoglie possono presentare una risposta spettrale simile alle conifere, tipicamente meno riflettenti. Le correzioni radiometriche e topografiche hanno consentito di ridurre in maniera drastica tali effetti, mediante la generazione di immagini in cui la risposta radiometrica nei vari tipi di versanti viene corretta attraverso la ricostruzione della geometria dei raggi incidenti e riflessi. Questi due tipi di pre-elaborazione sono stati condotti utilizzando il modulo ATCOR-3 per ERDAS.

La classificazione per ambiti territoriali: stratificazione del territorio

Per raggiungere un maggiore potere risolutivo nella classificazione della copertura del suolo è stato sviluppato un metodo di classificazione che prevede il trattamento separato delle immagini per aree fisiografiche. Tale impostazione presenta due importanti vantaggi:
- in ogni area fisiografica sono possibili solo certe tipologie di copertura del suolo in riferimento a particolari firme spettrali;
- realizzando immagini "mascherate" in cui è visibile e classificabile solo un singolo dominio fisiografico si ottiene una più accurata distinzione delle varie tipologie presenti in quel contesto specifico, per l'assenza dei segnali provenienti da aree differenti che aumenterebbero la dispersione dei valori nello spazio spettrale di tutte le bande utilizzate.

Per ogni area fisiografica è stata quindi individuata la migliore strategia di classificazione e post-classificazione, in funzione delle peculiarità dei vari ambienti fisici.

Il territorio della Regione Lombardia è stato suddiviso in tre ambiti omogenei dal punto di vista fisiografico:

1) Ambito agricolo e antropico – in questi territori le tematiche di classificazione sono caratterizzate dai seguenti fenomeni:
   a) elevata variabilità di risposta spettrale delle varie colture, sia per differenze specifiche che per fasi fenologiche;
   b) possibili sovrapposizioni di risposta spettrale tra territori non vegetati, afferenti sia al dominio agricolo che a quello delle aree antropiche edificate.
   Per raggiungere un livello di accuratezza soddisfacente, in tale area fisiografica risulta indispensabile l'uso di più immagini a differente periodo di acquisizione nello stesso anno, inserendo regole di postclassificazione "multitemporali".

2) Ambito naturale – per la discriminazioni delle diverse tipologie di ambiente naturale, dopo aver sperimentato varie tecniche di classificazione, si è scelto di classificare la sola

data estiva, per la migliore illuminazione e per condizioni maggiormente omogenee negli stadi fenologici delle varie specie e nei vari ambienti. Le date primaverili e autunnali presentano infatti delle variazioni nella risposta della vegetazione verde non omogenee in tutto il territorio, che portano ad una minor accuratezza nella classificazione.

3) Ambito dei corpi idrici – tale ambito comprende, oltre ai corpi idrici veri e propri, anche le aree naturali limitrofe. Si è posta una particolare attenzione a non includere i pioppeti, frequenti nelle fasce fluviali, in modo che le aree riflettenti presenti in tale dominio potessero essere classificate come greti fluviali, senza il rischio di includere tali colture arboree di recente impianto, o appena tagliate. Anche per questo ambito si è scelto di classificare solo la data estiva.

La classificazione delle immagini

Per quanto riguarda i due ambiti fisiografici "Naturale" e "Corpi Idrici", sono state effettuate le classificazioni ISODATA, con assegnazione diretta dei cluster prodotti alle diverse classi di copertura.

Per quanto riguarda l'ambito "Agricolo e Antropico", invece, sono state prodotte delle classificazioni ISODATA intermedie, con l'assegnazione dei cluster in tipologie semplificate di copertura del suolo, sfruttando, nella fase di caratterizzazione delle classi (operata per via fotointerpretativa), la multitemporalità delle immagini (ad esempio, distinguendo le macro-tipologie di seminativi sulla base della loro fenologia). A tali strati temporanei sono state quindi applicate delle operazioni di post-classificazione, che incrociano la codifica intermedia con l'informazione derivante dalla classificazione di copertura del suolo precedente (lc1999) e dallo strato informativo accessorio DUSAF (Destinazione d'Uso dei Suoli Agricoli e Forestali, ERSAF e Regione Lombardia), derivato per fotointerpretazione delle ortofoto IT2000.

Utilizzando questa procedura, ad esempio, le aree già classificate come antropizzate nel 1999, possono assumere solamente la codifica 1.1 (antropizzato non vegetato), 1.2 (verde urbano arboreo) o 1.3 (verde urbano erbaceo). L'altra classe interessata da queste regole di post-classificazione basate su dati ancillari è la classe 3 (colture permanenti e arboree): formata da tipologie di colture agrarie, come vigneti e frutteti, difficilmente individuabili utilizzando solo le immagini Landsat multitemporali.

Revisione fotointerpretativa

Lo strato raster ottenuto è stato sottoposto ad una revisione generale di carattere fotointerpretativo, utilizzando tre differenti tipologie di immagini satellitari:

− mosaico delle immagini Landsat (relative al mese di settembre 2004), ricampionate con pixel di 25 metri, con algoritmo di ricampionamento *Cubic Convolution* (disponibile per l'intero territorio regionale);

− immagini a media risoluzione ASTER (risoluzione a terra di 15 metri), acquisite fra il 2003 ed il 2004, disponibili in porzioni limitate del territorio lombardo.

− immagini a media risoluzione SPOT (risoluzione a terra di 20 metri), acquisite nel 2004, disponibili in porzioni limitate del territorio regionale.

In particolare, questa fase di revisione è stata utile per le aree potenzialmente neourbanizzate dal 1999 al 2004: le aree soggette ad un cambio di codifica "non antropizzato" nel 1999 ad "antropizzato" nel 2004 sono state trasformate in uno strato vettoriale. Tali poligoni, sulla base dell'analisi fotointerpretativa sono quindi stati confermati come classe 1.1 (antropizzato) oppure, nel caso di porzioni di territorio agricolo mai vegetate nelle date di acquisizione, ricodificati come classe 2.5 (seminativi mai vegetati).

Verifica dell'accuratezza tematica

Per la verifica dell'accuratezza della mappa di copertura del suolo, sono stati acquisiti manualmente 540 punti di verità al suolo, mediante sessioni di fotointerpretazione sulla base di immagini ad alta risoluzione IKONOS (pancromatiche e multispettrali, risoluzione geometrica di 1 e 4 metri) acquisite nel 2004 su quattro aree campione della Regione Lombardia, in territori con caratteristiche molto differenti fra loro e quindi ritenute sufficiente rappresentative delle tipologie di coperture del suolo lombarde (Fig. 2-B): est milanese e Mantova (aree urbanizzate e rurali), Ostiglia (area prevalentemente rurale), Valfurva (area rurale e montana), per un totale di 470 km² (pari a circa il 2% della superficie regionale).

Per valutare l'accuratezza tematica della carta del 1999 furono invece utilizzati 2044 punti di verità a terra fotointerpretati sulla base delle riprese aeree IT2000 (foto aeree riprese nel 1999) (Fig. 2-A). L'accuratezza globale ("*overall accuracy*") per la carta "lc_2004" (Fig.3) è del 87%, valore compatibile e confrontabile con l'accuratezza ottenuta per la mappa di copertura del suolo relativa al 1999 (85,4%).

Si riscontrano valori di accuratezza mediamente più bassi per le classi di vegetazione naturale, mentre per la classe 1-Antropizzato l'accuratezza è più alta ("*user's accuracy*" del 97%, "*producer's accuracy*" dell'89%), anche grazie alla fase manuale di revisione fotointerpretativa.
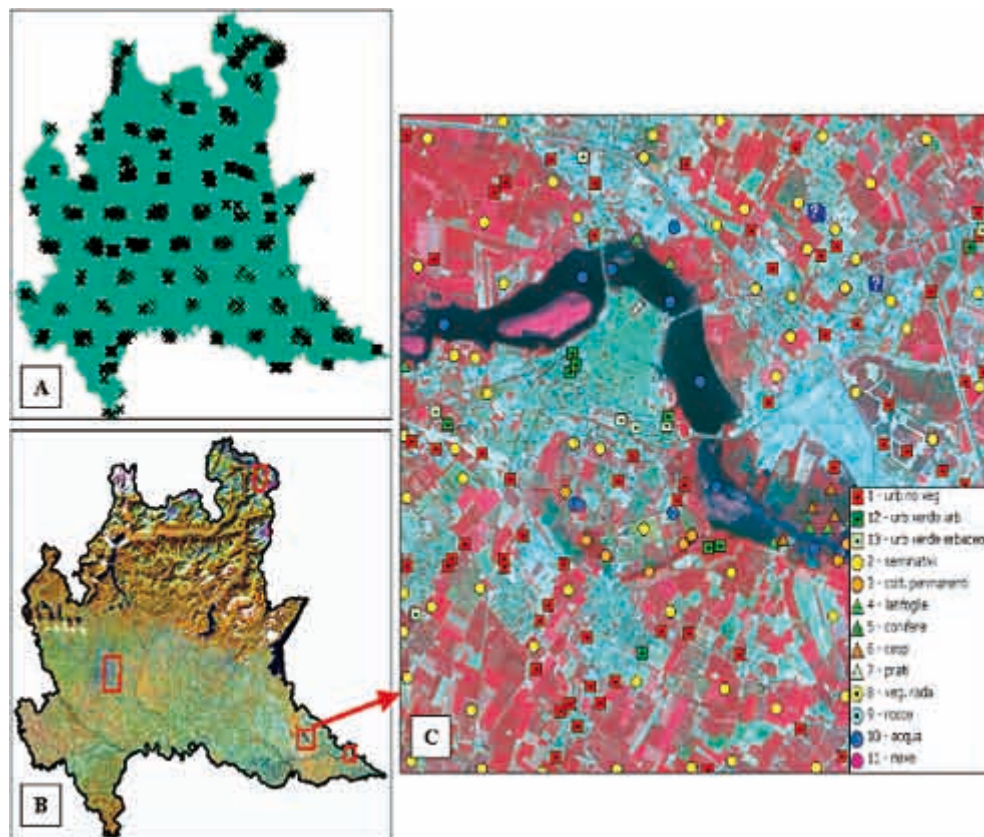

Figura 2 - A) Localizzazione dei 2044 punti di verità a terra fotointerpretati sulle ortofoto IT2000 e utilizzati per la validazione della carta "lc_1999"; B) Localizzazione delle aree acquisite nel 2004 con dati ad alta risoluzione e disponibili per la verifica dell'accuratezza di "lc_2004"; C) Dettaglio dei punti di verità a terra individuati sull'immagine IKONOS ripresa nel 2004 sulla città di Mantova.
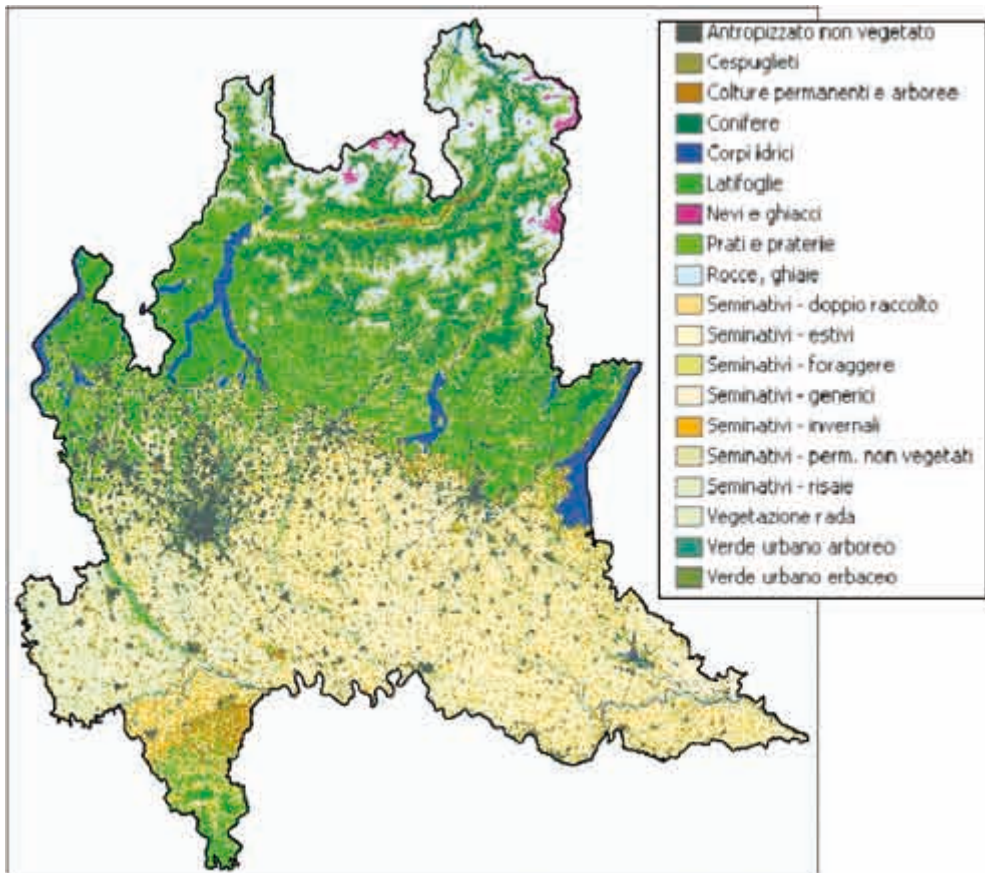
Figura 3 - Carta di Copertura del suolo della Lombardia aggiornata al 2004, con tematizzazione estesa a 19 classi.

Analisi delle transizioni 1999/2004 e analisi delle superfici neo-antropizzate

Al fine di descrivere i cambiamenti avvenuti nel territorio lombardo nel quinquennio 1999-2004, è stato creato uno strato raster risultante dall'incrocio tematico dei due *land cover*.

La Tabella 2 descrive le transizioni fra le carte di copertura del suolo del 1999 e del 2004, espresse in km².

Per analizzare in modo sintetico le principali transizioni, i cambiamenti sono stati ricodificati secondo un codice sintetico a 4 classi (Tab. 3).

La Tabella 4 descrive le principali transizioni rilevate dal 1999 al 2004, sintetizzate secondo il codice sintetico a 4 classi e sempre espresse in km².

L'espansione delle superfici antropizzate, fra i temi dell'evoluzione del territorio, è quello dotato della maggiore dinamicità e si connota per la complessità degli impatti sull'ambiente.

La Figura 4 sintetizza le aree caratterizzate da espansione, dalla cartografia di copertura del suolo del 1999 a quella riferita al 2004, della classe sintetica "1-antr". Spiccano in modo particolare i cambiamenti dalla classe "agricolo" nel 1999 ad "antropizzato" nel 2004. Le transizioni fra classe "1-antr" a "4-acq" sono in maggior parte da ricondursi alle variazioni areali dei laghi di cava.

In particolare il principale incremento di aree neo-urbanizzate risulta nelle aree metropoli-

Tabella 2 - Matrice delle transizioni fra le classi lc_1999 e lc_2004, espresse in km².

		1.1	1.2	1.3	2.1	2.2	2.3	2.4	2.5	2.6	2.7	3	4	5	6	7	8	9	10	11	TOT
	1.1	1382,9	199,1	411,2	0,0	0,0	0,0	0,0	0,0	0,3	0,0	0,7	1,0	0,0	0,1	0,4	0,1	0,1	2,4	0,0	1998,3
	1.2	52,1	115,5	56,2	0,0	0,0	0,0	0,0	0,0	0,1	0,0	0,1	0,7	0,0	0,1	0,1	0,0	0,0	0,3	0,0	225,3
	1.3	222,3	89,2	362,0	0,0	0,0	0,0	0,0	0,0	1,0	0,0	0,6	1,0	0,0	0,3	0,5	0,1	0,1	2,0	0,0	679,1
	2.1	2,8	0,1	1,1	85,0	47,3	299,0	79,6	21,7	46,2	6,1	7,5	0,7	0,0	0,1	0,0	0,0	0,0	0,5	0,0	597,7
	2.2	5,6	0,0	0,6	1,6	79,2	214,7	136,8	26,1	60,3	4,1	2,9	0,1	0,0	0,0	0,0	0,0	0,0	0,5	0,0	532,5
	2.3	64,7	1,3	9,9	67,2	251,1	3133,3	613,4	154,2	732,8	698,6	111,2	10,9	0,0	0,9	1,3	0,4	0,1	7,3	0,0	5858,6
Classi lc_1999	2.4	13,4	0,1	1,3	2,0	72,2	430,3	638,8	19,2	192,3	12,4	8,7	0,5	0,0	0,1	0,1	0,0	0,0	1,0	0,0	1292,4
	2.5	6,3	0,0	0,1	1,0	17,5	104,6	24,4	19,6	16,0	10,6	2,4	0,0	0,0	0,0	0,0	0,0	0,0	0,8	0,0	203,4
	2.6	15,8	0,6	1,4	8,0	50,1	216,5	128,6	27,0	912,7	8,6	6,6	1,5	0,3	0,3	0,0	0,0	0,2	0,9	0,0	1379,1
	3	2,9	0,4	1,2	7,2	20,9	103,8	12,2	26,3	61,5	9,2	558,3	4,0	0,0	0,4	0,1	0,0	0,2	1,3	0,0	810,3
	4	8,5	0,9	2,2	0,0	0,1	0,9	0,2	0,1	1,2	0,1	1,0	3795,4	10,0	9,8	3,3	1,5	0,9	23,6	0,0	3859,6
	5	0,3	0,1	0,0	0,0	0,0	0,0	0,0	0,0	0,0	0,0	0,0	7,6	1752,5	7,6	0,6	0,4	0,5	0,1	0,1	1769,9
	6	4,0	0,7	0,5	0,0	0,0	0,5	0,1	0,0	0,5	0,0	0,5	14,3	10,1	1004,1	8,1	3,5	2,3	17,8	0,2	1067,2
	7	2,2	0,8	1,0	0,0	0,0	0,0	0,0	0,0	0,0	0,0	0,0	3,6	0,0	12,4	953,6	27,2	4,7	0,2	0,0	1006,6
	8	0,8	0,0	0,0	0,0	0,0	0,0	0,0	0,0	0,0	0,0	0,0	1,3	1,5	16,2	14,2	806,4	8,0	0,7	0,4	849,5
	9	1,5	0,0	0,4	0,0	0,0	0,2	0,0	0,0	0,0	0,0	0,0	1,8	0,4	3,7	1,1	6,1	848,2	19,8	29,7	912,9
	10	1,2	0,0	0,0	0,0	0,0	0,1	0,0	0,0	0,0	0,0	0,1	13,8	0,0	15,5	0,0	0,0	6,4	670,2	0,0	707,5
	11	0,0	0,0	0,0	0,0	0,0	0,0	0,0	0,0	0,0	0,0	0,0	0,0	0,0	0,1	0,1	0,6	7,3	0,0	77,7	85,7
	TOT	1787,4	408,7	849,1	172,0	538,5	4504,1	1534,2	294,3	2025,0	749,8	700,7	3868,1	1775,9	1071,8	983,7	846,4	878,8	749,5	108,0	23835,9

Tabella 3 - Ricodifica delle tipologie di *land cover* in 4 classi sintetiche.

codice	descrizione	classi appartenenti
1-antr	antropizzato	1.1, 1.2, 1.3
2-agr	agricolo	2.x, 3
3-nat	naturale	4, 5, 6, 7, 8, 9, 11
4-acq	acqua	10

Tabella 4 - Matrice sintetica delle transizioni 1999-2004, secondo 4 macro classi (1: antropizzato, 2: aree agricole, 3: aree naturali, 4: acqua), valori in km².

		2004				
		1-antr	2-agr	3-nat	4-acq	TOT
1999	1-antr	2890,5	2,8	4,6	4,7	2902,7
	2-agr	129,6	10509,9	22,5	12,3	10674,2
	3-nat	23,8	5,7	9459,7	62,2	9551,4
	4-acq	1,2	0,2	35,8	670,2	707,5
	TOT	3045,2	10518,6	9522,7	749,5	23835,9

tane ricadenti nei territori di pianura delle province di Milano, Bergamo, Brescia, mentre per le aree montane e pedemontane, gli incrementi rilevabili si individuano soprattutto lungo le arterie che attraversano le principali valli.

Approfondimenti tematici ed analisi a scala locale

Con il monitoraggio periodico delle condizioni di *land cover* attraverso elaborazioni di immagini satellitari sono possibili sia analisi specifiche per la quantificazione di questo fenomeno a scala regionale che elaborazioni per la produzione di tematismi derivati, utili per le attività di monitoraggio ambientale e territoriale. A titolo di esempio, nella Figura 5 è riportata la sintesi della distribuzione delle nuove espansioni di urbanizzato in relazione alle categorie di destinazione d'uso, informazione contenuta nella banca dati MISURC (Mosaico Informatizzato degli Strumenti Urbanistici Comunali, Regione Lombardia).
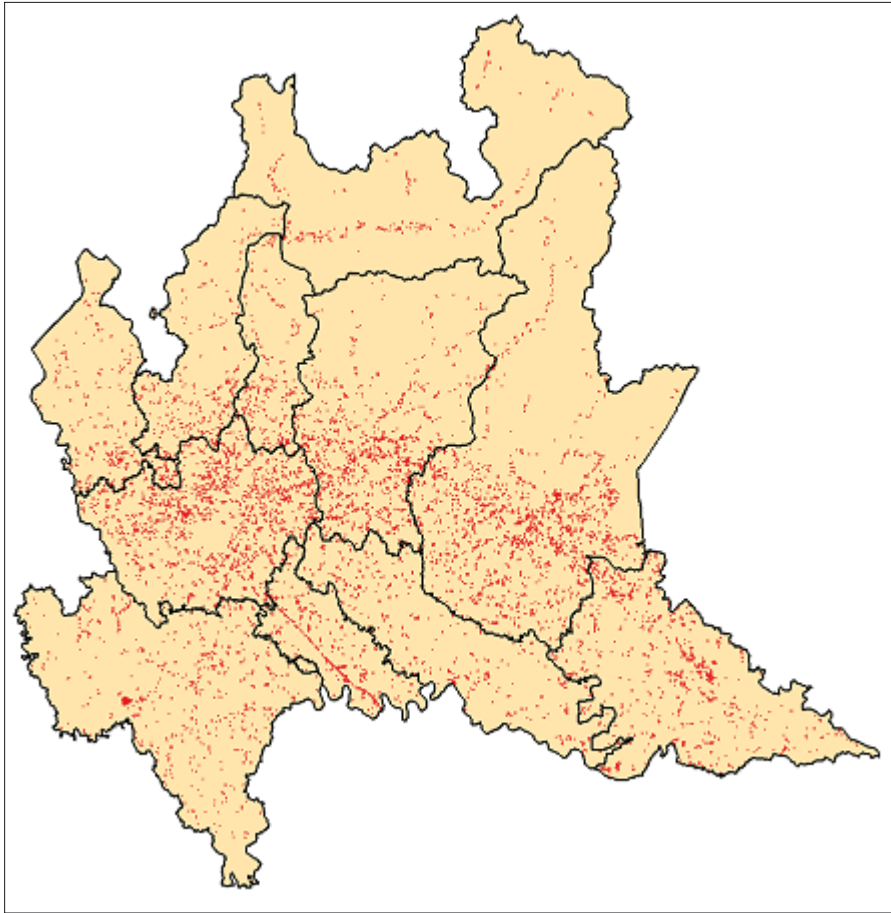
Figura 4 - Tematizzate in rosso, le aree caratterizzate dall'espansione dell'antropizzato dal 1999 al 2004.
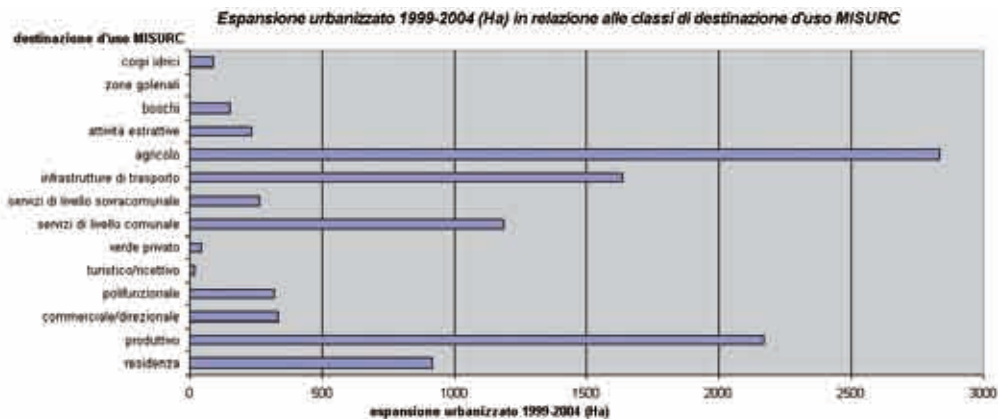

Figura 5 - Distribuzione delle conversioni da superfici agricole ad antropizzate rispetto alle categorie di destinazione d'uso MISURC (dati disponibili per il 68% del territorio regionale, e per circa il 90% della pianura lombarda).

Tale tipo di analisi, condotta a scala regionale con un dato satellitare a media risoluzione come le immagini Landsat TM, è funzionale inoltre all'identificazione dei territori sottoposti alle maggiori pressioni ambientali ed ai maggiori tassi di neo-urbanizzazione, sui quali approfondire le analisi anche con dati satellitari di maggiore dettaglio spaziale, utilizzando differenti metodologie di analisi, come la segmentazione e la classificazione di tipo *object oriented* [Valentini et al., 2002; Bellingeri et al., 2002]. Tale approccio è stato seguito in diverse *aree test* della Lombardia (Milano, Mantova, Valfurva, pianura mantovana), utilizzando immagini ad alta risoluzione IKONOS acquisite nel 2004, e sperimentando sia il software *FeatureAnalyst* per ERDAS che *eCognition*.

Gli *output* delle elaborazioni dei dati satellitari, che sono sostanzialmente delle cartografie di copertura del suolo, pur con differenti caratteristiche tematiche e spaziali, vanno integrati con altre tipologie di informazioni georeferenziate di rilevanza ambientale, nell'ottica della costruzione e del costante aggiornamento di un "sistema informativo ambientale di uso del suolo" di ARPA Lombardia.

Nella Figura 6, ad esempio, si riporta la sovrapposizione della cartografia semplificata di copertura del suolo, ottenuta tramite segmentazione e classificazione *object-oriented* di un'immagine IKONOS del dicembre 2004, e dell'archivio georeferenziato delle attività produttive.

Conclusioni e sviluppi futuri

La redazione della carta di copertura del suolo per l'intero territorio della Lombardia, ottenuta utilizzando un set multitemporale di immagini Landsat, ha permesso la creazione di un data set geografico aggiornato al 2004, ed ha consentito l'individuazione dei principali
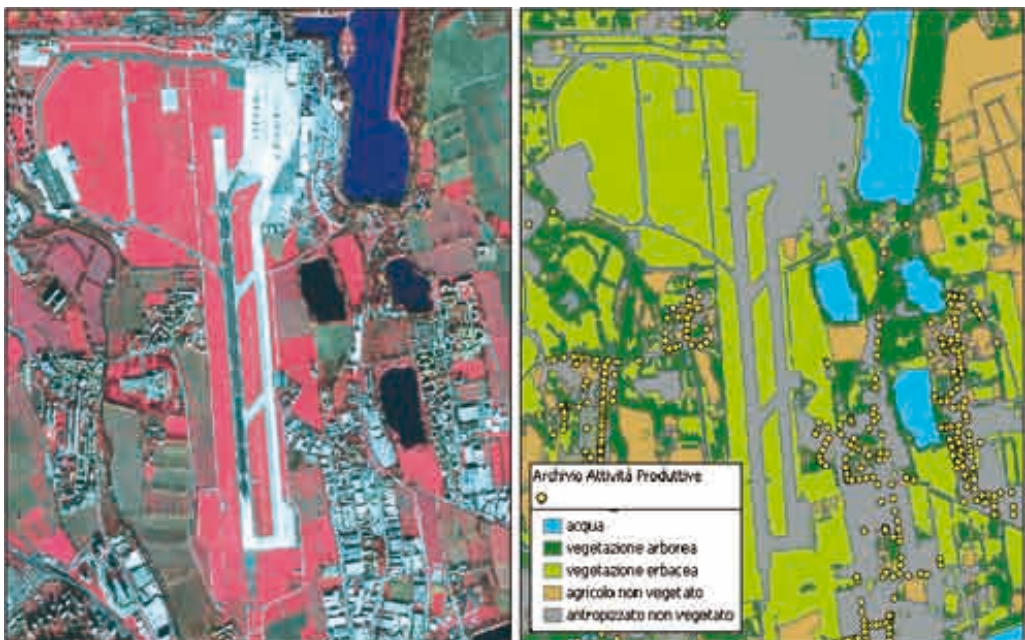

Figura 6 - Esempio nell'area di Milano-Linate di incrocio fra una carta di copertura del suolo (a destra) derivata da immagini IKONOS (a sinistra) con approccio *object oriented* usando il *software FeatureAnalyst*, e dati puntuali relativi all'archivio georeferenziato delle attività produttive.

fenomeni di cambiamento del territorio, in particolare l'aumento considerevole delle aree antropizzate nella fascia dell'alta pianura.

Le analisi sulle dinamiche evolutive del territorio si inseriscono nel quadro delle attività di monitoraggio e modellazione delle fenomenologie ambientali con l'obiettivo di poter disporre di dati sempre aggiornati sulle condizioni di uso e copertura del suolo.

Tale tipo di analisi, condotto a scala regionale, è funzionale inoltre all'identificazione dei territori sottoposti alle maggiori pressioni ambientali ed ai maggiori tassi di neo-urbanizzazione, sui quali approfondire le analisi anche con dati satellitari di maggiore dettaglio spaziale. Sono in corso attività per la definizione di procedure per la generazione di uno strato informativo di Uso del Suolo, inteso come uno dei prodotti del Sistema Informativo Ambientale di ARPA Lombardia, in cui l'informazione sul *land cover* derivata dalle immagini satellitari si integri con le altre informazioni degli archivi territoriali, come le altre cartografie tematiche, l'archivio georeferenziato delle attività produttive, strati tematici relativi alle pianificazioni territoriali, informazioni sulla demografia, e con gli altri archivi georeferenziati di carattere ambientale.

Bibliografia

ARPA Lombardia (2006) - *RSA, Rapporto sullo Stato dell'Ambiente in Lombardia.* Edizione 2005/2006, pp. 19-28; 133-134.

Bellingeri D., Bocci M., Zini E., Menin A. (2003) - *Il progetto Sentinel-1: creazione del laboratorio di Telerilevamento di ARPA Lombardia. Attività e primi risultati.* Atti 7° Conferenza Nazionale ASITA, Verona, Ottobre 2003, 255-260.

Bellingeri D., Colombo R., Fasolini D., Cognigni L. (2002) - *Utilizzo di dati satellitari ad alta risoluzione IKONOS per l'aggiornamento di cartografia tematica e per l'estrazione di parametri biofisici.* Atti 6° Conferenza Nazionale ASITA, Perugia, Novembre 2002.

Bellingeri D., Zini E. (2005) - *Utilizzo di immagini IKONOS stereoscopiche per il monitoraggio dei ghiacciai e per la stima del volume di accumuli di frana.* Atti 9° Conferenza Nazionale ASITA, Catania, Novembre 2005, 285-290.

Spirolazzi V., Bellingeri D., Bocci M., Zini E. (2004) - *Sviluppo di procedure operative di monitoraggio degli impatti ambientali a scala regionale: dinamica della copertura del suolo e mappatura delle esondazioni.* Atti 8° Conferenza Nazionale ASITA, Roma, Dicembre 2004, 1833-1838.

Valentini P., Bellingeri D., Colombo R., Donati R., Zanetti L. (2002) - *Classificazione del tessuto urbano tramite dati satellitari ad alta risoluzione geometrica in alcune aree della Provincia di Milano.* Atti 6° Conferenza Nazionale ASITA, Perugia, Novembre 2002.

Zini E., Bellingeri D., Menin A., Bocci M. (2003) - *Il progetto SINA Sentinel-1: uso del telerilevamento per il monitoraggio della copertura del suolo, dello stato della vegetazione e per la mappatura del manto nevoso.* Atti della Settima Conferenza Nazionale delle Agenzie Ambientali, Milano, Novembre 2003, 271-272.

Characterization of urban SAR Permanent Scatterers

Daniele Perissin and Claudio Prati

Politecnico di Milano, piazza L.da Vinci 32 - 20133 Milano. Email: perissin@elet.polimi.it

Abstract

The recently developed Permanent Scatterers (PS) technique is a processing tool in the field of space-borne SAR interferometry to detect terrain deformations with millimetre accuracy. Such accuracy is achieved in correspondence of privileged targets, the so-called Permanent Scatterers. Even if the PS technique is an operational tool since 2001, the physical nature of the PS's is still a subject of investigation. A good knowledge of the PS nature is an essential step to improve the interpretation of the measured ground deformation and to get a more precise topographic reconstruction. In this work we present the last results of the PS characterization obtained by using 120 ERS and Envisat repeated acquisitions on the urban area of Milano (Italy).
Keywords: SAR interferometry, Permanent Scatterers, target recognition, data fusion, urban monitoring

Riassunto

La tecnica dei diffusori permanenti (Permanent Scatterers, PS) è un'applicazione di punta nel contesto dell'interferometria SAR satellitare, in grado di monitorare fenomeni di deformazione con accuratezza millimetrica tramite l'osservazione di un limitato numero di punti di misura (i PS). Nonostante la tecnica PS sia uno strumento operativo già da alcuni anni, la natura fisica dei punti di misura osservati dal satellite è tutt'oggi oggetto di investigazione. La conoscenza della natura fisica dei PS è un passo fondamentale nell'interpretazione dei fenomeni di deformazione e per una corretta ricostruzione della topografia. Scopo del presente lavoro è mostrare i risultati della caratterizzazione dei PS, ottenuti utilizzando 120 immagini acquisite dai satelliti ERS ed Envisat della zona urbana della città di Milano.
Parole chiave: *Interferometria SAR, diffusori permanenti, riconoscimento di bersagli, fusione di dati, monitoraggio urbano*

Introduction

The Permanent Scatterers (PS) technique is a powerful operational tool for monitoring ground deformations on a large number of natural coherent targets (up to 300 PS/km^2 in urban areas), exploiting long series of SAR data [Ferretti, 2000, 2001]. The most attractive aspect of this approach is the capability of providing measurements relative to individual radar targets with unprecedented precision. Even if the PS technique has been used since the late nineties, the physical nature of PS's is still under investigation as a key step for a correct interpretation of the measured deformation mechanism. As an example, the phase of a dihedral formed by the ground and a building wall does not change in presence of

buildings slow subsidence, but it changes in case of ground subsidence [Ketelaar, 2003]. In second instance, the classification of reflecting structures behaving as PS allows an *a-prior*i identification of the PS's looking at the structural details of buildings. Finally, if we know the PS's physical nature, we can foresee their electromagnetic behaviour under different acquisition geometries, frequencies and polarizations, and we can develop feasibility studies on the integration of interferometric SAR multiple sensors (e.g. ERS and Envisat coherent exploitation [Colesanti, 2003; Ferretti, 2004] or the future Radarsat 1 and Radarsat 2 coherent exploitation). In this paper we describe the methodology adopted to tackle the problem of the urban PS physical nature and we report the principal results we obtained.

Physical analysis

The present work is based on the analysis of 120 SAR images of town of Milano where ground truth data are easily accessible to us. The 120 SAR images dataset has been acquired by ERS-1, ERS-2 and Envisat satellites from 1992 to 2005. Normal baseline values range from -4000 to 4000 m and Doppler centroid from -4 to 4 PRF (such a wide DC range is mainly due to ERS-2 acquisitions in gyro-less mode). Moreover, two 16 MHz spectral bands centered around 5.3 GHz (ERS radar frequency) and 5.331GHz (Envisat radar frequency) have been exploited. The processed area covers 16x18 km² around the city-center. Four different measurements have been carried out for each PS: the elevation with respect to the ground, the radiation pattern, the auto-interferogram phase of an Envisat alternating polarization acquisition and the phase dependence on the air temperature measured at the SAR acquisition time.

Elevation

The PS location should be known within a few meters accuracy in the 3D space to be able to associate the PS to a physical structure. To this aim we exploit the PS relative height that, together with the deformation rate, is the principal product of the PS analysis. The PS approach is described in detail in [Ferretti, 2000, 2001].

Here, we wish briefly recall the link between phase and height for a PS, that allows to precisely estimate its position on the ground. For a given PS with slant range position and elevation respectively Δr and Δq (relative to the center of the sampling cell), the following expression of the geometric component of the interferometric phase holds:

$$\Delta\phi = \frac{4\pi}{\lambda}\left(\Delta r \frac{B_n}{R_M \tan\theta} + \Delta q \frac{B_n}{R_M \sin\theta}\right) \qquad [1]$$

Here λ is the radar wavelength, B_n the normal baseline, R_M the sensor-target distance and θ the incidence angle. The first term is related to the flat terrain and can be compensated exploiting the WGS84 ellipsoid and the satellite state vectors. The second term contains the target height, which can be estimated as the value that fits the measurement.

In Figure 1 we report the PS's ellipsoidal elevation so found along the North (Gauss-Boaga) coordinate. From Figure 1 the average 3m per km N-S slope of the area of Milano can be easily appreciated. The PS elevation referred to the surrounding ground level can be achieved by estimating and subtracting the lower envelope of the cloud of points in Figure 1. The result obtained is shown in Figure 2. Focusing the attention on details, one can appreciate some set of adjacent points with high elevations, describing high regular structures. It is worth noting the thickening of high points around the center of Milan, where the buildings are higher and closer among themselves.

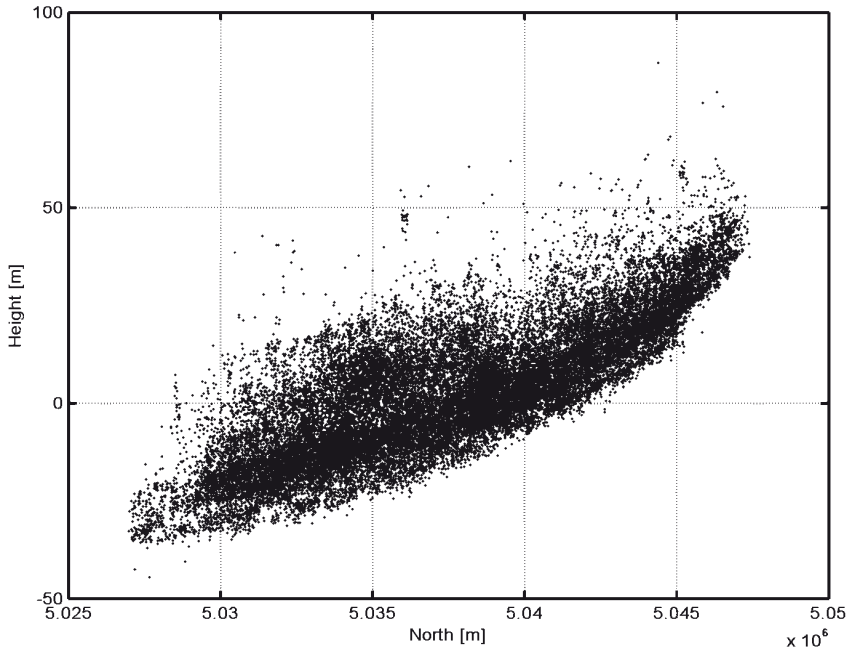We wish to point out that such a precision of PS height estimate is due to the high disper-

Figure 1 - PS estimated elevations as a function of the North (Gauss-Boaga) coordinate in Milan. Average slope in the order of 3 m per km.
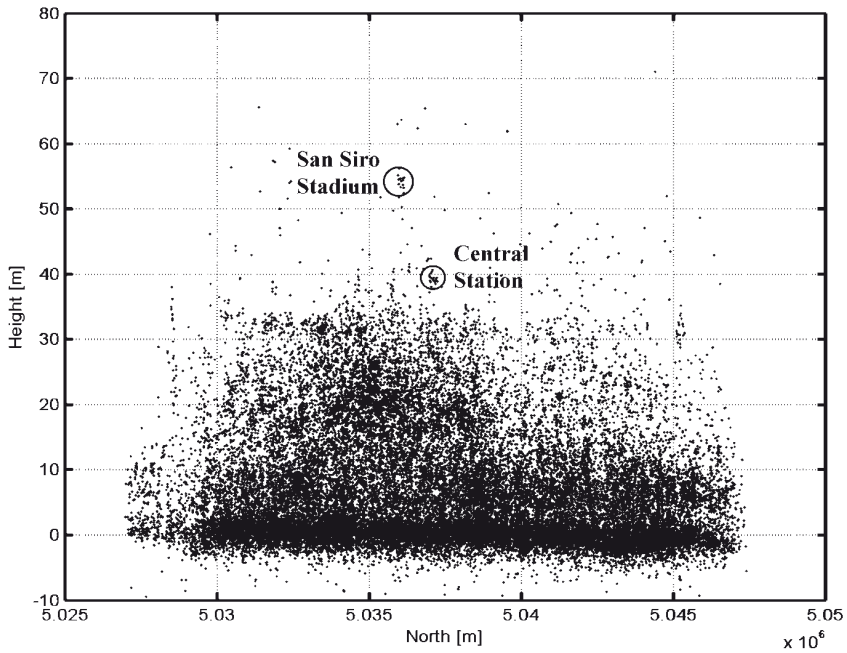

Figure 2 – North-South profile of Milan city after removing for the low-pass topography. It is worth noting the thickening of high points around the centre of Milan, where the buildings are higher and closer among themselves. Focusing the attention on details, some set of adjacent points with high elevations describing high regular structures can be appreciated, e.g. the Central Station and San Siro Stadium.

sion of normal baseline values, ranging from -4000 to 4000 m. With such a dataset, despite of the presence of a few outliers showing strong negative elevation, the achieved average elevation accuracy is close to 1 m [Perissin, 2005].

Amplitude analysis

The identification of each PS backscattering pattern as a function of normal baseline and Doppler centroid is the second step of the PS's characterization. The amplitude variations as a function of the look angle (normal baseline and Doppler centroid) can be ascribed to the physical dimensions of the scattering object. In fact, whereas a point-wise scatterer is expected to show a RCS independent of the acquisition geometry, an extended target can exhibit a very complex behavior. In our discussion, we consider a very simple model for the target: a flat surface (*i.e.* a mirror) in a low-clutter environment. In this way, we assign to the scatterer the size of an equivalent mirror with the same amplitude variations. It should be pointed out that ERS-2 loss of gyroscopes, usually seen as a negative fact, turns out to be a very positive circumstance to get the microwave radiation pattern of each scatterer also in the azimuth direction.

The PS backscattering radiation pattern has been modeled with a cardinal sine both in range and azimuth domains. Each PS is thus identified by 4 parameters: width and orientation in range and azimuth directions. As far as range is concerned, the PS backscattering radiation pattern observed by the satellite as a function of the normal baseline B_n is a cardinal sine whose main lobe width is inversely proportional to the target extension L_x measured along the normal to the slant range. The main lobe position B_{n0} on the normal baseline axis indicates the target pointing.

$$s(B_n) = \mathrm{sinc}\left[\frac{2L_x}{\lambda R_M}(B_n - B_{n0})\right] \qquad [2]$$

Likewise we obtain for the azimuth dimension a backscattering radiation pattern as a function of the Doppler centroid variation with respect to the master image Δf_{DC}:

$$s(\Delta f_{DC}) = \mathrm{sinc}\left[\frac{L_{az}}{PRF\delta_{az}}(\Delta f_{DC} - \Delta f_{DC0})\right] \qquad [3]$$

Here *PRF* is the pulse repetition frequency and δ_{az} the azimuth sampling step.

In Figures 3 the results of the estimated PS azimuth dimensions are shown. The gray scale of Figure 3 indicates the PS's density in Milano as a function of the estimated PS's azimuth extension (x-axis) and PS azimuth orientation (y-axis). The azimuth orientation is expressed as the normalized Doppler centroid (Hz/PRF) deviation with respect to the master image, which is barycentric within the dataset. Figure 3 shows that large coherently observed PS's (on the right of the image) are mainly pointed toward the master acquisition since their radiation pattern is narrow.

On the other hand, narrow PS's (on the left of the image) do not show such a strict pointing requirement since their radiation pattern is wider. On the same image it can be observed that some of the PS's are seen through their secondary lobes that are separated by the main lobe by an angle (vertical on the image) that is inversely proportional to the PS azimuth dimension. In between there are the zeros of the radiation pattern that generate null density areas clustering along curves clearly visible in Figure 3. It should be pointed out that PS azimuth dimensions larger than the resolution cell (about 5 meters for ERS and Envisat) can be detected.
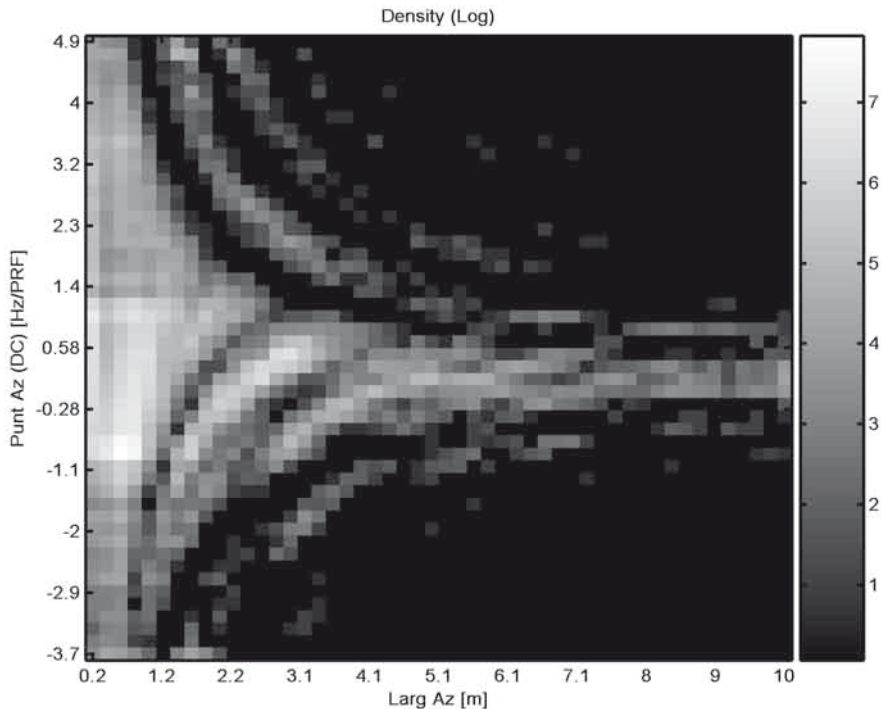
Figure 3 - PS's azimuth geometric conformation (Milan dataset). Gray scale indicates the density of PS's in a log scale. Y-axis: PS's orientation as a function of normalized Doppler centroid [Hz/PRF]. X-axis: PS's azimuth extension [m].

Narrow PS's with a wide scattering pattern should remain coherent when observed from different acquisition geometries. A PS with the very same 3D location in images acquired with different looking angle is reported in Figure 4. Here, data acquired from 2 different ERS and Envisat parallel tracks (208 and 480) with 3° incidence angle difference are plotted together, showing very high coherence.

From a technical point of view it should be emphasized that images co-registration is much more critical when working on amplitudes than on phases of interferometric images. In the case of ERS and Envisat SAR data, coregistration errors as small as 50 cm should be achieved to get useful information from amplitudes time series.

Alternating Polarization

In the alternating polarization acquisition mode, Envisat takes simultaneously 2 images with 2 different polarizations of the same area, with the same acquisition geometry but with half azimuth resolution. Creating an interferogram between the two images (auto-interferogram), in correspondence "good" scatterers (where the 2 different spectra are coherent) the interferometric phase depends only on the polarimetric response of the scatterers [Inglada, 2004]. Thus the polarimetric auto-interferogram can be exploited for discerning between odd and even bounces.

A specular reflector (a mirror) behaves in the same way if illuminated with horizontal or vertical polarized signals (0 auto-interferometric phase), whereas a dihedral rotates the phase by π radians [Van Zyl, 1989; Inglada, 2004].
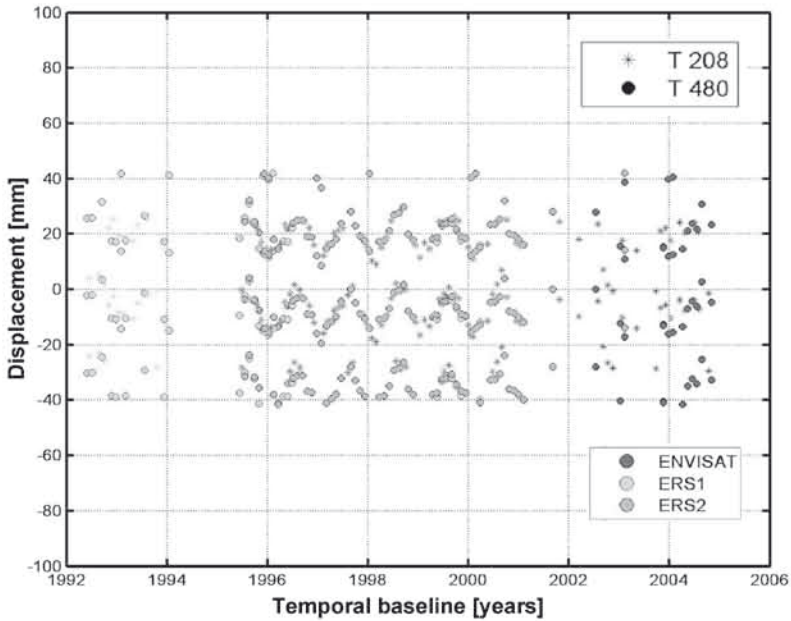
Figure 4 - An example of displacement time series [mm] measured by ERS and Envisat from 2 different parallel tracks 40 km apart. Stars: track 208, circles: track 480.
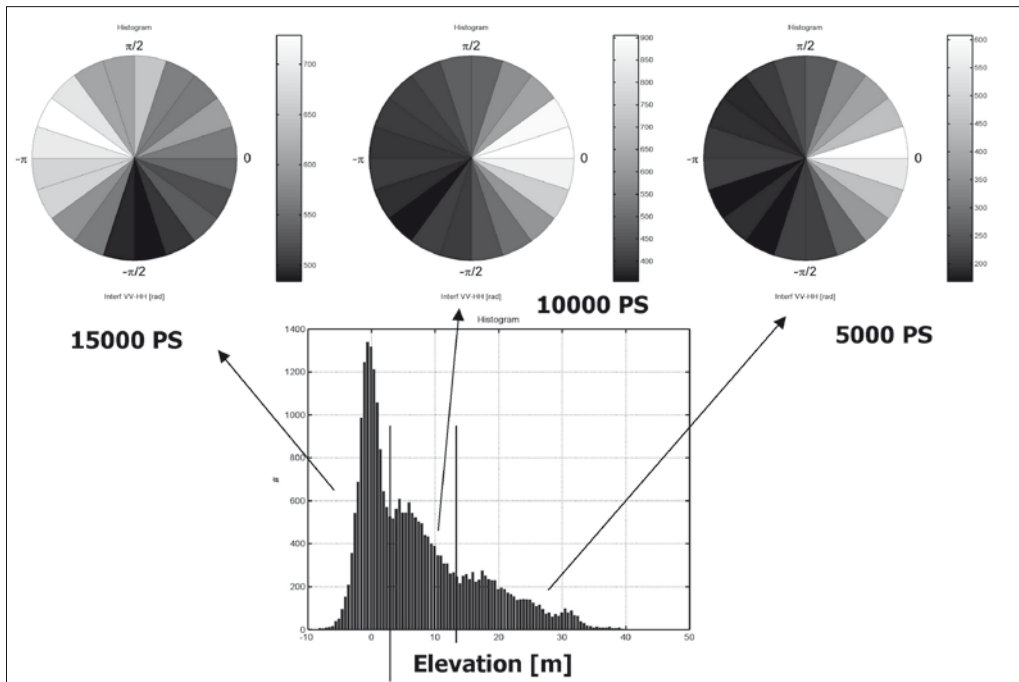

Figure 5 - Alt. Pol. auto-interferogram phase [rad] histograms for different elevation classes. Below: PS's elevation [m] histogram.

In Figure 5 three histograms of the auto-interferometric phase are shown for different elevation classes of the PS's in Milan. It's interesting to observe that the probability to have dihedrals at the ground level is quite high, while at higher elevations odd-bounces dominate (tiled roofs or corrugated iron roofs are good back-scatterers).

Temperatures

The last element taken into account is the correlation between the PS phase time series and temperatures taken at the acquisition time. This measurement does not refer to the target itself, but to the structure on which it lays. In fact, the phase oscillations are normally due to the thermal dilation of high composite steel-concrete buildings. The formula of linear expansion of a solid is

$$\Delta L = \alpha L_0 \Delta T \qquad [4]$$

A change in temperature ΔT causes a dilation of ΔL for an object of length L_0. The constant of proportionality α is called the coefficient of linear expansion and depends on the material. Assuming a thermal expansion coefficient of $1 \cdot 10^{-5}$ (composite steel concrete buildings) and a temperature range of 30°C, a 24 mm oscillation corresponds to an 80 m high building. This is the case depicted in Figure 6 where an example of displacement time series before and after the subtraction of the temperature-dependent term is shown. The oscillation range is thus related to the building height, as can be seen in Figure 7. The PS's thermal dilation is plotted in correspondence of their elevation as estimated in the Milan site.
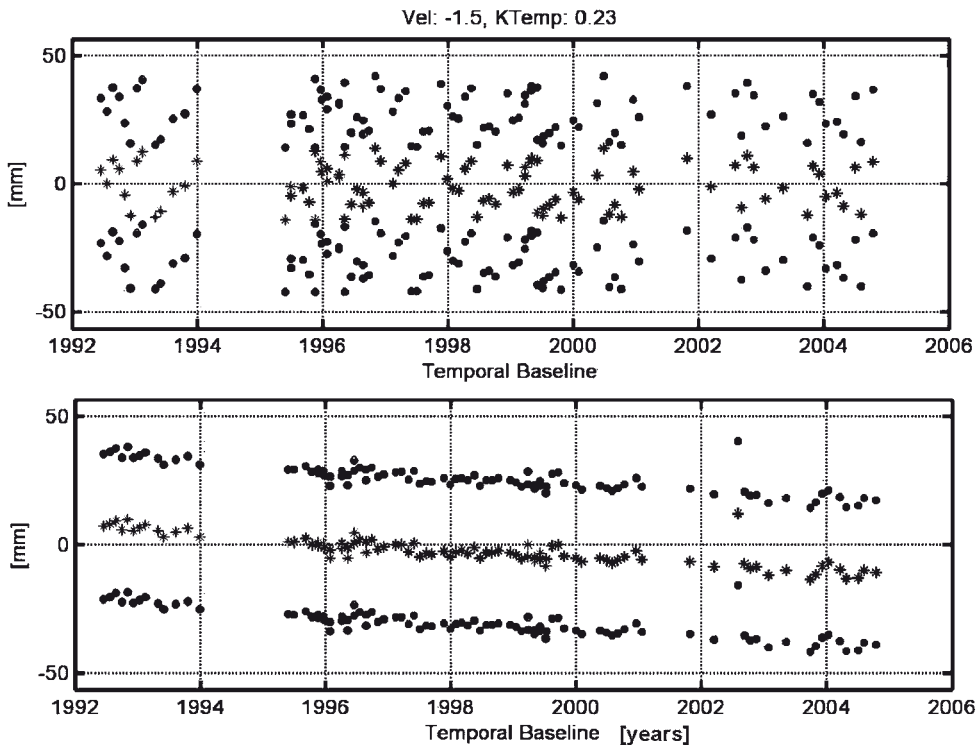

Figure 6 - Displacement time series [mm] example. Above: without removing the temperature-dependent term. Below: after removal of the temperature-dependent term. The 2 adjacent replica (± 28 mm) are plotted with dots in order to elucidate ambiguities.
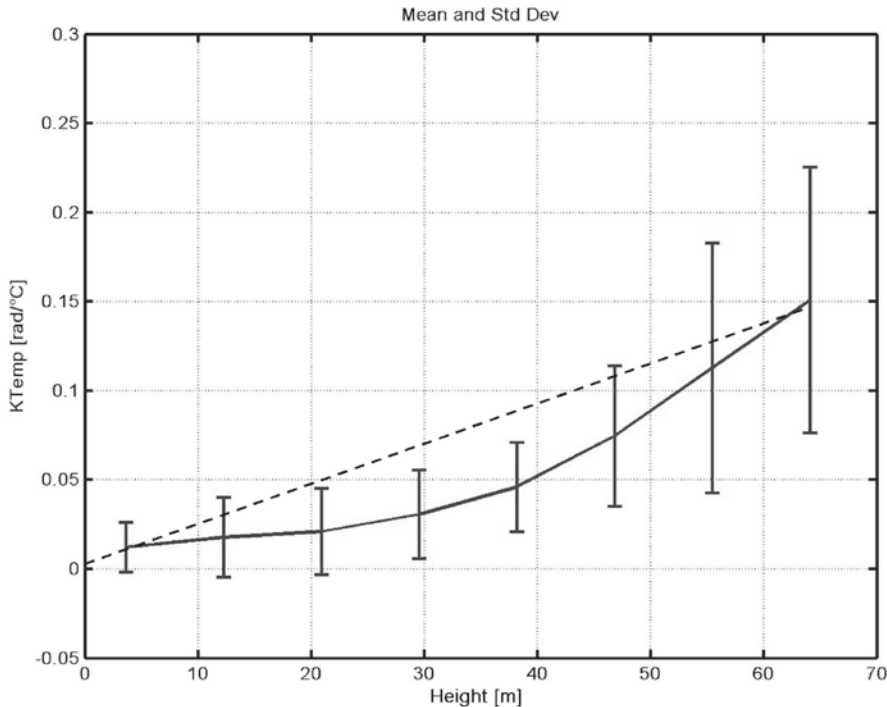
Figure 7 - Mean value and dispersion (sign at ±σ) of PS's thermal dilation as a function of the estimated elevation. Dashed line: theoretic behavior of composite-steel buildings.

As seen, the oscillating term can affect enormously the series coherence. We couldn't find structures such that reported in Figure 6 without a systematic estimation and removal of the thermal dilation component on the whole set of the analyzed points.

Target typologies

The described radar measurements can be jointly exploited to identify and characterize urban SAR PS's. Thus we discovered that the principal urban target typologies are the following:

1) Dihedrals formed by wall and ground (low elevation, narrow in range, wide in azimuth, high RCS, AP phase π), (Fig. 8). This kind of targets is visible from different parallel tracks.
2) Dihedrals with circular symmetry like poles (low elevation, narrow in range, narrow in azimuth, low RCS, AP phase π), (Fig. 9). These are targets that can be seen from ascending and descending passes.
3) Trihedrals corresponding to internal angles of courtyards (low elevation, narrow in range, narrow in azimuth, high RCS, AP phase 0), (Fig. 10). Visible from different parallel tracks.
4) Back-scattering floor gratings -periodical ground metal structures- (low elevation, wide in range, wide in azimuth, middle RCS, AP phase 0), (Fig.12). Generally not visible under different geometries.
5) Back-scattering roofs -periodical elevated structures- (high elevation, wide in range, wide in azimuth, middle-low RCS, AP phase 0), (Fig. 11). Generally not visible under different geometries.

Figure 8 - Example of structure forming a dihedral. Left: aerial photo, center: ground photo, right: estimated parameters.
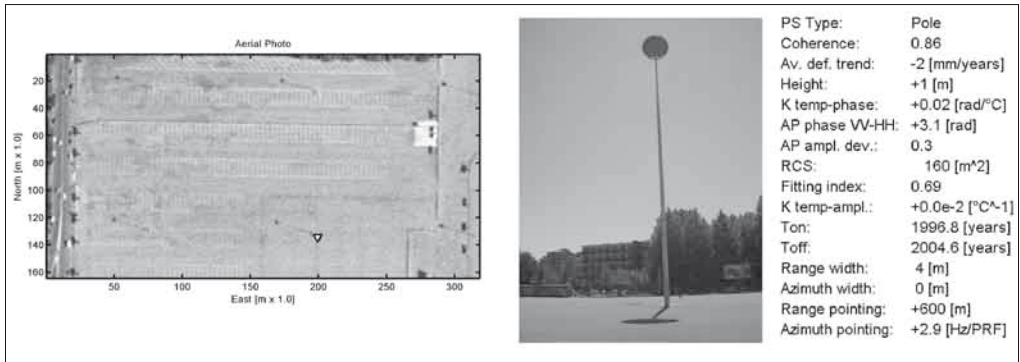

Figure 9 - Poles on a car park. Poles are dihedral targets with circular symmetry. Left: aerial photo, center: ground photo, right: estimated parameters.
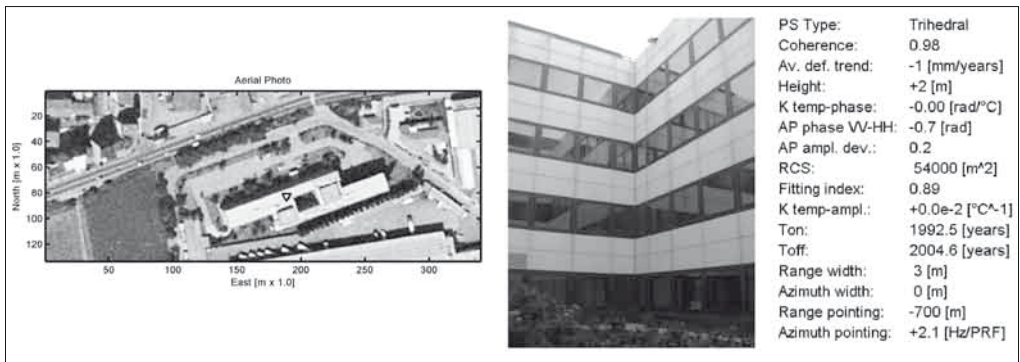

Figure 10 - Example of structure forming a trihedral. Left: aerial photo, center: ground photo, right: estimated parameters.
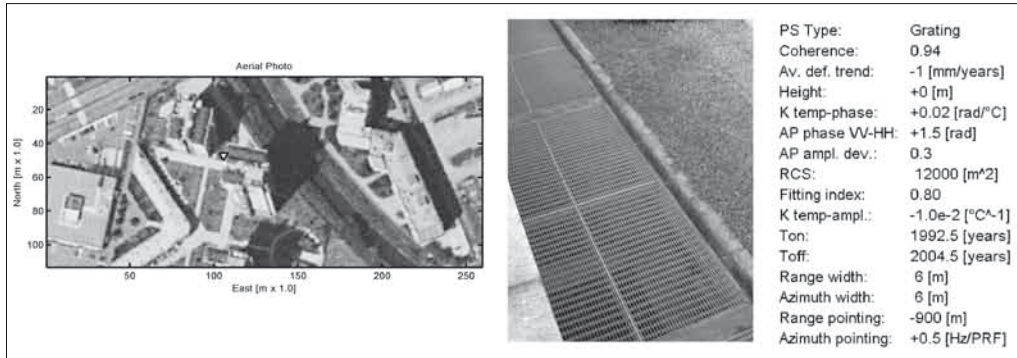
PS Type:	Grating
Coherence:	0.94
Av. def. trend:	-1 [mm/years]
Height:	+0 [m]
K temp-phase:	+0.02 [rad/°C]
AP phase VV-HH:	+1.5 [rad]
AP ampl. dev.:	0.3
RCS:	12000 [m^2]
Fitting index:	0.80
K temp-ampl.:	-1.0e-2 [°C^-1]
Ton:	1992.5 [years]
Toff:	2004.5 [years]
Range width:	6 [m]
Azimuth width:	6 [m]
Range pointing:	-900 [m]
Azimuth pointing:	+0.5 [Hz/PRF]

Figure 11 - Example of single bounce back-scatterer on the ground: floor grating. Left: aerial photo, center: ground photo, right: estimated parameters.

PS Type:	Roof
Coherence:	0.94
Av. def. trend:	-1 [mm/years]
Height:	+11 [m]
K temp-phase:	-0.01 [rad/°C]
AP phase VV-HH:	-0.3 [rad]
AP ampl. dev.:	0.2
RCS:	11000 [m^2]
Fitting index:	0.80
K temp-ampl.:	+2.2e-2 [°C^-1]
Ton:	1992.5 [years]
Toff:	2004.8 [years]
Range width:	9 [m]
Azimuth width:	2 [m]
Range pointing:	+800 [m]
Azimuth pointing:	-0.4 [Hz/PRF]
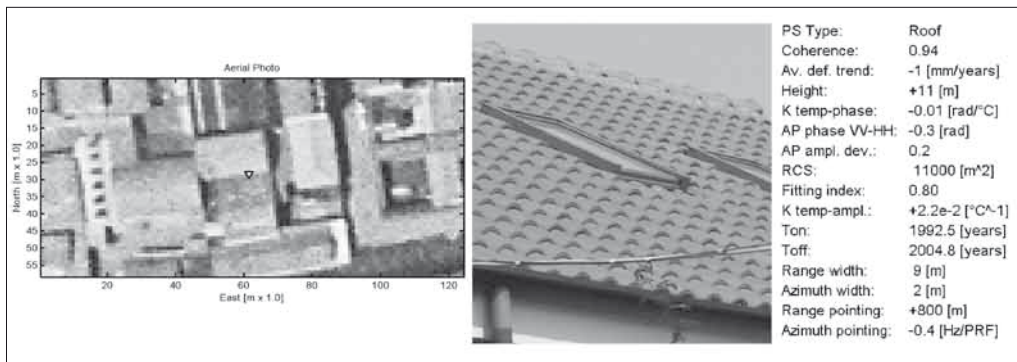
Figure 12 - Example of single bounce back-scatterer: tiled roof. Left: aerial photo, center: ground photo, right: estimated parameters.

Conclusions

In this paper we have presented the results of the first PS characterization in urban area. The 3D position of the scatterers has been estimated with a relative precision of 1m exploiting large baselines and Doppler centroids. An estimate of the PS's backscattering radiation pattern has been provided and, by means of an AP acquisition odd and even bounces of radar echoes have been discriminated. Thus, five urban SAR PS's typologies have been identified: dihedrals, poles, trihedrals, floor gratings, roofs.

Many improvements of SAR remote sensing derive from the knowledge of the physical nature of the scatterers. First, knowing which part of a structure is reflecting the radar signal allows the interpretation of the measured displacement. Then, the identification of corner reflectors makes it possible to combine data acquired by different sensors under different geometries. Consequences of this fact are the possibility of increasing the temporal sampling rate of deformation measurements and the possibility of increasing the density of targets on the ground. Thus, more accurate monitoring of deformation phenomena and more accurate elevation models can be provided. Moreover, the details achievable by means of low-resolution SAR data suggest the possibility of a combination with 3D city models for the generation of high-accurate geographic databases with constantly updated information of building deformations, also in view of the next generation high-resolution SAR missions such as TerraSAR-X or CosmoSky-Med.

References

Ferretti A., Prati C., Rocca F. (2001) - *Permanent Scatterers in SAR Interferometry*. IEEE TGARS, 39 (1), 2001.

Ferretti A., Prati C., Rocca F. (2000) - *Non-linear subsidence rate estimation using permanent scatterers in Differential SAR Interferometry*. IEEE TGARS, 38(5), 2000.

Ketelaar V.B.H., Hanssen R.F. (2003) - *Separation of different deformation regimes using PS-INSAR data*. Proceedings of FRINGE 2003, Frascati (Italy), 1-5 December 2003.

Colesanti C., Ferretti A., Perissin D., Prati C., Rocca F., (2003) - *ERS-Envisat permanent scatterers interferometry*. Proceedings of Geoscience and Remote Sensing Symposium, IGARSS '03. 2003 IEEE International, 2: 1130-1132.

Ferretti A., Perissin D., Prati C., Rocca F. (2004) - *ERS-Envisat Permanent Scatterers*. Proceedings of Geoscience and Remote Sensing Symposium IGARSS 2004, Anchorage (Alaska), September 2004.

Perissin D., Rocca F. (2005) - *Urban DEM*. Proceedings of FRINGE 2005, Frascati (Italy), 28 November - 2 December 2005.

Inglada J., Henry C., Souyris J-C. (2004) - *Assessment of ASAR/IMS Multi-polarization Images Phase Difference in the Framework of Persistent Scatterers Interferometry*. Envisat congress, Salzburg (Austria) 20-24 September 2004.

Van Zyl PJ. (1989) - *Unsupervised Classification of Scattering Behaviour using RADAR Polarimetry data*. IEEE Transactions on GRS, January 1989, 36-45.

Building height retrieval from radiometric parameters on SAR images

Giorgio Franceschetti, Raffaella Guida, Antonio Iodice, Daniele Riccio and Giuseppe Ruello

DIET, Università di Napoli Federico II, via Claudio 21 - 80125 Napoli. E-mail: rafguida@unina.it

Abstract

Urban structure detection, in terms of both geometric and electromagnetic features, from a single Synthetic Aperture Radar (SAR) image is, nowadays, an interesting still open challenge. Within this framework a new deterministic approach for the extraction of the height of an isolated building on a rough terrain is presented. The approach is based on a sound electromagnetic model which fully represents the electromagnetic return from an isolated building to an active microwave sensor, analytically evaluated in closed form. In particular, building height is extracted from double scattering contribution to the radar cross section measured on the SAR image. Some simulation examples, relative to canonical scenes, accompany and validate the proposed approach.

Keywords: Synthetic Aperture Radar (SAR), feature extraction, urban areas

Riassunto

L'estrazione di parametri, sia geometrici che elettromagnetici, da singole immagini SAR (Synthetic Aperture Radar) relative ad aree urbane rappresenta una sfida interessante tuttora aperta. In questo contesto viene presentato un nuovo approccio deterministico per il recupero dell'altezza di edifici isolati posti su suoli rugosi. L'approccio si basa su un robusto modello elettromagnetico che rappresenta completamente il ritorno elettromagnetico inviato da un edificio isolato verso un sensore attivo alle microonde e ne permette il calcolo in forma chiusa. In particolare, l'altezza degli edifici è estratta dal contributo di riflessione doppia alla sezione radar misurata sull'immagine SAR. Alcuni esempi di simulazione, relativi a scene canoniche, accompagnano e convalidano l'approccio proposto.

Parole chiave*: Radar ad Apertura Sintetica (SAR), estrazione di caratteristiche, aree urbane*

Introduction

The growth of urban centers calls for a real time monitoring able to check any change in this kind of scenario. Synthetic Aperture Radar (SAR) represents a powerful instrument allowing any weather conditions monitoring and, in particular operating modes, e.g. spotlight, very fine resolutions on data collected.

In the last years, some attempts to retrieve information on man-made objects from SAR images have been carried out. This inverse procedure can be motivated: as shown in Franceschetti et al. [2005], a set of analytical relationships among radiometric and geometric parameters of the scene and of the SAR image, can be found; it turns out that

some scene parameters could be in principle estimated from even a single SAR image.

But actually, within this framework, only in a few works [Quartulli et al., 2004] information is retrieved from single SAR images, being, in most cases, extracted from multiaspect [Bolter, 2000; Simonetto et al., 2005] or interferometric [Tison et al., 2004] SAR data and, usually, it is limited to the building dimensions estimation [Bennet et al., 2003; Bolter, 2000] or to its shape [Tison et al., 2004] from geometric parameters on the SAR image.

In most of these works, particular attention is focused on building height retrieval. In fact, range extensions of layover and shadow areas are simply related to the building height [Bennet et al., 2003; Tison et al., 2004; Franceschetti et al., 2005], so that height retrieval is immediate when the extension of these areas can be easily estimated on a SAR image. But the error affecting the measure is dependent on the SAR acquisition geometry and on the SAR image range resolution; for spaceborne SAR this approach often leads to building height estimation affected by unacceptable measurements errors.

A new way to extract height information is presented in this work.

The idea of building height retrieval from radiometric parameters measurable on SAR image is here presented. The proposed method relies on an electromagnetic model that quantifies the radar return from an isolated building on a rough terrain [Franceschetti et al., 2002; Franceschetti et al., 2003].

The model takes into account any relevant macroscopic geometrical parameters of the building [Franceschetti et al., 2002] and evaluates the corresponding radar cross section.

Single, double and triple scattering are considered as main contributions to the backscattered field [Franceschetti et al., 2002]. Moreover, multiple scattering twists together with layover and shadowing effects to form the SAR image in a not trivial way according to the geometric (building dimensions and ground roughness) and electromagnetic (complex dielectric constants of soil and building) parameters in the scene and the radar functioning mode (look angle, polarization, frequency..).

Particularly, we observed that building heights affect notably SAR image formation not only in the pixel extension of some contributions but also in their intensities.

In the following this consideration is explained in details in order to motivate our approach in building height retrieval from radiometric parameters and, particularly, from double scattering contribution to the radar cross section.

Different simulation examples relative to canonical urban scenes have been carried out letting radar parameters and scene features vary. All them proved not only the reasonableness of the methodology proposed but also its major effectiveness in many actual cases respect to height retrieval from geometric parameters. The SAR raw signal simulator adopted here [Franceschetti et al., 2003] is coherent with the scattering model considered for the feature extraction, as it takes into account all multiple reflections arising in the geometric model illustrated in the following paragraph.

In these years other simulation techniques of SAR images have been developed for urban structures, but they do not fit our idea of feature extraction because not all contributions to the radar cross section are considered. In fact, usually only layover and shadow [Soergel et al., 2003] are taken into account, or, even if double bounce is accounted for, soil roughness is ignored [Lee et al., 2001].

Geometric and electromagnetic model

Let us consider the simple urban scene represented in Figure 1. A single building, modelled as a parallelepiped with smooth roof and walls, is placed on a rough terrain. Any direction φ respect to the radar flight trajectory can be considered.

For the model adopted all main building and ground parameters are defined: the height h,

Figure 1 - Geometric model of the scene.
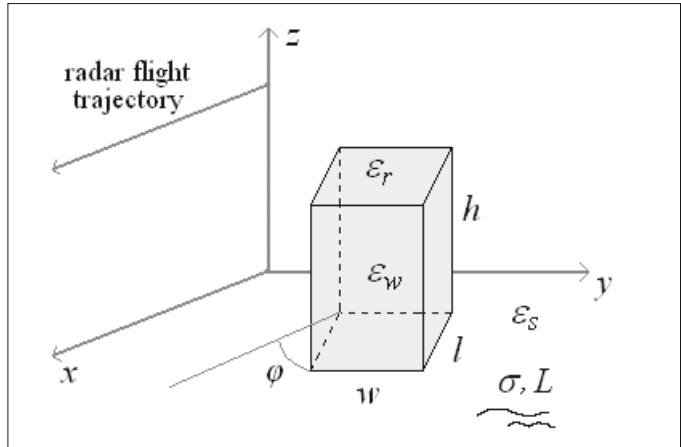
the length *l* and the width *w* of the building together with its complex dielectric constants (ε_r for the roof and ε_w for the walls); the correlation length *L* and deviation standard σ of the stochastic process describing the roughness of the soil and its complex dielectric constant ε_s.

Really, for our analysis, we do not need strictly a scene with a single building. Many buildings can be present provided that they are isolated in electromagnetic sense, *i.e.* their contributions to the (processed) SAR image do not overlap. In such a manner, our attention can be focused on each building separately from others. This hypothesis, which can be relaxed in future, is important in this work where, for the first time in literature, an attempt of retrieve geometric parameters from electromagnetic ones, measurable on the SAR image, has been lead.

In fact, as shown in Figure 2 where single, double and triple scattering have been considered, for a single building we already expect a very complex composition of different contributions on SAR image.

As far as the adopted electromagnetic model concerned, a few words are now needed.

High frequency allows us to adopt Kirchhoff approach to compute electromagnetic field backscattered towards the radar, in Geometric Optics (GO) or Physics Optics (PO) approximation according to the soil roughness [Franceschetti et al., 2002].

For the geometrical model studied, contributions till third order are demonstrated to be sufficient for a realistic description of backscattered field, [Franceschetti et al., 2002], which can be written as:

$$\begin{bmatrix} E_{Sh} \\ E_{Sv} \end{bmatrix} = jk \frac{e^{jkr}}{4\pi r} \begin{pmatrix} S_{hh} & S_{vh} \\ S_{hv} & S_{vv} \end{pmatrix} \begin{bmatrix} E_{0h} \\ E_{0v} \end{bmatrix} I_S \qquad [1]$$

where E_0 is the incident field, E_s is the backscattered field, *r* is the range distance between the target and the sensor, *h* and *v* stand for horizontal and vertical polarization, respectively, *k* is the wave number, S_{pq} is the generic element of scattering matrix, with *p* and *q* each standing for *h* or *v*, I_s is the surface integral accounting for the portion of surface invested by radiation. Complete expressions of the quantities appearing in Equation [1] are reported in Franceschetti et al. [2002].

In particular, as shown in Franceschetti et al. [2002], under the hypothesis above I_s can be written in closed form and it assumes different expressions according to the order of contri-
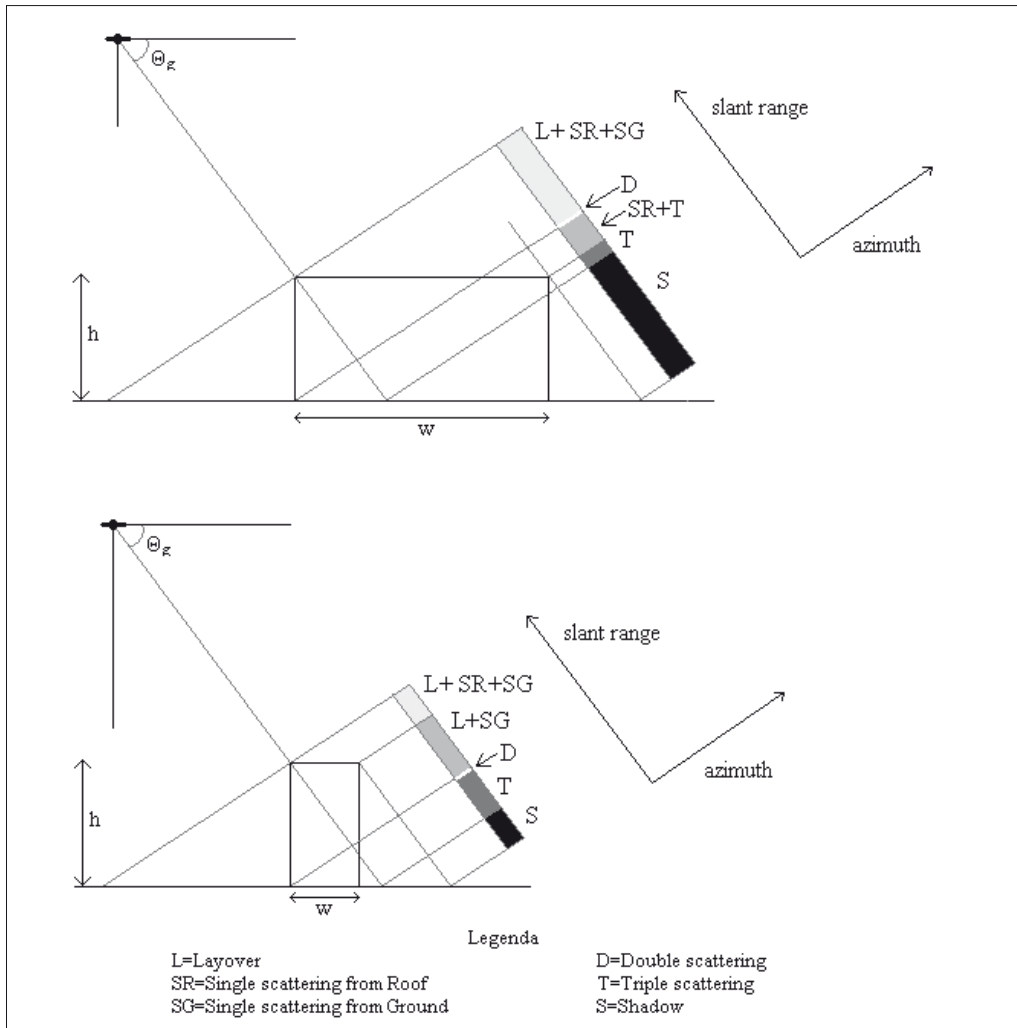
Figure 2 - Composition of different contributions on SAR image relative to a canonical scene with an isolated building.

bution (single, double and triple scattering) and the approximation (GO or PO) considered. All these forms, each in a different way, involve geometric and electromagnetic parameters previously defined to describe the scene under detection. That is why, in principle, an inversion of direct formulation in Franceschetti et al. [2002] can be thought. How this has been applied to building height is shown in the following.

Building height retrieval

As demonstrated in literature [Bennet et al., 2003], building height can be retrieved from geometric parameters measurable on SAR image, *i.e.*, layover and shadow range extensions.

Unfortunately, as shown in the next Section by means of simulation, not always these extensions can be appreciated on a real SAR image affected by speckle. Appreciating layover

extension can be difficult and also shadow area can be not meaningful for height retrieval. In fact, the extension of this area is not always directly linked to the height because, depending on the building height/width ratio, the shadow can be partly canceled by triple reflection [Franceschetti et al., 2003], see the lower part of Figure 2. Moreover, even if we are able to measure these areas, our evaluation of the building height will be always affected by an error linked to the range resolution of the SAR image.

So, when SAR image resolution is not very high or when building height can not be retrieved from layover and shadow, an alternative approach is worth to be studied and it is what we present in this paper.

Starting from Franceschetti et al. [2005] and Franceschetti et al. [2002] we found that building height involves single reflection from wall, double reflection and triple reflection. But triple scattering, the contribution of which has been emphasized in Figure 2, is weak and difficult to be extracted; single reflection from wall (layover) is usually mixed with single scattering from roof and from ground and so not immediately available; double reflection, instead, is always easily distinguishable for its peaked value. Then, a building height retrieval from double scattering contribution can be attempted.

Now, let us suppose that, for roughness parameters involved, Geometric Optics (GO) can represent a reasonable approximation for both bounces of double scattering. This is the case, for example, of a building with a garden in front, whatever is the working frequency in the microwave range. But if the building is placed on a bare soil, it will appear rough in the Ka band and smooth in the L one [Xia et al., 1997]; that is why the same approach with different approximations has to be adopted according to the surface roughness.

In the hypothesis above, the link between the building height and the integral surface I_s found in Franceschetti et al. [2002] can be inverted giving

$$h = \frac{\left\langle I_S \cdot I^*_S \right\rangle}{l \tan \vartheta \cos \varphi \, \dfrac{1 + \tan^2 \vartheta \sin^2 \varphi}{4k^2 \cos^2 \vartheta \cdot 2\pi\sigma^2 \left| C''(0) \right|} \exp\left[-\dfrac{\tan^2 \vartheta \sin^2 \varphi}{2\sigma^2 \left| C''(0) \right|} \right]} \qquad [2]$$

where ϑ is the radar look angle, $C''(\cdot)$ is the second derivative of normalized correlation function of stochastic process describing the microscopic profile of ground and $< I_s \cdot I^*_s >$ represents the mean square value of I_s.

In Equation [2] the building height can be expressed in terms of the radar and scene parameters. On one hand, this shows the generality of the retrieval approach according to which other interesting parameters can be extracted; on the other hand, it means that a high a priori knowledge of ground truth as well as of radar parameters is needed for the retrieval of only one unknown.

Now, what we measure on the SAR image is the radar cross section RCS linked to the backscattered field, and hence to the surface integral I_s, by the well known expression:

$$RCS = \frac{4\pi r^2 < \left| E_s \right|^2 >}{\left| E_o \right|^2} \qquad [3]$$

Equations [1], [2], [3] have been used in the next section in evaluating building height after having measured RCS relative to double scattering on the SAR image.

Some considerations are now in order. As anticipated, a high a priori knowledge of the scene is needed. In the simulation examples we will suppose each parameter describing the scene, except the height, to be known but actually some of them can be extracted from the image itself. In particular, l and φ can be evaluated in a very simple way by means of geometric considerations.

Moreover, being SAR image not calibrated, we need the presence of two buildings with known height to compute the two unknown calibration constants. Note that in a more general case, in a scene with n buildings, the height of only two of them has to be known to evaluate the heights of the remaining $n-2$.

Many simulation examples have been realized letting radar and scene parameters vary. Some of them, presented in the follow, are accompanied by interesting results showing the efficiency of the approach adopted.

Simulation examples

The urban canonical scene simulated in the next examples is represented by three buildings aligned along a direction in general not parallel with the radar trajectory flight. As anticipated, all geometric and electromagnetic parameters in the scene are assumed to be known except for the height of the central building that we propose to retrieve. We let these parameters, as well as radar ones, vary.

Double reflection is always easily distinguishable, and so extractable, on SAR image.

In fact, see Figure 3, if we plot a range cut of the amplitude $|E_s|$ of the field backscattered by the central building, we realize that every contribution can be recognized only in absence of speckle. For example, in Figure 3a, we first distinguish the backscattering from ground and then the different contributions from the building (in order we have layover, double reflection, backscattering from roof and shadow) But when speckle is present, see Figure 3b, this operation becomes critical for most contributions. Only double scattering remains particularly peaked in the plot.

Moreover, the error on the hight retrieved by the double reflection is always independent of SAR range resolution and the height evaluation is often better than that retrieved from geometrical parameters.

An example is given for the simulated SAR image in Figure 4 relative to $\varphi=0°$ and in presence of speckle. Horizontal polarization has been considered both in transmitting and receiving mode. Radar parameters adopted are relative to a hypothetic, but not really existing, airborne sensor functioning in L-band with a look angle of 30 degrees.

Scene parameters are synthesized in Table 1. The heights considered are relative to buildings of about 3, 6 and 9 floors.

Length and width dimensions are not typical of buildings in urban centres but they have been chosen so large in order to compare our method with height extraction from shadow. For the sake of simplicity we have supposed the buildings having the same dielectric constants, but a different electromagnetic behaviour can be considered for each of them. The hypothesis of rough soil is true in L band, according to the Rayleigh criterion, only for some kinds of surfaces (like grass or bushes) with the given look angle [Xia et al. 1997], but also this assumption can be generalized taking into account smooth grounds and, consequently, the appropriate scattering model. We realize from the last row in Table 1 that the height estimation error is about 0.09 m.

By means of a range cut of simulated SAR image around the central building, a shadow area of 4 pixels in slant range has been measured. Considering SAR resolution and look angle, a central building height of 16.76 m can be retrieved from shadow, so with an error of 3.24 m.

A more realistic instance has been considered in Figure 5, in which a wall direction of 30°
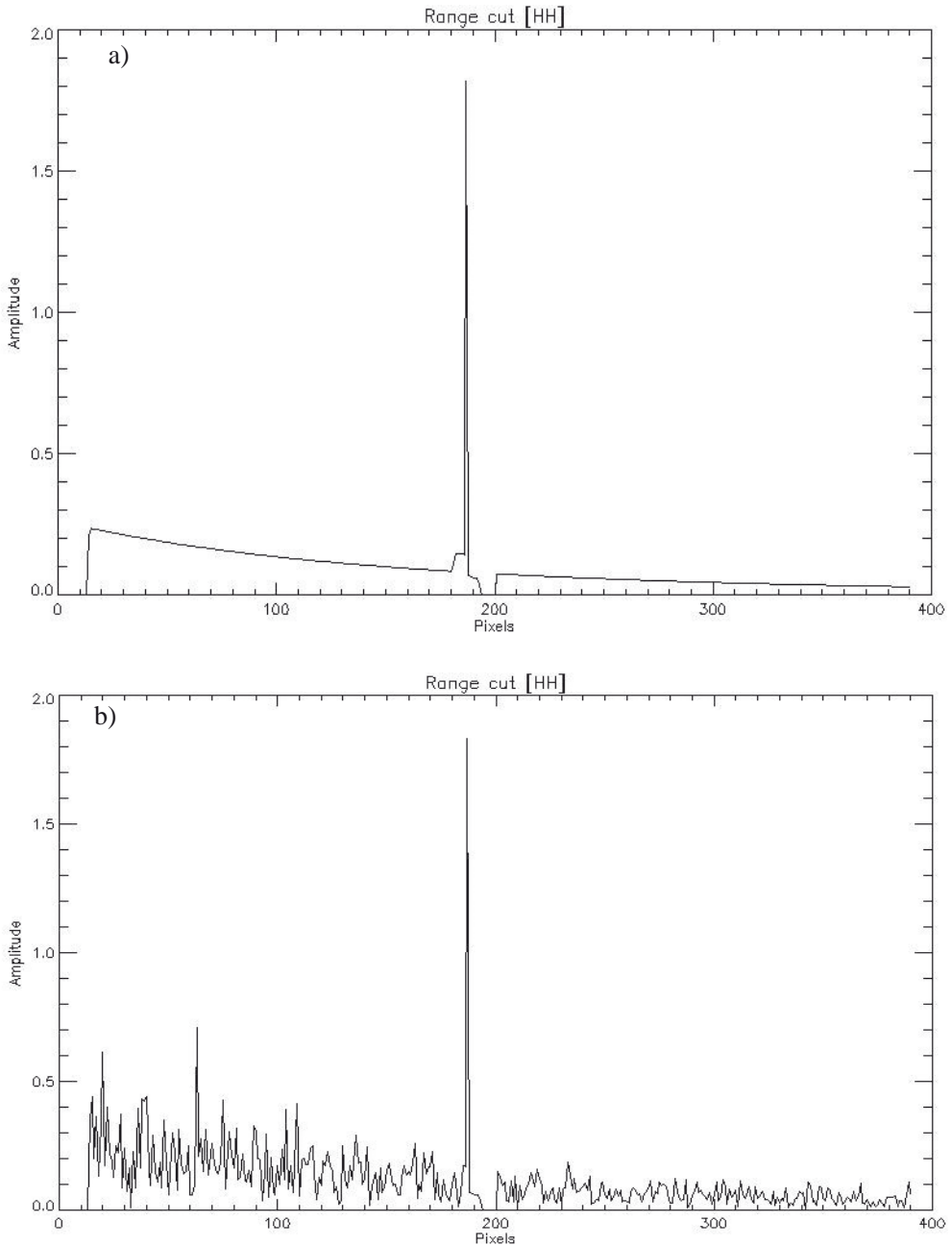
Figure 3 - Range cut of the amplitude |E$_s$| backscattered by the central building: (a) in absence of speckle; (b) in presence of speckle.

respect to the SAR flight trajectory has been simulated. The difference in building heights (3 metres) is also smaller than in the previous example as probably happens in real scenes. Most of other parameters remain unchanged, as summarised in Table 2.
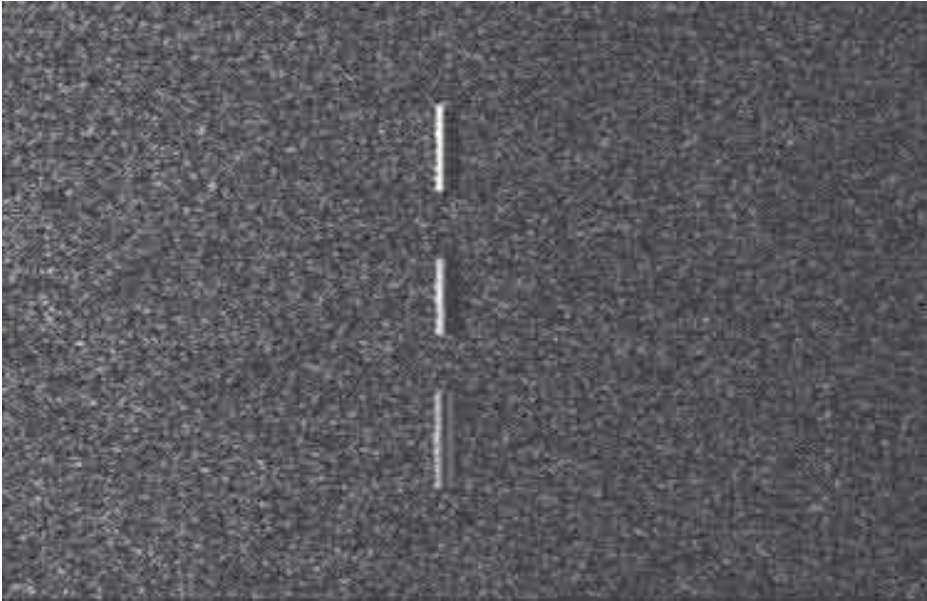
Figure 4 - Simulated SAR image relative to three buildings aligned along the direction φ=0°.

Table 1 - Scene parameters relative to the simulated SAR image in Figure 4.

Top building dimensions (length x width x height)	90 m x 90 m x 30 m
Central building dimensions (length x width x height)	80 m x 80 m x 20 m
Bottom building dimensions (length x width x height)	100 m x 100 m x10 m
Roof and wall dielectric constant	3
Roof and wall conductivity	0.01 S/m
Ground dielectric constant	4
Ground conductivity	0.001 S/m
Ground standard deviation	0.19 m
Ground correlation length	1.54 m
Image resolution (range x azimuth)	4.839 m x 2.571 m
Central building height estimation	19.91 m

In this case we also tried to improve height estimation from shadow by measuring the extension of this area with more range cuts and by operating a mean of all measured pixel extensions.

In this way we found for the shadow area an extension of 4.375 pixels that corresponds to a height of 18.33 m and an error of 4.67 m. Instead, by applying deterministic extraction from double reflection (last row in Table 2) we find that the building height is retrieved with an error of 1.78 m. In all of the other performed simulations, the error is even smaller, often inferior to one meter.
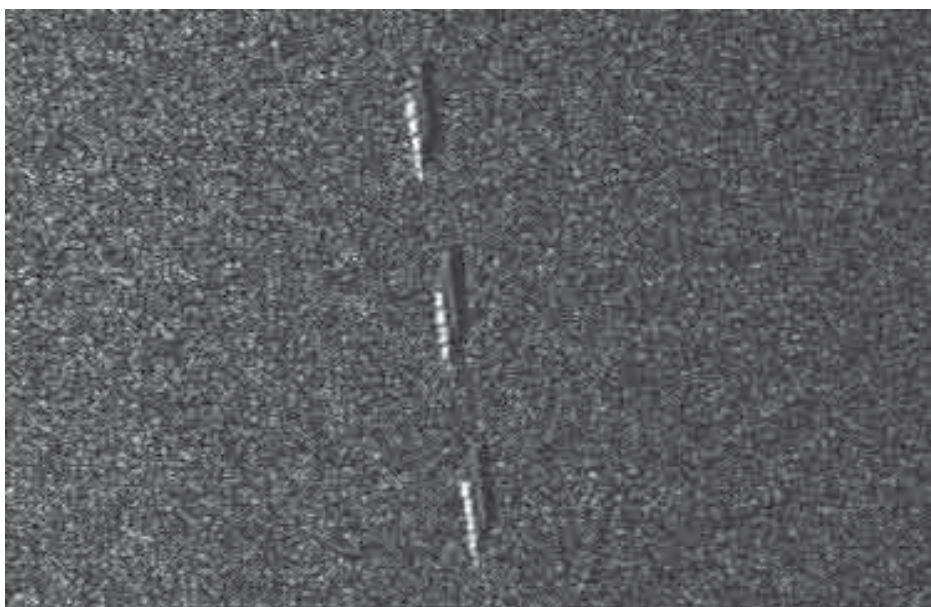
Figure 5 - Simulated SAR image relative to three buildings aligned along the direction φ=30°.

Table 2 - Scene parameters relative to the simulated SAR image in Figure 5.

Buildings length and width	100 m x 100 m
Buildings height	20,23,26 m
Roof and wall dielectric constant	3
Roof and wall conductivity	0.01 S/m
Ground dielectric constant	4
Ground conductivity	0.001 S/m
Ground standard deviation	0.19 m
Ground correlation length	1.54 m
Image resolution (range x azimuth)	4.839 m x 2.571 m
Central building height estimation	21.22 m

Conclusions

The need of not conventional approaches to retrieve geometrical features from single SAR image has been highlighted. Particularly, building height retrieval from radiometric parameters, such as intensity of double reflection region, has been described in details.

The suggested approach has been applied to simulated canonical scenes with a few buildings. It results to be efficient, being the measure independent of SAR resolution image, and the obtained first results encourage application to real data.

At the moment, the main limitation of our method is that it does not take into account mutual interactions among different buildings in the scene. Inclusion of this effect is currently under study.

References

Bennett A.J., .Blacknell D. (2003) - *The Extraction of Building Dimensions from High Resolution SAR Imagery.* Proc. of the International Radar Conference 2003, 182-187.

Bolter R. (2000) - *Reconstruction of Man-Made Objects from High Resolution SAR Images*. IEEE Aerospace Conference Proceedings, 3: 287-292.

Franceschetti G., Iodice A., Riccio D. (2002) - A *Canonical Problem in Electromagnetic Backscattering from Buildings*. IEEE Trans. Geosci. Remote Sensing, 40: 1787-1801.

Franceschetti G., Iodice A., Riccio D., Ruello G. (2003) - *SAR Raw Signal Simulation for Urban Structures*. IEEE Trans. Geosci. Remote Sensing, 41: 1986-1995.

Franceschetti G., Guida R., .Iodice A, .Riccio D, Ruello G. (2005) - *Deterministic Extraction of Building Parameters from High Resolution SAR Images*. Proceedings of the 3rd RSS/ISPRS joint Symposium on Remote Sensing and Data Fusion over Urban Areas, Tempe (Arizona, USA), .

Lee W.K. (2001) - *Analytical investigation of urban SAR features having a group of corner reflectors*. In Proc. IGARSS, 3: 1282-1284.

Quartulli M., Datcu M. (2004) - *Stochastic Geometrical Modeling for Built-Up Area Understanding from a Single SAR Intensity Image with Meter Resolution*. IEEE Trans. Geosci. Remote Sensing, 42: 1996-2003.

Simonetto E., Oriot H., Garello R. (2005) - *Rectangular Building Extraction From Stereoscopic Airborne Radar Images*. *I*EEE Trans. Geosc. Remote Sensing, 43: 2386-2395.

Soergel U., Schulz K., Thoennessen U., Stilla U. (2003) - *Determination of optimal SAR illumination aspects in built-up areas*. In Proc. IGARSS, 6: 3362-3364.

Tison C., Tupin F., Maitre H. (2004) - *Retrieval of building shapes from shadows in high resolution SAR interferometric images*. In Proc. IGARSS, 4: 1788-1791.

Xia Z., Henderson F.M. (1997) - *Understanding the Relationships Between Radar Response Patterns and the Bio- and Geophysical Parameters of Urban Areas.* IEEE Trans. Geosci. Remote Sensing, 35: 93-101.

Abstracts di lavori di Autori italiani pubblicati su riviste internazionali

Monthly averages of sea surface temperature

Pellegrini P.F.[1], Bucci M.[2], Tommasini M.[1], Innocenti M.[3]
[1]DET, Università degli Studi di Firenze, Via S. Marta 3, 50139 Florence. Italy
[2]ARPAT. Via Adige 12, 57025 Piombino (LI). Italy
[3]PIN. Piazza G. Ciardi 25, 59100 Prato (PO). Italy

This paper concerns the time variation in mean sea surface temperature measurements on a regional scale by using AVHRR data. The studied algorithm uses sub-pixel resolution, precise geolocation and determination of the cloudy pixels. In order to indicate cloudy pixels, thresholds based on regional temperature maps are applied instead of the average temperatures of the Mediterranean Sea. Special calculations have been made for coastline pixels. The zone considered is the sea off the Tuscan region of Italy.

Integration of multi-source NDVI data for the estimation of Mediterranean forest productivity

Maselli F., Chiesi M.
IBIMET-CNR. 50144 Firenze. Italy

This paper presents the development and testing of different integration procedures aimed at producing Normalized Difference Vegetation Index (NDVI) datasets with high spatial and temporal resolutions. In particular, two methods were considered, which both used higher spatial resolution information to increase the spatial detail of more frequent low resolution NDVI data. The first method was based on the extraction of per-class NDVI end-member values from low spatial resolution images (NOAA-AVHRR), followed by a combination of these values with a reference land cover map. Starting from the same end-members, the second method introduced further high resolution information by means of regression analyses applied per-pixel to the multitemporal dataset. The performances of the two methods were evaluated by means of two experiments carried out in a Mediterranean study area (San Rossore, central Italy). First, the images produced were compared on a per-pixel basis to higher spatial resolution Landsat TM/ETM+ data. Next, the NDVI temporal

profiles were transformed into Fraction of Absorbed Photosynthetically Active Radiation (FAPAR) estimates, which were combined with standard meteorological (radiation) data to compute forest Gross Primary Productivity (GPP). The validation of these GPP estimates was performed by comparison with the outputs of a more complex model of bio-geochemical processes (FOREST-BGC), already calibrated in the study area. The results of both tests indicated the greater accuracy of the more advanced per-pixel integration method, which was capable of reproducing NDVI data with high spatial and temporal details.

Space-borne and ground-based SAR interferometry as tools for landslide hazard management in civil protection

Corsini A.[1], Farina P.[2], Antonello G.[3], Barbieri M.[1], Casagli N.[2], Coren F.[3], Guerri L.[2], Ronchetti F.[1], Sterzai P.[3], Tarchi D.[4]

[1]Università di Modena e Reggio Emilia, Dip. di Scienze della Terra, Largo S. Eutemia19, 41100 Modena. Italy
[2]Università di Firenze, Dip. di Scienze della Terra. Via G. La Pira 4, 50121 Firenze, Italy
[3]Istituto Nazionale di Oceanografia e Geofisica Sperimentale OGS, Dipartimento di Geofisica della Litosfera, Borgo Grotta Gigante 42/C. 34010 Sgonico (Trieste), Italy
[4]Joint Research Centre, European Commission. 21020 Ispra. (Varese), Italy

In recent years, SAR interferometry has become one of the most popular emerging techniques for the assessment of ground displacements, and, as such, it is of great interest as a possible operational tool for civil protection institutions having to deal with landslide risk. The paper presents some of the results obtained in northern Italy during a research project aimed at testing the potentiality of the application of C-band space-borne interferometry and Ku-band ground based interferometry during different specific civil protection activities. Main research objectives were the detection of the movements of complex earth and rock slides affecting built-up areas during the 1990s, and the near real-time monitoring of a reactivated rotational earth slide over an emergency period of 15 days. Results of space-borne interferometry did qualitatively fit with the geological interpretation of the mass movements and with ground truths such as damaged buildings and in situ monitoring systems. However, this was not achieved in quantitative terms, suggesting that this technique should be used limitedly for displacement recognition and not monitoring. On the other hand, ground-based interferometry proved valuable both for a qualitative and a quantitative estimate of slope movements. Nonetheless, the research has also enabled the limitations that are still to be tackled in order to bring these systems to an operational usage in civil protection to be highlighted.

PAN-sharpening of very high resolution multispectral images using genetic algorithms

Garzelli A., Nencini F.

Department of Information Engineering, University of Siena, 53100 Siena, Italy

A novel image fusion method is presented, suitable for sharpening of multispectral (MS) images by means of a panchromatic (PAN) observation. The method is based on redundant

multiresolution analysis (MRA); the MS bands expanded to the finer scale of the PAN band are sharpened by adding the spatial details from the MRA representation of the PAN data. As a direct, unconditioned injection of PAN details gives unsatisfactory results, a new injection model is proposed that provides the optimum injection by maximizing a global quality index of the fused product. To this aim, a real-valued genetic algorithm (GA) has been defined and tested on Quickbird data. The optimum GA injection is driven by an index function capable of measuring different types of possible distortions in the fused images. Fusion tests are carried out on spatially degraded data to objectively compare the proposed scheme to the most promising state-of-the-art image fusion methods, and on full-resolution image data to visually assess the performance of the proposed genetic image fusion method.

Discriminating urban environments using multiscale texture and multiple SAR images

Dell'Acqua F., Gamba P.
Dipartimento di Elettronica, Università di Pavia. 1-27100 Pavia. Italy

The use of multiscale textural features for urban satellite Synthetic Aperture Radar (SAR) image characterization is introduced. The multiscale nature of urban environments requires that no single scale of analysis is exclusively considered. An accurate texture-based discrimination of land use/land cover classes needs, for instance, the computation of multiscale textural features for a wide range of parameters of the co-occurrence algorithm. The technique proposed in this paper shows how to reduce the full multiscale feature set to a subset, the most suitable for classification using a fuzzy ARTMAP neural network. This is done by analysing the relevance of each feature for this particular classifier by means of the Histogram Distance Index (HDI). We validate the procedure by providing results of the classification of several satellite SAR data of the same urban test site. The results are encouraging. They show the potential of this technique for automatic extraction of the best texture and scale subset, suitable for efficient urban mapping using SAR satellite data. This work is an enlarged version of the paper 'Discriminating urban environments using multiscale texture and multiple SAR images', presented at WARSD'03.

Use of remotely sensed and ancillary data for estimating forest gross primary productivity in Italy

Maselli F., Barbati A.[2], Chiesi M.[1], Chirici G.[3], Corona P.[2]
[1]IBIMET-CNR, Via Madonna del Piano 10, 50019 Sesto Fiorentino (FI), Italy
[2]DISAFRI, University of Tuscia, Italy
[3]DISTAF, University of Florence, Italy

The current paper describes the development and testing of a procedure which can use widely available remotely sensed and ancillary data to assess large-scale patterns of forest productivity in Italy. To reach this objective a straightforward model (C-Fix) was applied which is based on the relationship between photosynthetically active radiation absorbed by plant canopies and relevant gross primary productivity (GPP). The original C-Fix meth-

odology was improved by using more abundant ancillary information and more efficient techniques for NDVI data processing. In particular, two extraction methods were applied to NDVI data, derived from two sensors (NOAA-AVHRR and SPOT-VGT) to feed C-Fix. The accuracy of the model outputs was assessed through comparison with annual and monthly values of forest GPP derived from eight eddy covariance flux towers. The results obtained indicated the superiority of SPOT-VGT over NOAA-AVHRR data and a higher efficiency of the more advanced NDVI extraction method. Globally, the procedure was proved to be of easy and objective implementation and allowed the evaluation of mean productivity levels of existing forests on the national scale.

Lava flow thermal analysis using three infrared bands of remote-sensing imagery: A study case from Mount Etna 2001 eruption

Lombardo V., Buongiorno M.F.

Istituto Nazionale di Geofisica e Vulcanologia, Via di Vigna Murata, 605, 00143, Roma, Italy

Infrared remotely sensed data can be used to estimate heat flux and thermal features of active volcanoes. The model proposed by Crisp and Baloga [Crisp, J., Baloga, S., 1990. A model for lava flows with two thermal components, Journal of Geophysical Research, 95, 1255–1270.] for active lava flows considers the thermal flux a function of the fractional area of two thermally distinct radiant surfaces. The larger surface area corresponds to the cooler crust of the flow, the smaller one to fractures in the crust. In this model, the crust temperature Tc, the temperature of the cracks Th, and the fractional area of the hottest component fh represent the three unknowns to work out. The simultaneous solution of the Planck equation ("dual-band" technique) for two distinct shortwave infrared (SWIR) bands allows to estimate any two of the parameters Tc, Th, fh, if the third is assumed [Dozier, J., 1981. A method for satellite identification of surface temperature fields of subpixel resolution. Remote Sensing Environment, 11, 221–229.]. The airborne sensor MIVIS was flown on Mount Etna during the July–August 2001 eruption. This hyperspectral imaging spectrometer offers 72 bands in the SWIR range and 10 bands in thermal infrared (TIR) region of the spectrum, which can be used to solve the dual-band system without any assumptions. Therefore, we can combine three spectral MIVIS bands to obtain simultaneous solutions for the three unknowns. Here, the procedure for solving such a system is presented. It is then demonstrated that a TIR channel is required to better pinpoint solutions to the 2-components model. Finally, the spatial and statistical characteristic of the resultant MIVIS-derived temperature and flux distributions are introduced and statistics for each hot spot investigated.

Near-surface thermal structure and surface diurnal warming in the Adriatic Sea using satellite and drifter data

Notarstefano G., Mauri E., Poulain P.M.[1]

Istituto Nazionale di Oceanografia e di Geofisica Sperimentale (OGS), Sgonico (Trieste)

An extensive set of in situ temperature data collected by surface drifters is combined with satellite-derived sea surface temperature images to study the difference between the pseudo-bulk and bulk temperatures (ΔT_{pb-b}) in the Adriatic Sea for the period 21 September 2002–31 December 2003. The variations of this temperature difference are described as a

function of local wind speed and incoming solar radiation provided by a local area atmospheric model. The daily sea surface temperature variability is also assessed by computing the temperature difference between the daily maximal and minimal values ($\Delta T_{\text{day–night}}$). The data show that the smaller the wind speed and the larger the solar radiation, the larger $\Delta T_{\text{pb–b}}$. The temperature difference reached the highest value (~5 °C) on a hot day (more than 600 W/m^2) of May 2003 in weak wind condition (around 3 m/s). For strong winds (speed > 6 m/s) the dependence on both the wind and solar radiations vanishes as the temperature difference approaches zero because the near-surface water becomes thermally homogenous due to the wind-induced vertical mixing. Strong diurnal warming of the sea surface, as derived by the pseudo-bulk estimates, and a strong near-surface stratification were found during the spring/summer season. Monthly mean statistics show that the diurnal cycle of the pseudo-bulk and bulk temperature starts to become significant already in February and March. Subsequently (from April to August) both the diurnal warming and the stratification are maximal (monthly means of $\Delta T_{\text{day–night}}$ ~1-2 °C and of $\Delta T_{\text{pb–b}}$ ~0.5 °C), while in fall and early winter the $\Delta T_{\text{pb–b}}$ values are quite small (monthly means near 0 °C) and the $\Delta T_{\text{day–night}}$ monthly means are bounded by 0.5-1.5 °C. Maximal amplitudes of the diurnal cycle can exceed 4 °C (mostly in spring-summer) for both the pseudo-bulk and bulk temperatures. However, the monthly means of $\Delta T_{\text{day–night}}$ is generally twice as large for the pseudo-bulk estimates (~2 °C) with respect to the bulk layer (~1 °C). The diurnal warming of the sea surface, as derived by the pseudo-bulk temperature, occurs at about 14:30 local time, that is more than 2 h after the maximal sun elevation and an hour earlier than the bulk temperature maximum at 20-40 cm depth.

A quantitative assessment of the SBAS algorithm performance for surface deformation retrieval from DInSAR data

Casu F.[1, 2], Manzo M.[1, 3], Lanari R.[1]

[1]Ist. per il Rilevamento Elettromagnetico dell'Ambiente, CNR, Via Diocleziano 328, 80124 Napoli, Italy

[2]Dip. di Ingegneria Elettrica ed Elettronica, Univ. degli Studi di Cagliari, P.zza d'Armi, 09123 Cagliari, Italy

[3]Dip. di Ingegneria e Fisica dell'Ambiente, Univ. degli Studi della Basilicata, Via Sauro 85, 85100 Potenza, Italy

We investigate in this work the performance of the Small BAseline Subset (SBAS) approach that is a Differential Synthetic Aperture Radar Interferometry (DInSAR) algorithm allowing the generation of mean deformation velocity maps and displacement time series from a data set of subsequently acquired SAR images. In particular, we have carried out a quantitative assessment of the SBAS procedure performance by processing SAR data acquired by the European Remote Sensing Satellite (ERS) sensors and comparing the achieved results with geodetic measurements that are assumed as reference. The analysis has been focused on the Napoli bay (Italy) and Los Angeles (California) test areas where different deformation phenomena are present and, at the same time, a large amount of ERS SAR data is available as well as geometric leveling (in the Napoli zone) and continuous GPS (in the Los Angeles zone) measurements, to be used for our performance analysis. Moreover, due to the presence of large urbanized zones, the selected test sites are also characterized by extended, highly coherent areas in the DInSAR maps. The presented study shows that the SBAS technique provides an estimate of the mean deformation velocity with a standard deviation of about 1 mm/year for a typical ERS data set including between 40 and 60 images. Moreover, the single displacement measurements, computed with respect to a reference point of known motion, show a sub-centimetric accuracy with a standard devia-

tion of about 5 mm, consistently in both the SAR/leveling and SAR/GPS comparisons; we also show that there is an increase of this standard deviation value as we move away from the reference SAR pixel, with an estimated spatial variation value of about 0.05 mm/km.

Leaf level detection of solar induced chlorophyll fluorescence by means of a subnanometer resolution spectroradiometer

Meroni M.[1,2], Colombo R.[2]

[1]Forest Ecology Lab., Dip. Scienze dell'Ambiente Forestale e delle sue Risorse, Università della Tuscia, 01100 Viterbo, Italy

[2]Remote Sensing of Environmental Dynamics Lab., Dip. Scienze dell'Ambiente e del Territorio, Università Milano-Bicocca, 20126 Milano, Italy

A leaf level investigation on the spectral signature of Phaseolus vulgaris was undertaken by using a very high spectral resolution spectroradiometer featuring full width at half maximum of 0.06 nm and spectral range of 635.5–802.5 nm. High spectral resolution allows detection of leaf reflected and emitted radiance fields in two narrow absorption bands at 687 and 760 nm, respectively, where solar irradiance is strongly reduced owing to molecular oxygen absorption of the terrestrial atmosphere. The flux emitted due to chlorophyll fluorescence was measured using the Fraunhofer line depth principle by spectrally modelling the signal, capitalizing on the high resolution of the spectroradiometer devices. An experiment was conducted on two potted bean plants. One was maintained in good health for use as a reference while the other was treated with a photosystem II inhibitor. Collected spectra show that the fluorescence emission produces a pair of characteristic peaks superimposed on the typical leaf-specific reflectance curve. The magnitude of the fluorescence signal of the herbicide-treated leaf was four times greater than that of the control plant, thus indicating damage to the photosynthetic apparatus of the plant.

Mapping salt-marsh vegetation by multispectral and hyperspectral remote sensing

Belluco E.[1], Camuffo M.[2], Ferrari S.[1], Modenese L.[2], Silvestri S.[3], Marani A.[2], Marani M.[1]

[1]Dipartimento IMAGE and International Centre for Hydrology "Dino Tonini", University of Padova, via Loredan 20, I-35131 Padova, Italy

[2]Environmental Science Department, University of Venice, Dorsoduro 2137, I-30123 Venice, Italy

[3]Servizio Informativo-CVN-Magistrato alle Acque di Venezia, San Marco 2803, I-30124 Venice, Italy

Tidal marshes are characterized by complex patterns both in their geomorphic and ecological features. Such patterns arise through the elaboration of a network structure driven by the tidal forcing and through the interaction between hydrodynamical, geophysical and ecological components (chiefly vegetation). Intertidal morphological and ecological structures possess characteristic extent (order of kilometers) and small-scale features (down to tens of centimeters) which are not simultaneously accessible through field observations, thus making remote sensing a necessary observation tool. This paper describes a set of remote sensing observations from several satellite and airborne platforms, the collection of concurrent ground reference data and the vegetation distributions that may be inferred from them, with specific application to the Lagoon of Venice (Italy). The data set comprises ROSIS, CASI,

MIVIS, IKONOS and QuickBird acquisitions, which cover a wide range of spatial and spectral resolutions. We show that spatially-detailed and quantitatively reliable vegetation maps may be derived from remote sensing in tidal environments through unsupervised (K-means) and supervised algorithms (Maximum Likelihood and Spectral Angle Mapper). We find that, for the objective of intertidal vegetation classification, hyperspectral data contain largely redundant information. This in particular implies that a reduction of the spectral features is required for the application of the Maximum Likelihood classifier. A large number of experiments with different feature extraction/selection algorithms show that the use of four bands derived from Maximum Noise Fraction transforms and four RGBI broad bands obtained by spectral averaging yield very similar classification performances. The classifications from hyperspectral data are somewhat superior to those from multispectral data, but the close performance and the results of the features reduction experiments show that spatial resolution affects classification accuracy much more importantly than spectral resolution. Monitoring schemes of tidal environment vegetation may thus be based on high-resolution satellite acquisitions accompanied by systematic ancillary field observations at a relatively limited number of reference sites, with practical consequences of some relevance.

Titan, fractals, and filtering of Cassini altimeter data

Franceschetti G., Callahan P.S., Iodice A., Riccio D., Wall S.D.
Dept. of Electron. & Telecommun. Eng., Univ. of Naples "Federico II", Italy

Fractal behavior of one Titan profile acquired by the Cassini altimeter during its first flyby is demonstrated and quantitatively analyzed. The inadequacy of popular nonfractal models to represent scale-dependent behavior is also discussed. Our results lead to the conjecture that a proper geometrical model of the Titan surface is provided by the fractional Brownian motion stochastic process and that the particular acquired profile has a fractal dimension of about 2.4. In addition, use of the developed statistical model allows the design of model-based filters for a significant improvement of the measurement accuracy, at the expense of the horizontal resolution.

Influence of geometrical factors on crop backscattering at C-band

Della Vecchia A., Ferrazzoli P., Guerriero L., Blaes X., Defourny P., Dente L., Mattia F., Satalino G., Strozzi T., Wegmuller U.
Dipt. di Informatica, Univ. di Roma "Tor Vergata", Rome, Italy

Several efforts, aimed at developing and refining crop backscattering models, have been done during the last years. Although important advances have been achieved, it is recognized that further work is required, both in the electromagnetic characterization of single scatterers and in the combination of contributions. This work is focused on the description of leaf geometry and of the internal structure of stems. Recently developed routines, able to model the scattering cross sections of curved sheets and hollow cylinders, are adopted for this purpose and run within the multiple-scattering model developed at the University of Rome "Tor Vergata". Input parameters are taken from experimental campaigns. In

particular, ground data collected over a maize field at the Central Plain site in 1988, over wheat and maize fields at the Loamy site in 2003, and over wheat fields at the Matera site in 2001 and 2003 are considered. The multitemporal backscattering coefficients at C-band are simulated. The results obtained under different assumptions are compared to each other, and with C-band radar signatures collected over the same fields. The influence of some critical factors, affecting crop backscattering, is discussed. It is demonstrated that a more detailed scatterer characterization may improve the model accuracy, especially in the case of hollow stems.

A sampling method for the retrospective validation of global burned area products

Boschetti L., Brivio P.A., Eva H.D., Gallego J., Baraldi A., Gregoire J.M.

Joint Research Centre, European Commission. 21020 Ispra. (Varese), Italy

This work presents a design-based validation and calibration scheme for the Global Burned Area 2000 (GBA2000) products. The objective of such a scheme is to assess the margins of uncertainty associated with the burned area products and to estimate calibration coefficients needed to convert burned pixel counts into areal estimates. As the validation of GBA2000 was performed long after 2000, and given the fact that burned areas are a predominantly nonpermanent land cover change, the reference data are obtained from a set of Landsat-7 Enhanced Thematic Mapper Plus high-resolution remotely sensed data. A stratified sampling scheme is presented, specifically designed for the retrospective validation of burned area data; the scheme is based on combining information from two low-resolution burned area products (GBA2000 itself and Globscar). The resulting stratification has been applied to the whole global GBA2000 dataset, and preliminary validation results are reported for Africa. The conclusions highlight the limits of a retrospective validation exercise, and summarize some of the open issues in the validation of global burned area maps.

Impact of tropospheric scintillation in the Ku/K bands on the communications between two LEO satellites in a radio occultation geometry

Martini E., Freni A., Facheris L., Cuccoli F.

Dept. of Inf. Eng., Univ. of Siena, Italy

A theoretical analysis of the impact of clear-air tropospheric scintillation on a radio occultation link between two low Earth orbit satellites in K- and Ku-bands is presented, with particular reference to differential approaches for the measure of the total content of water vapor. The troposphere is described as a spherically symmetric turbulent medium satisfying Kolmogorov theory. Rytov's first iteration solution for weak fluctuations is used to derive an expression for the variance of amplitude fluctuations of the wave as well as their spectrum and the correlation between fluctuations at different frequencies. The validity of the assumptions made and the influence of atmospheric parameters on the quantities of interest are also investigated and discussed. Finally, numerical results are presented to provide an estimate of the level of scintillation-induced disturbances.

Norme per gli Autori

Nella Rivista sono presenti tre tipi di **articoli principali, essi possono essere sia in lingua italiana che in lingua inglese**:

Ricerche: articoli che riportano i risultati di ricerche originali;

Applicazioni: articoli che riportano casi di studio in cui vengono applicate metodologie ormai consolidate;

Review: revisioni critiche di argomenti più generali e presentazioni a carattere didattico di argomenti specifici.

Gli articoli principali sono soggetti a revisione da parte di due esperti indicati dal Direttore Scientifico.

Sulla Rivista vengono inoltre pubblicati i resoconti di congressi, di seminari o di attività dei gruppi di ricerca, così come brevi descrizioni di nuove attrezzature e di software di interesse per gli operatori del settore. Vengono pubblicati i riassunti di tesi di laurea e di dottorato, gli abstract di lavori di Autori italiani pubblicati su riviste straniere e le recensioni dei libri.

Gli Autori degli articoli principali sono pregati di rispettare le seguenti norme. Per la stesura degli altri contributi si consiglia di fare riferimento agli ultimi numeri della Rivista. Gli articoli non redatti in piena conformità con le presenti Norme non potranno essere presi in considerazione per la pubblicazione.

Titolo: sia in inglese che in italiano, max 120 caratteri inclusa la spaziature fra le parole.

Abstract: sia in inglese che in italiano, per ognuno max 750 caratteri inclusa la spaziatura fra le parole.

Parole chiave: sia in inglese che in italiano, indicanti l'oggetto del contributo, il tipo di dati utilizzati, le metodologie utilizzate, ecc.

Autore/i: Nome e Cognome seguito da un numero in apice per indicare l'eventuale Istituto di appartenenza ed il relativo indirizzo.

Lunghezza articolo: indicativamente 6-12 pagine di rivista per le Ricerche e le Review; 4-6 pagine per le Applicazioni. Lunghezze diverse possono essere concordate con la Redazione. Per consentire la stampa diretta degli estratti, gli articoli devono svilupparsi su di un numero pari di pagine. Particolari esigenze di impaginazione possono determinare la stampa delle figure con dimensioni diverse da quelle auspicate dagli Autori. Gli Autori debbono chiaramente indicare specifiche indicazioni in merito al momento dell'invio in Redazione della versione definitiva del contributo.

Stile: evitare il più possibile i rientri e, comunque, farne di un solo ordine. Gli elenchi puntati sono identificati da "-", "l)" oppure "a)"; ogni elemento dell'elenco è chiuso con";" salvo l'ultimo che chiude con un punto. Non inserire altri caratteri, di formato diverso o sottolineati.

Il neretto è utilizzato solo per il titolo dei paragrafi. Eventuali sottoparagrafi possono portare un titolo in corsivo neretto. Non inserire righe bianche nel testo se non alla fine di paragrafi e dei sottoparagrafi. Tutti i testi, compreso il titolo generale e quello dei paragrafi, devono essere scritti in Maiuscolo e minuscolo.

Formato per l'invio del manoscritto in revisione: nel momento in cui il contributo viene inviato affinché sia sottoposto alle revisione dei referee dovrà essere formattato come segue: spaziatura doppia, linee numerate, Tabelle e Figure riportate in fondo al contributo. Sono accettati formati sia in MICROSOFT WORD (.doc, .docx, .rtf) sia in ADOBE ACROBAT (.pdf). Il file deve essere inviato solo per posta elettronica agli indirizzi: **marchettimarco@unimol.it** e **gherardo.chirici@unimol.it** con esplicita indicazione dell'Autore di riferimento per i contatti con la Redazione (afferenza, indirizzo con numeri telefonici fissi e mobili e posta elettronica).

Formato per l'invio del manoscritto in pubblicazione: nel momento in cui il manoscritto ha completato il processo di revisione all'Autore di riferimento viene richiesto l'invio in forma elettronica

(.doc, .docx o .rtf) del manoscritto formattato per la pubblicazione come segue:

Font: Times New Roman, interlinea singola. Titolo: 15 pt centrato, grassetto. Autori: (nome e cognome per esteso) 9,5 pt, grassetto. Affiliazioni: 9 pt, normale, centrato. Titoli dei paragrafi: 11,5 pt, grassetto, no maiuscolo, nè maiuscoletto, giustificati a sinistra e non puntati. Testo: 10,5 pt, normale, giustificato.

Le equazioni e le formule devono essere identificate da un numero racchiuso tra parentesi quadra e posizionato a destra. Anche nei riferimenti di equazioni e formule all'interno del testo devono essere usate le parentesi quadre.

Tabelle: i caratteri alfabetici/numerici per le tabelle sono in stile Times New Roman corpo 9. Le Tabelle (o *tables* se il contributo è in lingua Inglese) sono citate nel testo con Tabella n (Table n), oppure (Tab. n) se fra parentesi. Devono essere precedute da una didascalia in grassetto corpo 9. con "Tabella" ("Table") per esteso, seguito dal trattino e non puntato. es. Tabella 1 - (Table 1 -).

Le Tabelle debbono essere inserite nel testo centrate. Le Tabelle devono essere in bianco e nero.

Figure (fotografie, schemi, diagrammi, grafici): le Figure (o *figures* se il contributo è in lingua Inglese) sono identificate con Figura n (Figure n), oppure (Fig. n) se fra parentesi. Devono essere seguite da una didascalia in grassetto corpo 9 con "Figura" ("Figure") per esteso, seguito dal trattino e non puntato. es. Figura 1 - (Figure 1 -). La larghezza massima delle figure è 17 cm e non è prevista la stampa di figure ruotate. Ad eccezione delle figure stampate a giustezza piena, tutte le altre non potranno avere una base superiore a 9,5 cm. La Redazione è a disposizione per discutere aspetti tecnici relativi a questo punto. Le figure devono essere inserite nel corpo del testo (anche a bassa risoluzione) delle dimensioni desiderate per la stampa. Le figure devono inoltre essere fornite in un file separato dal testo, in formato .tiff o .eps e ad una risoluzione minima di 300 dpi. Gli Autori sono pregati di ridurre al minimo il numero delle figure a colori. La Redazione potrà chiedere la conversione in B/N di figure nelle quali l'uso del colore non sia essenziale alla comprensione.

Note a piè di pagina: sono da evitare il più possibile e verranno comunque riportate in corpo minore in fondo all'ultima pagina dell'articolo con richiami numerici nel testo. Indicazioni di Progetti e Finanziamenti verranno inserite prima della Bibliografia con gli eventuali Ringraziamenti.

Riferimenti bibliografici: nell'articolo le citazioni sono racchiuse fra [ ] con il seguente formato: [Verdi, 1990] o [Rossi e Verdi, 1989]; [Verdi et al., 1987] qualora il numero degli Autori sia maggiore di due. Più lavori dello stesso autore e dello stesso anno saranno identificati con le lettere a, b, c. ecc. Più lavori dello stesso autore citati consecutivamente dovranno essere posti in ordine cronologico, con gli anni separati da virgola [Rossi, 1990, 1993] , mentre più lavori di autori diversi saranno separati dal punto e virgola [Rossi, 1990; Bianchi 1997]. Se citato nell'ambito di una frase il nome di un Autore [1995] è seguito dall'anno della pubblicazione a cui si fa riferimento.

Bibliografia: tutti e solo i lavori citati nel testo devono comparire in Bibliografia. La Bibliografia deve essere in ordine alfabetico per cognome; a esempio:

Bianchi A., Rossi V., Verdi T. (1999) - *Metodi di integrazione fra dati TM e dati SPOT.* Riv. Ital. Telerilevamento, 19: 153-157. (19 è il numero del fascicolo, 153-157 1e pagine).

Neri A., Rossi C. (1978) - *Elementi di Telerilevamento.* Nessuno Ed., Roma. pp.324.

Violi K. (1998) - *Elaborazione di dati ERS-3 per l'identificazione di alvei sepolti.* Atti XXI Congr. Soc. Ital. Geomorfologia. Pisa. pp. 34-76.

Evitare di usare **AA.VV.**, anche se il numero degli Autori è elevato.

Estratti: È previsto l'invio dei PDF definiti di stampa.

Contributo alla stampa: Grafici e tabelle a colori e le figure a colori in numero superiore a 2 richiedono un contributo alla pubblicazione pari a 200€ a figura/tabella/grafico. Gli Autori sono pregati di inviare, insieme alle bozze corrette, le indicazioni necessarie per l'intestazione della nota di debito. I pagamenti devono essere effettuati tramite versamento su ICCP n.29688504 AIT - Firenze, indicandone la causale.

Rivista italiana di TELERILEVAMENTO

n° 38 - 2007

Indice